ORGANISATION EUROPÉENNE POUR LA RECHERCHE NUCLÉAIRE

CERN EUROPEAN ORGANIZATION FOR NUCLEAR RESEARCH

PRINCIPLES OF OPERATION OF MULTIWIRE

PROPORTIONAL AND DRIFT CHAMBERS

F. Sauli

Lectures given in the

Academic Training Programme of CERN

1975-1976

G E N E V A

1977

ABSTRACT

The report gives a detailed review of energy-loss processes and of charge drift and diffusion in gases, which define the operational characteristics of this family of charged-particle and photon detectors. In a practical discussion of the chambers themselves, emphasis is placed on gas properties and electrostatics whereas the mechanics and electronics of the chambers are covered by references to the extensive bibliography.

CONTENTS

1. INTRODUCTION

The first multiwire proportional chamber, in its modern conception, was constructed and operated by Charpak and his collaborators in the years 1967-68 [1]. It was soon recognized that the main properties of a multiwire proportional chamber, i.e. very good time resolution, good position accuracy and self-triggered operation, are very attractive for the use of the new device in high-energy physics experiments. Today, most fast detectors contain a large number of proportional chambers, and their use has spread to many different fields of applied research, such as X-ray and heavy ion astronomy, nuclear medicine, and protein crystallography [2]. In many respects, however, multiwire proportional chambers are still experimental devices, requiring continuous attention for good operation and sometimes reacting in unexpected ways to a change in the environmental conditions. Furthermore, in the fabrication and operation of a chamber people seem to use a mixture of competence, technical skill and magic rites, of the kind "I do not know why I'm doing this but somebody told me to do so".

In these notes I will try to illustrate the basic phenomena underlying the behaviour of a gas detector, with the hope that the reader will not only better understand the reasons for some irrational-seeming preferences (such as, for example, in the choice of the gas mixture), but will also be able better to design detectors for his specific experimental needs.

Most of the recent development on multiwire proportional chambers is due to the enthusiastic work of Georges Charpak who initiated me into this exciting field of applied research; these notes are dedicated to him.

A large number of the illustrations have been extracted from old textbooks and articles, and I would like to thank Claude Rigoni for her great skill and patience in making them suitable for reproduction.

2. DETECTION OF CHARGED PARTICLES

2.1 Generalities

A fast charged particle, traversing a gaseous or condensed medium, can interact with it in many ways. Of all possible interactions, however, only the electromagnetic one is generally used as a basis for detection, being many orders of magnitude more probable than strong or weak interactions and therefore leaving a "message" even in very thin samples of material. These notes are mainly concerned with the highly probable incoherent Coulomb interactions between the electromagnetic fields of the incoming charged particle and of the medium, resulting in both excitation and ionization of the atoms of the medium itself. The contribution of other electromagnetic processes (at least for particles heavier than electrons), such as bremsstrahlung, Čerenkov, and transition radiation, to the total energy loss is negligible in gas detectors and we will ignore them.

2.2 Energy loss due to electromagnetic interactions

An expression for the average differential energy loss (loss per unit length) due to Coulomb interactions has been obtained by Bethe and Bloch [3] in the framework of relativistic quantum mechanics, and can be written as follows (in the electrostatic unit system):

$$\frac{dE}{dX} = - K \frac{Z}{A} \frac{\rho}{\beta^2} \left\{ \ln \frac{2mc^2\beta^2 E_M}{I^2(1-\beta^2)} - 2\beta^2 \right\} , \qquad K = \frac{2\pi N z^2 e^4}{mc^2} \qquad (1)$$

where N is the Avogadro number, m and e are the electron mass and charge, Z, A and ρ are the atomic number and mass, and the density of the medium, respectively, and I is its effective ionization potential; z is the charge and β the velocity (in units of the speed of light c) of the projectile. In the electrostatic unit system and expressing energies in MeV, K = 0.154 MeV g^{-1} cm^2 for unit charge projectiles. In the system used, the rest energy of the electron, mc^2, equals 0.511 MeV.

The quantity E_M represents the maximum energy transfer allowed in each interaction, and simple two-body relativistic kinematics gives

$$E_M = \frac{2mc^2\beta^2}{1 - \beta^2} . \qquad (2)$$

For example, for 1 GeV/c protons (β = 0.73) E_M = 1.2 MeV. Not always, however, can this kinematical limit be used, particularly in the case of thin detectors where energy can escape in the form of δ-rays (see Section 2.4).

It is customary to substitute for the length X a reduced length x defined as $X\rho$ and measured in g cm^{-2}. In this case, the reduced energy loss can be written as

$$\frac{dE}{dx} = \frac{1}{\rho} \frac{dE}{dX} .$$

The value of the effective ionization potential I is in general the result of a measurement for each material; a rather good approximation is, however, $I = I_0 Z$ with $I_0 \simeq 12$ eV. Values of I_0 are given in Table 1 for several gases. For molecules and for gas mixtures, average values for Z, A, and I have to be taken.

Table 1

Properties of several gases used in proportional counters (from different sources, see the bibliography for this section). Energy loss and ion pairs per unit length are given at atmospheric pressure for minimum ionizing particles

Gas	Z	A	δ (g/cm³)	E_{ex}	E_i	I_0	W_i	dE/dx (MeV/g cm⁻²)	(keV/cm)	n_p (i.p./cm) [a]	n_T (i.p./cm) [a]
					(eV)						
H_2	2	2	8.38×10^{-5}	10.8	15.9	15.4	37	4.03	0.34	5.2	9.2
He	2	4	1.66×10^{-4}	19.8	24.5	24.6	41	1.94	0.32	5.9	7.8
N_2	14	28	1.17×10^{-3}	8.1	16.7	15.5	35	1.68	1.96	(10)	56
O_2	16	32	1.33×10^{-3}	7.9	12.8	12.2	31	1.69	2.26	22	73
Ne	10	20.2	8.39×10^{-4}	16.6	21.5	21.6	36	1.68	1.41	12	39
Ar	18	39.9	1.66×10^{-3}	11.6	15.7	15.8	26	1.47	2.44	29.4	94
Kr	36	83.8	3.49×10^{-3}	10.0	13.9	14.0	24	1.32	4.60	(22)	192
Xe	54	131.3	5.49×10^{-3}	8.4	12.1	12.1	22	1.23	6.76	44	307
CO_2	22	44	1.86×10^{-3}	5.2	13.7	13.7	33	1.62	3.01	(34)	91
CH_4	10	16	6.70×10^{-4}		15.2	13.1	28	2.21	1.48	16	53
C_4H_{10}	34	58	2.42×10^{-3}		10.6	10.8	23	1.86	4.50	(46)	195

a) i.p. = ion pairs

Inspection of expression (1) shows that the differential energy loss depends only on the projectile velocity β, not on its mass. After a fast decrease dominated by the β^{-2} term, the energy loss reaches a constant value around $\beta \simeq 0.97$ and eventually slowly increases for $\beta \to 1$ (relativistic rise). The region of constant loss is called the minimum ionizing region and corresponds to the more frequent case in high-energy physics.

When plotting dE/dX as a function of the projectile energy, see Fig. 1 (computed for air), one observes that at energies above a few hundred MeV all particles are at the minimum of ionization and therefore lose the same amount of energy per unit length; for most materials, dE/dx is equal to about 2 MeV g^{-1} cm^2 at the minimum. Computed values of the differential energy loss at the minimum are given in Table 1, together with other relevant parameters and for the gases commonly used in proportional counters.

It should be emphasized that, even for thin materials, the electromagnetic energy loss is the result of a small number of discrete interactions and, therefore, has the characteristics of a statistical average. The distribution, however, is not Gaussian for all cases where the energy loss ΔE is small compared to the total energy, as will be discussed below. Furthermore, a closer look at the interaction mechanism shows that individual events can be grouped in two classes: close collisions, with large energy transfers resulting in the liberation of electronic charges (ionizations), and distant collisions involving smaller energy transfers and resulting in both ionization and atomic excitation. Primary ionization and excitation share more or less equally the available energy loss, although secondary effects can increase the efficiency for one of the processes. In Fig. 2 [4] the probability of the processes described is qualitatively shown as a function of the energy transfer, in a single event, for 100 keV incident electrons.
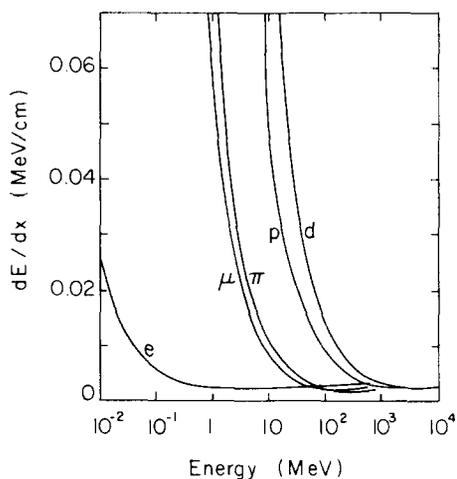

Fig. 1 Energy loss per unit length in air, as computed from expression (1), for different particles as a function of their energy. At energies above 1 GeV/c or so, all particles lose about the same amount of energy (minimum ionization plateau).

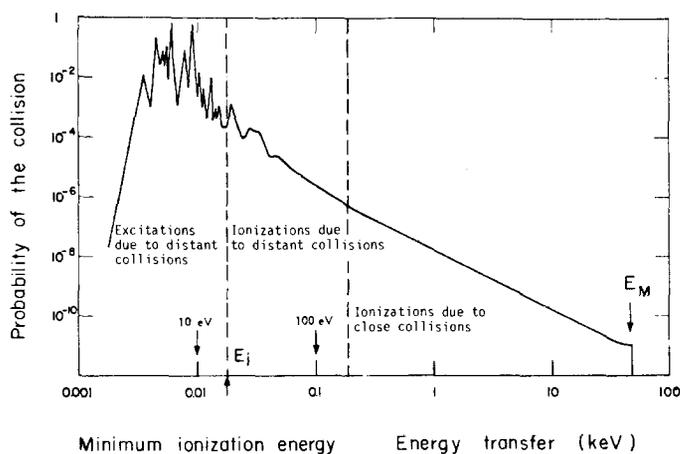Fig. 2 Relative probability of different processes induced by fast (100 keV) electrons in water, as a function of the energy transfer in a collision[4]. The maximum kinematically allowed energy transfer, E_M = 50 keV in this case, is also shown.

2.3 The relativistic rise of energy loss

At very high momenta, above 10 GeV/c or so, the logarithmic term in the Bethe-Block formula produces an increase of the energy loss; this may constitute a basis for particle identification at very high energies since, for a given momentum, the average energy loss will be slightly different for different masses. Polarization effects, not taken into account by expression (1), however, produce a saturation in the increase, that would other-wise indefinitely continue. In gases, saturation occurs around a few hundred GeV/c at a value which is about 50% above minimum ionizing; Fig. 3 shows a collection of experimental data for argon[5]. For statistical reasons, discussed more fully later, an effective par-ticle identification in the region of the relativistic rise requires a very large number of independent measurements of energy loss for each track, and stacks of multiwire proportional chambers have been succesfully used for this purpose[6].
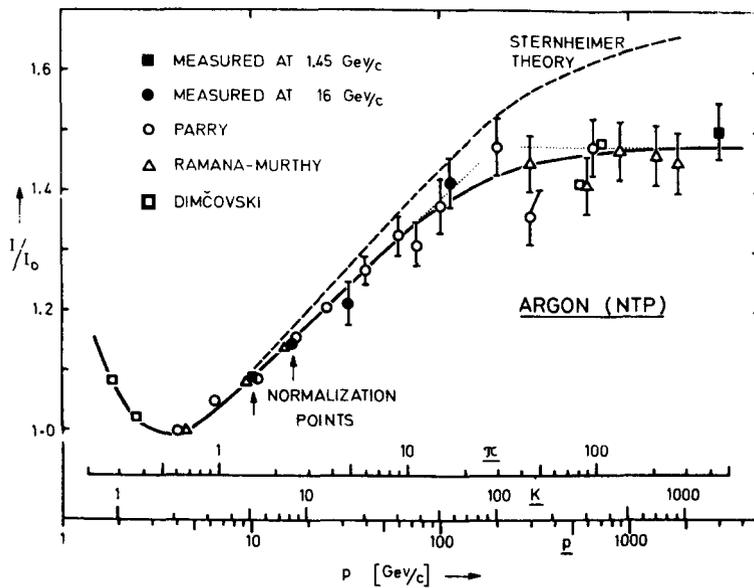

Fig. 3   Relativistic rise of the energy loss in argon, as a function of particle mass and momentum; the vertical scale gives the relative increase above the minimum of ionization[5]

2.4 δ-ray production

In ionizing encounters, the ejected electron is liberated with an energy E that can assume any value, up to the maximum allowed E_M, as given by expression (2). An approximate expression for the probability of an electron receiving the energy E is given by[3]

$$P(E) = K \frac{Z}{A} \frac{\rho}{\beta^2} \frac{X}{E^2} \tag{3}$$

that corresponds essentially to the first term in the Bethe-Bloch formula. More accurate expressions can be found elsewhere[7,8], but for our needs the approximation (3) is suffi-cient. If the reduced thickness $x = X\delta$ is introduced, and given in g cm^{-2}, the expression can be conveniently rewritten as

$$P(E)dE = \frac{K}{\beta^2} \frac{Z}{A} \frac{x}{E^2} dE = W \frac{dE}{E^2} \quad . \tag{3'}$$

Electrons ejected with an energy above a few keV are normally called δ-rays, using an old emulsion terminology. Integration of expression (3') allows one to obtain an expression for the number of δ electrons having an energy E_0 or larger:

$$N(E \geq E_0) = \int_{E_0}^{E_M} P(E) \, dE = W\left(\frac{1}{E_0} - \frac{1}{E_M}\right) \simeq \frac{W}{E_0} \quad,$$

the last approximation being valid for $E_0 \ll E_M$.

As an example, Fig. 4 shows the number of electrons ejected with energy $E \geq E_0$ by 1 GeV/c protons, as a function of E_0 in 1 cm of argon at normal conditions. There are, for example, about ten electrons emitted with energy above 15 eV, which is the ionization potential of argon (see Table 1); these considerations are very important for the understanding of secondary processes (see below). In Fig. 4, the maximum energy transfer for 1 GeV/c protons as projectiles is also shown, as given by expression (2).

The angle of emission of a δ electron of energy E is given in a free-electron approximation, by the expression[8]

$$\cos^2 \theta = \frac{E}{E_M} \quad.$$
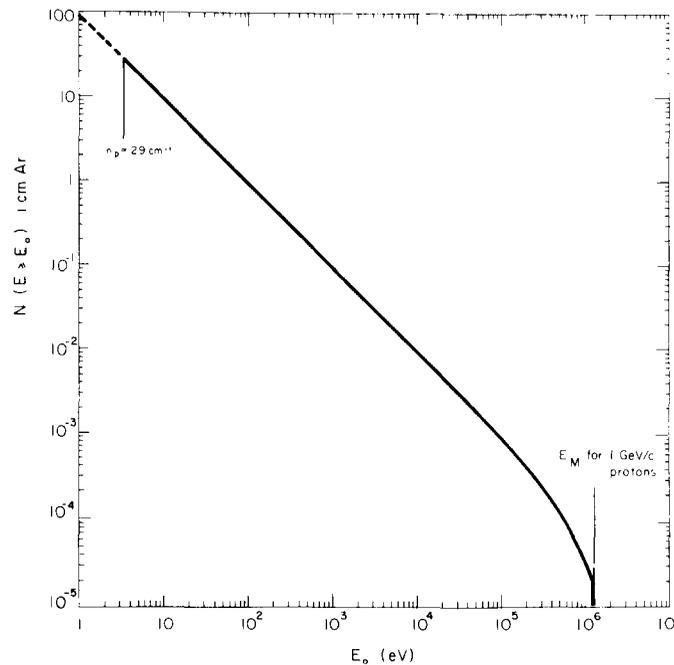

Fig. 4   Computed number of δ electrons ejected at an energy larger than or equal to E_0, as a function of E_0, in 1 cm of argon at normal conditions. The average number of primary ionizing collisions (29 per cm) and the maximum allowed energy transfer for 1 GeV/c protons are shown.

Therefore for minimum ionizing particles ($E_M > 1$ MeV), and up to energies of emission of several keV, δ rays are emitted perpendicularly to the incident track; however, multiple scattering in the medium quickly randomizes the direction of motion of δ electrons. In fact, typical electron molecule cross-sections, in the keV region, are around 10^{-16} cm^2 [3], at atmospheric pressure, this corresponds to a mean free path between collisions of a few microns. For energies around a hundred electronvolts, the cross-section is increased by an order of magnitude or so owing to the high probability of inelastic collisions (see Section 4.7). Because of the large mass difference between target and projectile, large momentum transfers (scattering angles) are highly probable, which means that in a few collisions any trace of the electron's original emission angle will be obliterated. A detailed discussion of the process can be found in Refs. 6 and 7.

2.5 Range of slow electrons

Depending on their energy, δ electrons will cover a certain distance in the gas, suffering elastic and inelastic scatters from the molecules. The total range R_T for an energy E, along the trajectory, can be calculated integrating the Bethe-Block formula over the length R_T and requiring the integral to equal the total available energy; however, it gives a bad representation of the distance effectively covered by an electron, because of the randomizing effect of the multiple collisions. It is customary to define a practical range R_p that appears to be two or three times smaller than the total range and in general is the result of an absorption measurement. For energies up to a few hundred keV, a rather good approximation for the practical range, in g cm^{-2}, is[8]

$$R_p = 0.71 \ E^{1.72} \qquad (E \text{ in MeV}) \ .$$

Figure 5 gives the range of electrons in argon, under normal conditions, as a function of energy. Combining the data of Figs. 4 and 5, one can deduce, for example, that in 1 cm of argon, one out of twenty minimum ionizing particles ejects a 3 keV electron having a practical range of 100 μm.

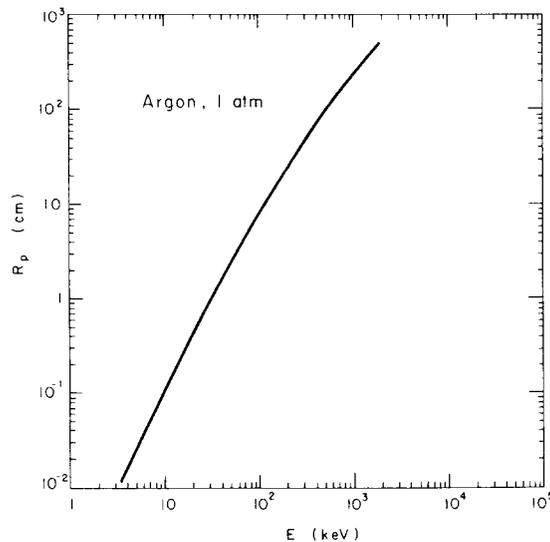Fig. 5 Range of electrons in argon, at normal
conditions as a function of energy, de-
duced from measurement in light materials[8]

Since the average energy loss in argon is 2.5 keV/cm, these events will result in a much bigger pulse height, and also the centre of gravity of the detected charge, which is the best position information one can get, will be systematically displaced to one side of the original track. This obviously sets a limit to the best accuracy of position one can hope to obtain in a single gas counter operating at atmospheric pressure, somewhere between 20 and 30 µm. Actual measurements obtained so far with high accuracy drift chambers provide accuracies of localization of between 50 and 100 µm [9,10]. Notice that an increase in the gas density or pressure does not obviously improve the accuracy since, although the range of electrons will decrease, the number produced at any given energy will increase.

Also, from Fig. 5 one can deduce that electrons produced with energies above 30 keV have a range larger than 1 cm of argon, and will escape detection from the 1 cm thick layer. In this case use of the Bethe-Block formula is not completely justified, since the maximum energy transfer E_M cannot in fact be dissipated in the detector.

2.6 Energy loss distribution

The fact that in thin materials the total energy loss is given by a small amount of interactions, each one with a very wide range of possible energy transfers, determines a characteristic shape for the energy loss distribution. In a classical formulation due to Landau, the energy-loss distribution in thin media is written as [11]

$$f(\lambda) = \frac{1}{\sqrt{2\pi}} e^{-\frac{1}{2}(\lambda + e^{-\lambda})} \quad ,$$

where the reduced energy variable λ represents the normalized deviation from the most probable energy loss $(\Delta E)_{mp}$:

$$\lambda = \frac{\Delta E - (\Delta E)_{mp}}{\xi} \quad , \qquad \text{where } \xi = K \frac{Z}{A} \frac{\rho}{\beta^2} X \quad ,$$

ΔE being the actual loss and ξ the average energy loss given by the first term in the Bethe-Block formula. Figure 6 shows the characteristic shape of the Landau distribution, and indicates the meaning of the average and of the most probable energy losses. Notice the long tail at very large energy losses, corresponding to events where one or more energetic δ electrons have been produced. The energy resolution of thin counters for fast particles is therefore very poor; increasing the thickness of the detector is of no help, since the number of energetic electrons will increase (unless, of course, one gets close to total absorption where Gaussian statistics again dominate).

The large fluctuation in energy loss for individual events has several important practical consequences. First, when designing the amplification electronics for a gaseous detector one has to take into account the large dynamic range of the signals. Secondly, a single measurement of a track contains very little information about the average energy loss; when trying to identify particles in the relativistic rise region from the small increase of dE/dx, one is obliged to sample each track as much as several hundred times. This requires the development of relatively cheap, large surface multiwire proportional chambers.
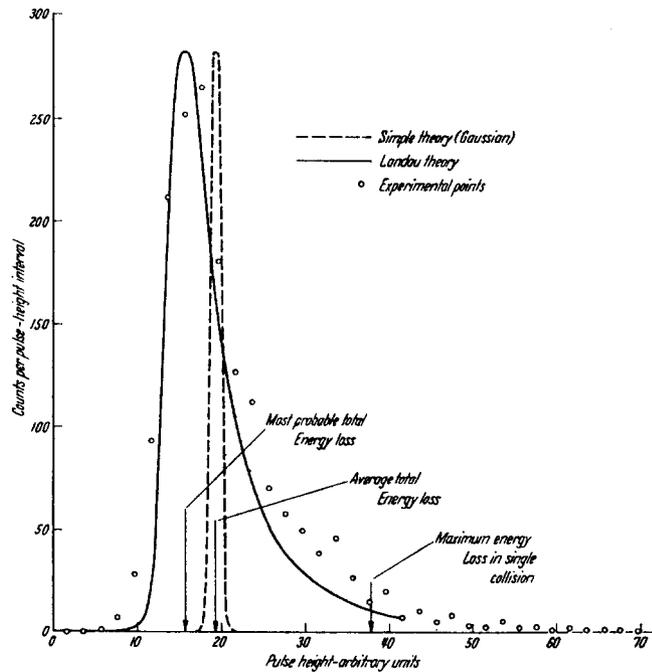
Fig. 6   (From Franzen and Cochran, see bibliography
          for Section 5.) Comparison of the experi-
          mental energy loss distribution, in an argon-
          carbon dioxide counter, with the distribu-
          tion computed using a simple Gaussian theory
          and the Landau expression.

2.7 Primary and total ionization

We are now in a position to understand in detail the process of energy loss by ioniza-
tion of a charged particle. On the passage of the particle, a discrete number of primary
ionizing collisions takes place which liberate electron-ion pairs in the medium. The
electron ejected can have enough energy (larger than the ionization potential of the medium)
to further ionize, producing secondary ion pairs; the sum of the two contributions is
called total ionization. Both the primary and the total ionization have been measured for
most gases, although not always in the minimum ionizing region. The total number of ion
pairs can be conveniently expressed by

$$n_T = \frac{\Delta E}{W_i} \quad ,$$

where ΔE is the total energy loss in the gas volume considered, and W_i is the effective
average energy to produce one pair. Values of W_i for different gases are given in Table 1.
No simple expression exists for the number of primary ion pairs; in the table, experimental
values of n_p for minimum ionizing particles are given, per unit length and at normal condi-
tions. As Fig. 7 shows, n_p is roughly linearly dependent on the average atomic number of
the gas, and the figure can be used to estimate the number of primary pairs for other mole-
cules (an exception is xenon). This has been done, for example, to obtain W_i for carbon
dioxide (CO_2) and isobutane (C_4H_{10}) (values in brackets in Table 1).
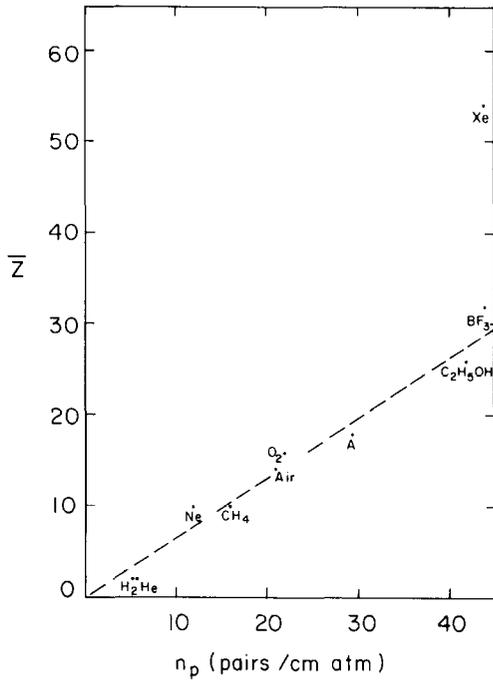
Fig. 7

Primary ionizing events pro-
duced by fast particles per
unit length at normal condi-
tions for several gases, as a
function of their average ato-
mic number (from Table 1). With
the exception of xenon, all ex-
perimental points lie around a
straight line. The plot may be
used to estimate the number of
primary pairs in other gases.

The reader should be warned that the values of W_i and of n_p listed in the table cor-
respond just to a reasonable average over results of different experimenters[12]; values
different from the averages by as much as 20-30% can be found.

A simple composition law can be used for gas mixtures; as an example, let us compute
the number of primary and total ion pairs produced in a 1 cm thick 70-30 mixture of argon-
isobutane, at normal conditions:

$$n_T = \frac{2440}{26} \, 0.7 + \frac{4500}{23} \, 0.3 \quad = 124 \text{ pairs/cm}$$

$$n_p = 29.4 \times 0.7 + 46 \times 0.3 = 34 \text{ pairs/cm} \quad .$$

In other words, we see that the average distance between primary interactions is around
300 μm at normal conditions, and that each primary produces about 2.5 secondaries on the
average.

2.8 Statistics of ion-pair production

The primary ionization encounters, being a small number of independent events, follow
Poisson-like statistics; if n is the average number of primary interactions (n = n_p), the
actual number k in one event will have a probability

$$P_k^n = \frac{n^k}{k!} \, e^{-n} \quad .$$

The inefficiency of a perfect detector is therefore given by

$$1 - \varepsilon = P_0^n = e^{-n} \quad . \tag{4}$$

In the gas mixture previously considered, the inefficiency will be around 10^{-15} for a 1 cm thick detector (n = 34), and 3.3% for a 1 mm thick detector (n = 3.4). As a matter of fact, it is from inefficiency measurements in low-pressure proportional counters that the values of n_p have been deduced. When k ion pairs are produced in a given event, simple probabilistic considerations provide the space distribution of each pair j $(1 \leq j \leq k)$ along a normalized coordinate x $(0 \leq x \leq 1)$:

$$D_j^k(x) = \frac{k!}{(k-j)!(j-1)!} (1-x)^{k-j} x^{j-1}$$

and the general expression for the space distribution of the pair j , when n is the average number produced, is obtained as follows:

$$A_j^n(x) = \sum_{k=j}^{\infty} P_k^n D_j^k(x) = \frac{x^{j-1}}{(j-1)!} n^j e^{-nx} \quad .$$

Consider, in particular, the distribution of the pair closer to one end of the detection volume,

$$A_1^n(x) = n \, e^{-nx} \quad , \tag{5}$$

which is represented in Fig. 8, for n = 34, as a function of the coordinate across a 10 mm thick detector. If the time of detection is the time of arrival of the closest electron at one end of the gap, as is often the case, the statistics of ion-pair production set an obvious limit to the time resolution of the detector. A scale of time is also given in the figure, for a collection velocity of 5 cm/μsec typical of many gases; the FWHM of the distribution is about 5 nsec. There is no hope of improving this time resolution in a gas counter, unless some averaging over the time of arrival of all electrons is realized.
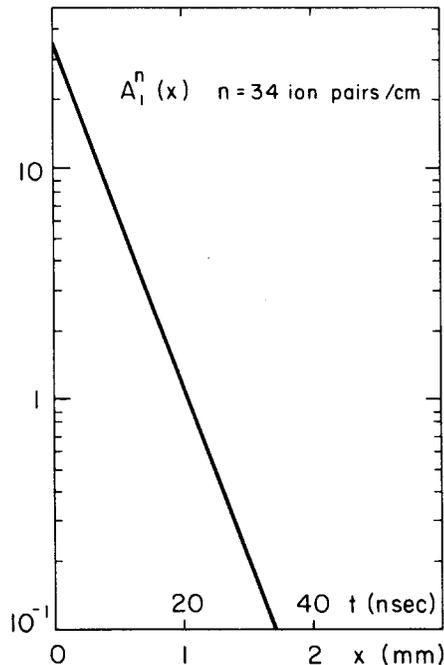

Fig. 8

Statistics of primary ion pair production: probability of finding the closest pair at a distance x from one electrode in a counter, in argon-isobutane 70-30. The corresponding electron minimum collection time is shown, for a typical drift velocity of electrons of 5 cm/μsec.

3. DETECTION OF PHOTONS

3.1 Different processes of absorption

As for charged particles, an electromagnetic interaction allows the detection of photons; in this case, however, the interaction is a single localized event. The probability of absorption can be written in terms of the cross-section σ, and the attenuation of a beam of photons traversing a thickness X of a medium having N molecules per unit volume is given by

$$I = I_0 \, e^{-\sigma NX} = I_0 \, e^{-\mu x} \quad , \tag{6}$$

where μ is the mass attenuation coefficient (normally expressed in $cm^2 \, g^{-1}$) and $x = \rho X$ is the reduced thickness of the medium, see Section 2.2. One can also define an absorption mean free path $\lambda = (\mu\rho)^{-1}$ and in this case Eq. (6) is rewritten as

$$I = I_0 \, e^{-X/\lambda} \quad . \tag{7}$$

Depending on photon energy, the interaction can follow different mechanisms. At low energies, up to several keV, the dominant process is photoelectric conversion; then Compton scattering takes over, up to energies of a few hundred keV, and at even higher energies electron-positron pair production is the most probable process (Fig. 9).
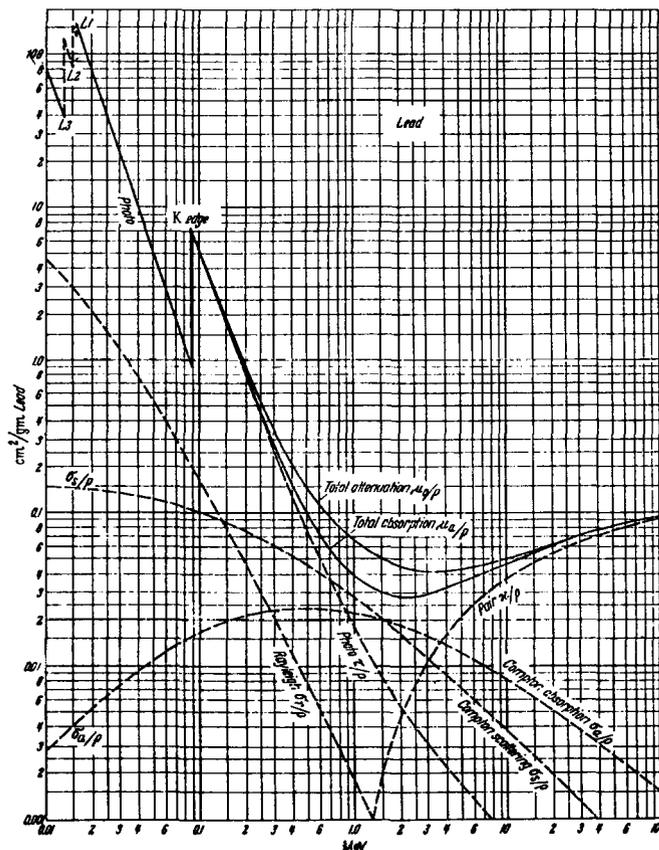

Fig. 9   Cross-section for photon absorption in lead, as a function of energy, showing the relative contribution of different processes[16])

3.2 Photoelectric absorption

We will consider this process in some detail for two reasons. Firstly, it is common practice for laboratory testing of proportional chambers to use X-ray emitting isotopes producing energy losses in the few keV region (as can be seen from Table 1, this is equal to the typical energy loss of a minimum ionizing particle in 1 cm of gas). Secondly, multi-wire proportional chambers are used as soft X-ray detectors in many applications, such as, for example, to study transition radiation, in crystal diffraction experiments, and in X-ray astronomy. A clear understanding of the detailed process of energy loss by the photoelectric effect is necessary in all these cases.

Photoelectric absorption is a quantum process involving one or more transitions in the electron shells of a molecule. Denoting by E_j the energy of a shell j, photoelectric absorption in the shell can take place only for photon energies $E_\gamma \geq E_j$ and, at a given energy, the contributions of all levels having $E_j < E_\gamma$ add up. The absorption is a maximum at the edge, and then very rapidly decreases with energy.

The binding energy of a given shell increases rapidly with atomic number, as shown in Fig. 10; precise values can be found in many textbooks (see the bibliography for this section). Figure 11, drawn using the tables of Grodstein[13], gives the photoelectric absorption coefficient as defined in the previous section, for several elements. Approximate values of the absorption edges are also shown. At a given energy, light elements have the smallest coefficient and, except for the heavier noble gases, at energies above a few keV K-edge absorption dominates. For a gas mixture or for complex molecules one can assume a simple composition rule to be valid; if p_1, p_2, ..., p_n are the percentages, in weight, of atoms 1, 2, ..., n in the mixture, the absorption coefficient of the compounds can be written as

$$\mu_{1,2\ldots n} = p_1\mu_1 + p_2\mu_2 + \ldots + p_n\mu_n \quad.$$
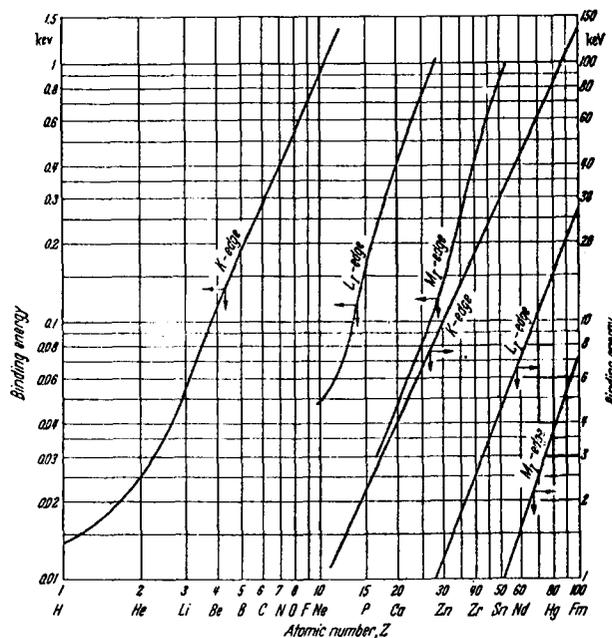

Fig. 10 Binding energy of K, L and M electron shells, as a function of atomic number[16]
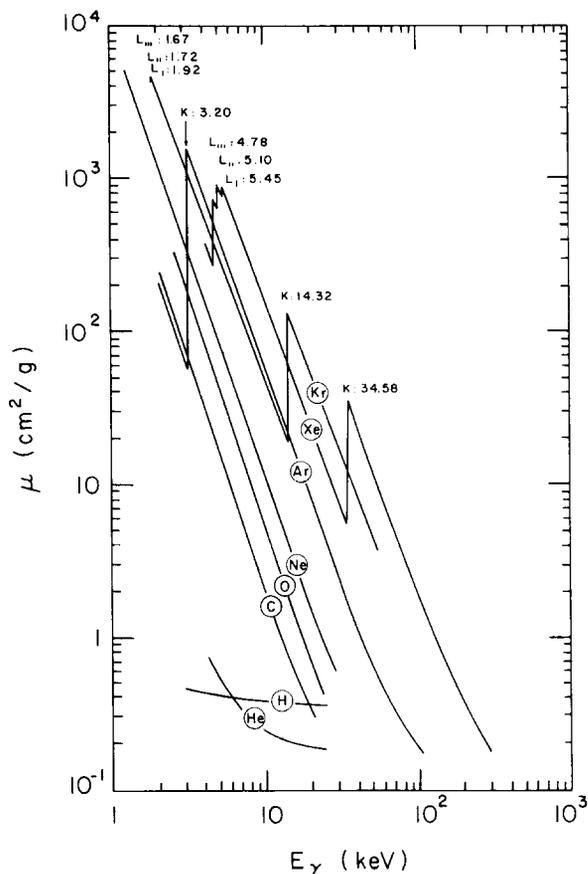
Fig. 11   Absorption coefficient versus energy
of photons, in several gases used in
proportional counters. Carbon is
included, to allow the calculation
of absorption in hydrocarbons. The
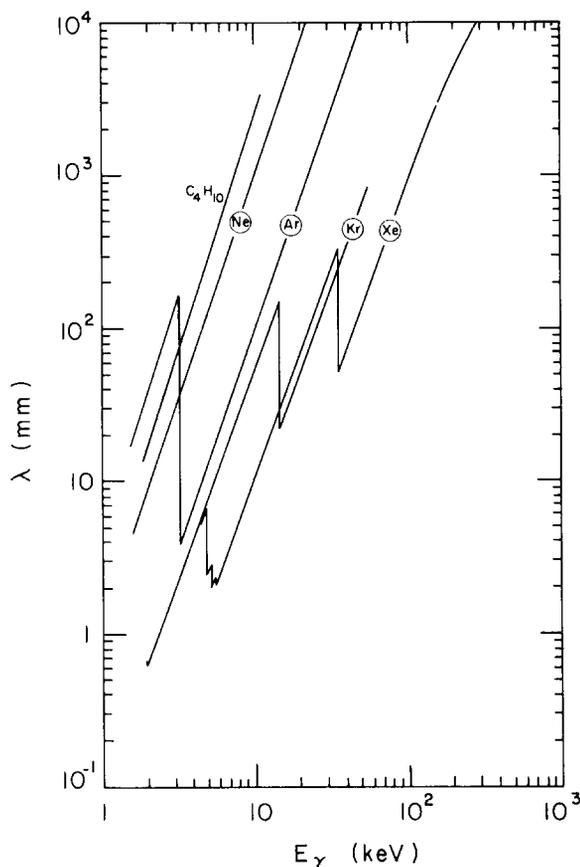figure has been drawn using the tabu-
lations of Ref. 13.

Fig. 12   Mean free path for absorption in
several gases at normal conditions,
for photons of energy E_γ (from the
tabulation in Ref. 13)

In particular, the organic vapours used as quenchers in proportional counters have a very
small absorption coefficient, since they mainly contain light elements.

Using the definition (7) one can compute the mean free path for absorption in gases
under normal conditions, as shown in Fig. 12. Notice, for example, that the absorption in
argon increases by almost two orders of magnitude when the photon energy increases over the
K-shell edge of 3.20 keV.

Absorption of a photon of energy E_γ in a shell of energy E_j results in the emission of
a photoelectron of energy $E_e = E_\gamma - E_j$; the excited molecule can then return to its ground
state mainly through two competing mechanisms:

- fluorescence, i.e. the transition of an electron from an energy shell $E_i < E_j$ into the
  j-shell, with the emission of a photon of energy $E_j - E_i$;

- radiationless transition, or Auger effect, which is an internal rearrangement involving
  several electrons from the lower energy shells, with the emission of an electron of
  energy very close to E_j.

The fraction of de-excitations producing the emission of a photon is called fluorescence yield. For the K-shell, the fluorescence yield increases with the atomic number as shown in Fig. 13 [14]. In argon, for example, about 15% of the photoelectric absorptions are followed by the emission of a photon, while in 85% of the events two electrons, of energy $E_\gamma - E_K$ and slightly smaller than E_K, respectively, are produced. The secondary photon, emitted at an energy just below the K-edge, has of course a very long mean free path for absorption and can therefore escape from the volume of detection. This produces the characteristic escape peak of argon, at an energy $E_\gamma - E_K$. In detectors where localization of the conversion point is required, the emission of a long-range photon can introduce a large error if the position is estimated with a centre-of-gravity method as is often the case. A quantitative discussion on this point can be found in Bateman et al. [15] for xenon-filled counters.

The primary photoelectron is emitted in a preferential direction, depending on its energy, as shown in Fig. 14; up to a few tens of keV, the direction of emission is roughly perpendicular to the incoming photon direction. However, as already discussed in Section 2.4, multiple scattering quickly randomizes the motion of the heavily ionizing photoelectron. The range of electrons in gases was also discussed in Section 2.5.
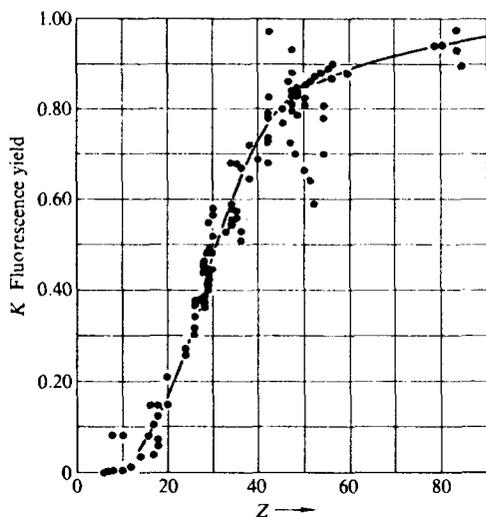

Fig. 13   Fluorescence yield of the K shell i.e. the fraction of de-excitations producing the emission of a photon, versus atomic number [14]
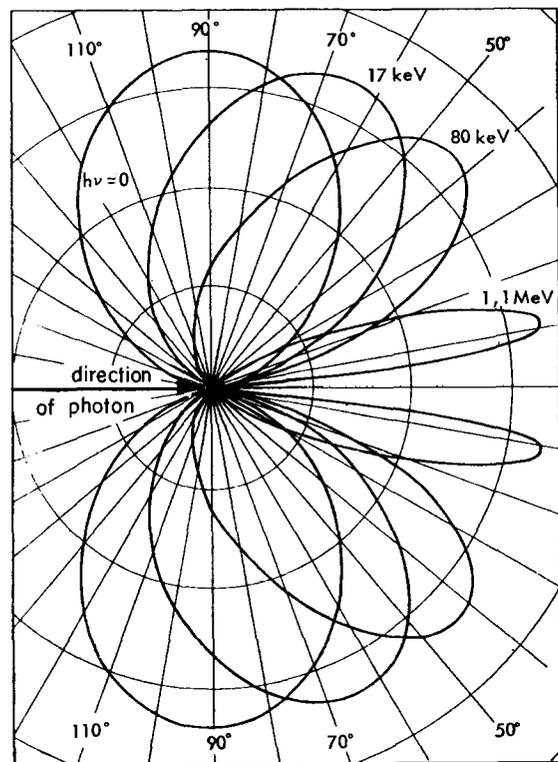
Fig. 14   Probability of emission of a photoelectron at a given angle in respect to the incoming photon direction, as a function of the quantum energy [4]

3.3 Compton scattering

When the photon energy rises well above the highest atomic energy level, Compton scattering begins to be the dominant process. The incident photon, with energy $h\nu_0$, is scattered by a quasi-free electron by an angle θ, and takes a new energy $h\nu'$ such that

$$\frac{1}{h\nu'} - \frac{1}{h\nu_0} = \frac{1}{mc^2} (1 - \cos \theta) \quad .$$

The energy of the scattered electron is $h\nu_0 - h\nu'$. Quantum-mechanical theory provides the differential cross-section and the angular distributions for this effect (see the bibliography for this section). Figure 15 shows the computed absorption coefficient for Compton scattering (coherent and incoherent), as from Ref. 13; Figs. 16a and 16b [16] show correlations between the energies and angles of diffusion, while Fig. 17 is a polar plot of the cross-section for different photon energies[16].

In a thin gas counter, it is unlikely for the scattered photon to be absorbed again; therefore, the energy deposit depends on the (unknown) angle of scattering. No energy resolution is therefore obtained in the Compton region.
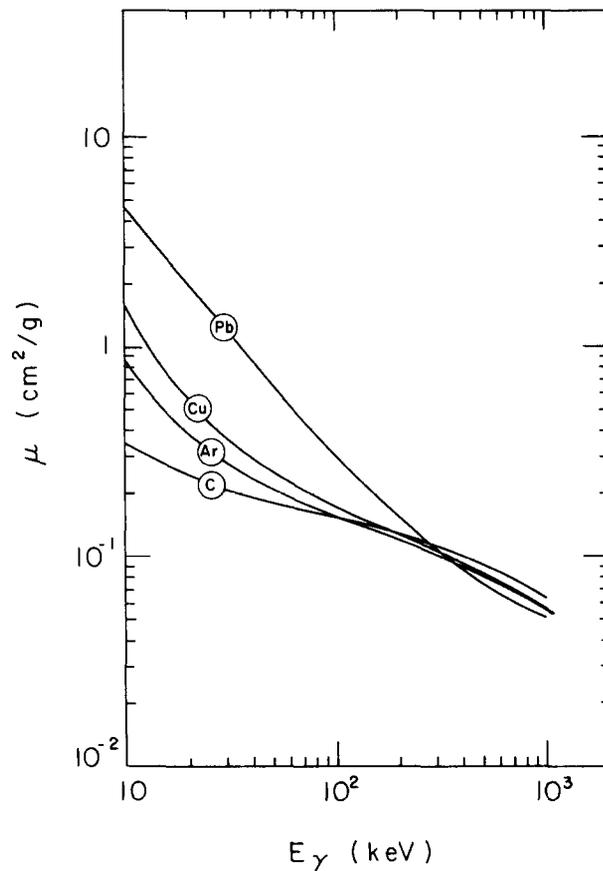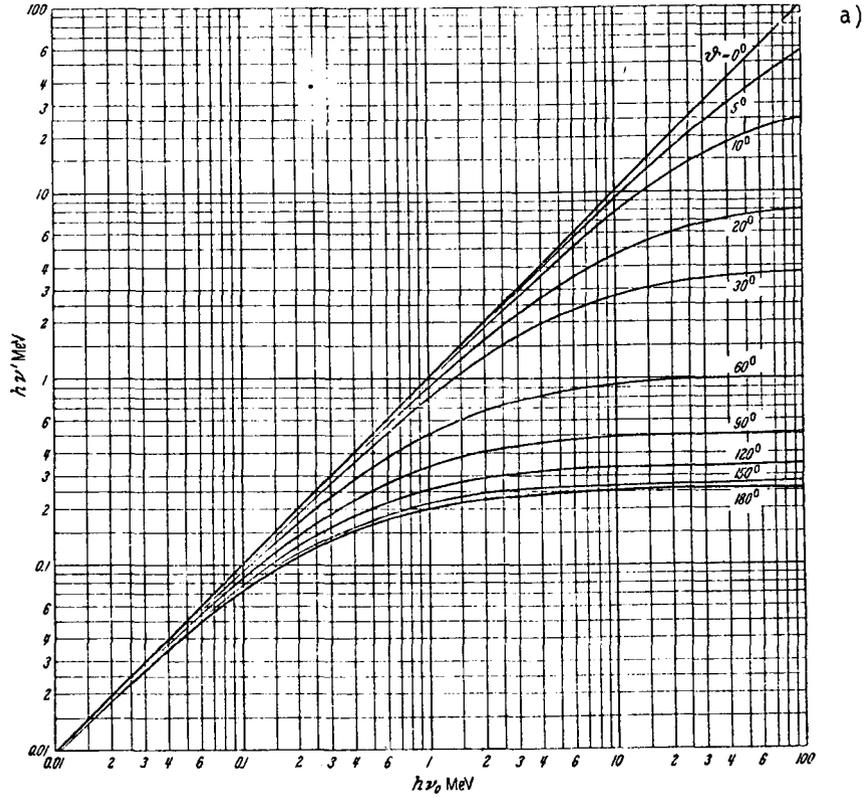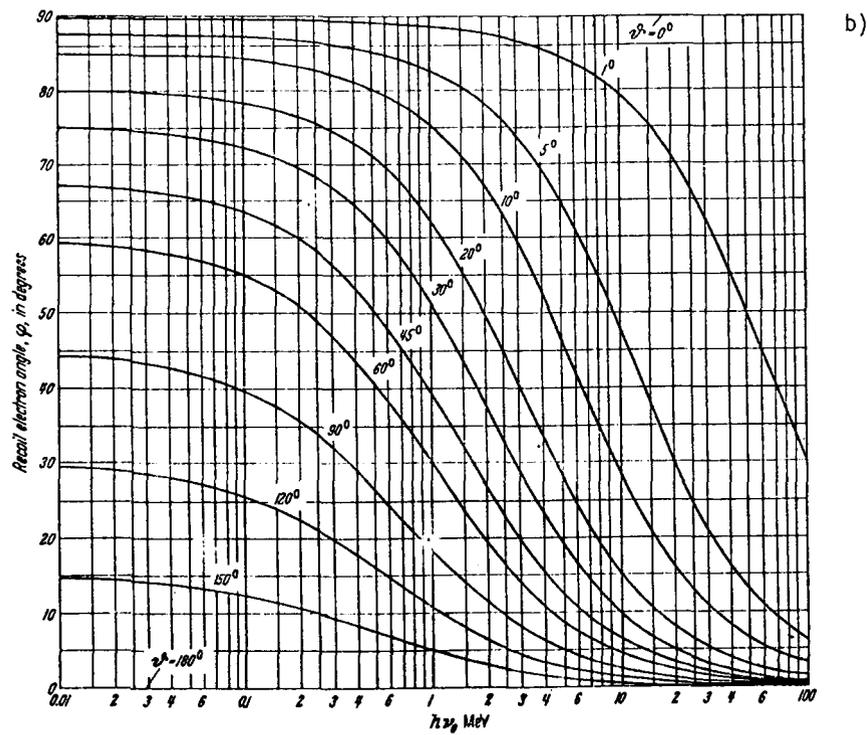

Fig. 15   Absorption coefficient for Compton
scattering (coherent and incoherent)
as a function of photon energy, for
several elements[16]

Fig. 16   Computed correlation (a) between energy hν′ and angle θ
of the Compton scattered photon, and (b) between the recoil
electron angle φ and θ, both as a function of the incident
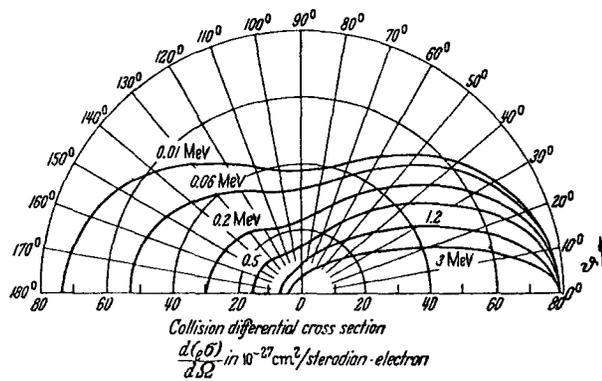photon energy hν₀ [16]

Fig. 17   Polar plot of the Compton cross-section
           as a function of the photon scattering
           angle θ, for several incident photon
           energies[16]

3.4 Pair production

Electron-positron pair production can take place at photon energies above the threshold
of 1.02 MeV (corresponding to two electron masses); Figure 18 shows the absorption coeffi-
cient due to pair production for several elements[13], while Fig. 19 gives the relative
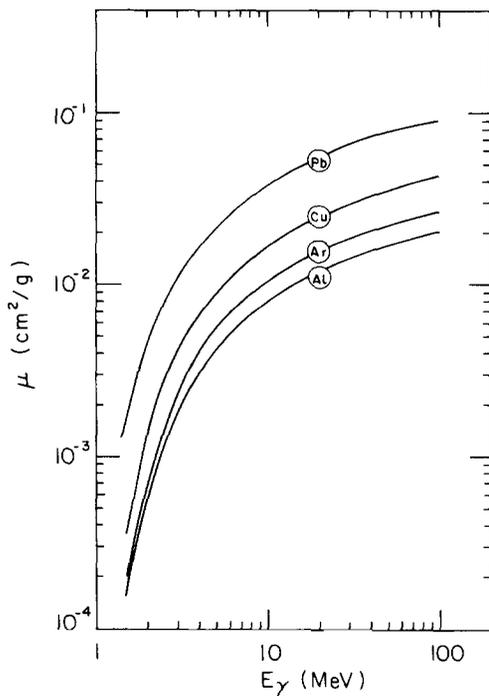
Fig. 18   Absorption coefficient for e^+e^-
           pair production in several mate-
           rials, as a function of the in-
           coming photon energy (drawn from
           the Tables of Ref. 13)

Fig. 19   Relative energy sharing between e^+
           and e^- in pair production, for
           several incoming energies (given
           in terms of the electron rest energy
           $mc^2 = 0.511$ MeV). The ordinate is
           proportional to the cross-section
           for the process, as given in the
           previous curve. (From N.A. Dyson,
           see bibliography for this section.)

energy-sharing between e^+ and e^-. In the figure, the ordinate is a quantity proportional to the differential cross-section for the process, increasing with photon energy (given in terms of the electron rest mass). B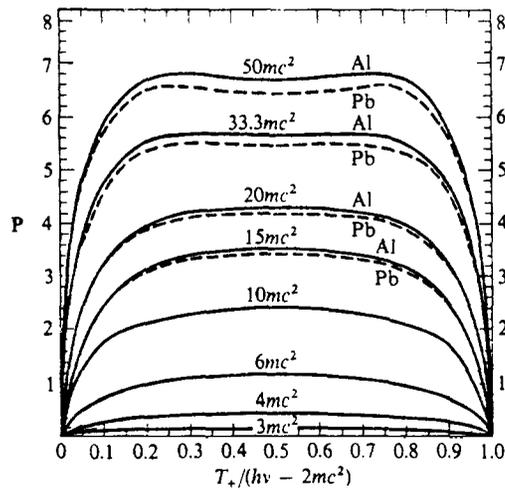ecause of the very small value of the absorption coefficient, proportional chambers are used in this energy region only to detect the pairs produced in a layer of heavy material placed in front of the chamber. Shower counters are either constructed in this way sandwiching chambers with conversion plates, or by using high density drift chambers with conversion cells of heavy material in the gas volume[17].

4. DRIFT AND DIFFUSION OF CHARGES IN GASES

4.1 Ion and electron diffusion without electric fields

Charges produced by an ionizing event quickly lose their energy in multiple collisions with the gas molecules and assume the average thermal energy distribution of the gas. Simple kinetic theory of gases provides the average value of the thermal energy, $\varepsilon_T = (3/2) \, kT \simeq 0.04$ eV at normal conditions, and the Maxwellian probability distribution of the energies

$$F(\varepsilon) = C \sqrt{\varepsilon} \, e^{-(\varepsilon/kT)} \quad . \tag{8}$$

In the absence of other effects, a localized distribution of charges diffuses by multiple collisions following a Gaussian law:

$$\frac{dN}{N} = \frac{1}{\sqrt{4\pi Dt}} \, e^{-(x^2/4Dt)} \, dx \quad , \tag{9}$$

where dN/N is the fraction of charges found in the element dx at a distance x from the origin, and after a time t; D denotes the diffusion coefficient. The root mean square (r.m.s.) of the distribution, or standard deviation, is given by

$$\sigma_x = \sqrt{2Dt} \quad \text{or} \quad \sigma_v = \sqrt{6Dt} \quad , \tag{10}$$

respectively, for a linear and a volume diffusion. As an example, Fig. 20 [18] shows the space distribution of ions produced in air, at normal conditions, after different time
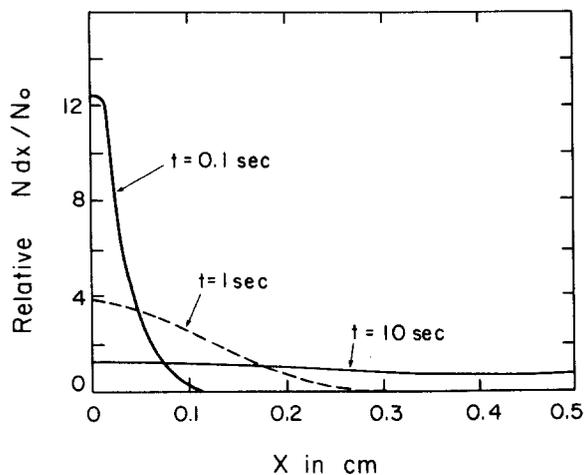

Fig. 20   Space distribution of ions produced in air, at normal conditions, after different time intervals[18]

Table 2

Classical mean free path, velocity, diffusion coefficients, and mobility for molecules, under normal conditions [18-21]

Gas	λ (cm)	u (cm/sec)	D^+ (cm^2/sec)	μ^+ (cm^2 sec^{-1} V^{-1})
H_2	1.8×10^{-5}	2×10^5	0.34	13.0
He	2.8×10^{-5}	1.4×10^5	0.26	10.2
Ar	1.0×10^{-5}	4.4×10^4	0.04	1.7
O_2	1.0×10^{-5}	5.0×10^4	0.06	2.2
H_2O	1.0×10^{-5}	7.1×10^4	0.02	0.7

intervals; values of the diffusion coefficient of several ions in their own gas are given in Table 2. During diffusion, ions collide with the gas molecules; the mean free path, average velocity, and time between collisions are also given in the table. Electrons move much faster than ions (because of their small mass), their average thermal velocity being about 10^7 cm/sec; also, because of their negligible size, their mean free path is classically four times longer than that of ions in a like gas.

A positive ion can be neutralized recombining in the gas volume with a negative charge carrier, either an electron or a negative ion, or extracting an electron at the walls. A process of charge transfer is also possible with a molecule of its own gas or with molecules of another kind having lower ionization potentials. We will reconsider this very important effect in the next section.

Electrons, instead, can be neutralized by an ion, can be attached to a molecule having electron affinity (electro-negative), or can be absorbed in the walls. The probability of attachment h is essentially zero for all noble gases and hydrogen, while it assumes finite values for other gases (see Table 3). In the table we have also shown, taking into account the previous data, the average attachment time $t = (hN)^{-1}$, if N is the number of collisions per unit time. One can see, for example, that in oxygen the average time it takes for a thermal electron to be attached is 140 nsec. The attachment coefficient is a strong function of the electric field, as will be shown later.

Table 3

Coefficient, number of collisions, and average time for electron attachment in several gases under normal conditions [12,18,21]

Gas	h	N (sec^{-1})	t (sec)
CO_2	6.2×10^{-9}	2.2×10^{11}	0.71×10^{-3}
O_2	2.5×10^{-5}	2.1×10^{11}	1.9×10^{-7}
H_2O	2.5×10^{-5}	2.8×10^{11}	1.4×10^{-7}
$C\ell$	4.8×10^{-4}	4.5×10^{11}	4.7×10^{-9}

4.2 Mobility of ions

When an electric field is applied across the gas volume, a net movement of the ions along the field direction is observed. The average velocity of this slow motion (not to be confused with the instant ion velocity) is called drift velocity w^+, and it is found to be linearly proportional to the reduced field E/P up to very high fields, P being the gas pressure. It is therefore convenient to define a quantity μ^+, called mobility, as

$$\mu^+ = \frac{w^+}{E} \ .$$ (11)

The value of the mobility is specific to each ion moving in a given gas. A constant mobility is the direct consequence of the fact that, up to very high fields, the average energy of ions is almost unmodified; we will see that this is not the case for the electrons.

A classical argument allows one to obtain the following relationship between mobility and diffusion coefficient:

$$\frac{D^+}{\mu^+} = \frac{kT}{e} \ .$$ (12)

Values of the mobility and diffusion coefficient for ions moving in a like gas were given in Table 2, while Table 4 gives the mobility of several ions drifting in gases commonly used in proportional and drift chambers[20].

Table 4

Experimental mobilities of several ions
in different gases, at normal conditions[20]

Gas	Ions	Mobility $(cm^2 \ V^{-1} \ sec^{-1})$
Ar	$(OCH_3)_2CH_2^+$	1.51
$IsoC_4H_{10}$	$(OCH_3)_2CH_2^+$	0.55
$(OCH_3)_2CH_2$	$(OCH_3)_2CH_2^+$	0.26
Ar	$IsoC_4H_{10}^+$	1.56
$IsoC_4H_{10}$	$IsoC_4H_{10}^+$	0.61
Ar	CH_4^+	1.87
CH_4	CH_4^+	2.26
Ar	CO_2^+	1.72
CO_2	CO_2^+	1.09

In a mixture of gases G_1, G_2, ..., G_n, the mobility μ_i^+ of the ion G_i^+ is given by the relationship (Blanc's law):

$$\frac{1}{\mu_i^+} = \sum_{j=1}^{n} \frac{p_j}{\mu_{ij}^+} \ ,$$ (13)

where p_j is the volume concentration of gas j in the mixture, and μ^+_{ij} the mobility of ion G^+_i in gas G_j. In gas mixtures, however, a very effective process of charge transfer takes place, and very quickly removes all ions except the ones with the lower ionization potential. Depending on the nature of the ions, and on the difference in the ionization potential (small differences increase the charge-transfer probability), it takes between 100 and 1000 collisions for an ion to transfer its charge to a molecule having a lower ionization potential. Since mean free paths for collision are of the order of 10^{-5} cm under normal conditions, see Table 2, one can assume that after a drift length between 10^{-3} p^{-1} and 10^{-2} p^{-1} cm, where p is the percentage of the lowest ionization potential molecules, the charge-exchange mechanism will have left migrating only one kind of ion. Figure 21 [20] shows the measurement of ion mobility in the mixtures argon-isobutane and argon-isobutane-methylal. As shown by the relationship (13), for a given kind of ion drifting in a gas mixture, the inverse of the mobility depends linearly on the mixture's specific weight; lines of equal slope, therefore, represent migration of the same kind of ions. In the figure, curve F represents the mobility
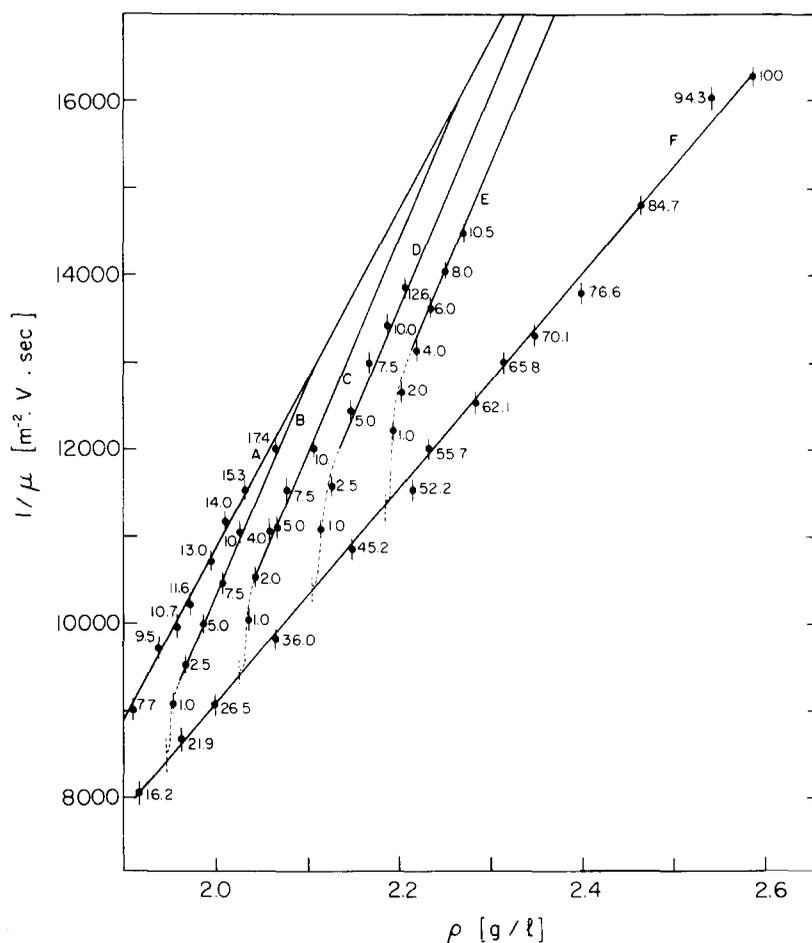

Fig. 21   Inverse mobility of ions migrating in argon-isobutane mixtures (curve F), in argon-methylal (curve A) and argon-isobutane-methylal (B = 80% argon, C = 70% argon, D = 60% argon, E = 50% argon). The numbers close to the experimental points represent the methylal concentration (curves A to E) or the isobutane concentration (curve F)[20].

of isobutane ions in variable argon-isobutane mixtures, while curves B, C, D, E represent the measured mobility of methylal ions in several argon-isobutane-methylal mixtures; the fraction of methylal in each measurement is written close to the experimental points. Clearly, in the range of electric fields considered (a few hundred to a thousand volts/cm) and for 1 cm of drift, if methylal is present in the mixture by more than 3-4% the exchange mechanism is fully efficient and only methylal ions are found to migrate. The relevance of this mechanism in the operation of proportional counters will be discussed in Section 5.3.

Ions migrating in a time t over a length x diffuse with a probability distribution expressed by Eq. (9), and the standard deviation is given by [introducing expressions (12) and (11) in (10)]:

$$\sigma_x = \sqrt{2Dt} = \sqrt{\frac{2kTw^+t}{eE}} = \sqrt{\frac{2kTx}{eE}} \quad .$$

Therefore the r.m.s. linear diffusion is independent of the nature of the ions and the gas; the variation of σ_x with the electric field, at 1 atm, is shown in Fig. 22, as well as the equivalent time dispersions σ_t for several gas mixtures[20], and 1 cm drift.

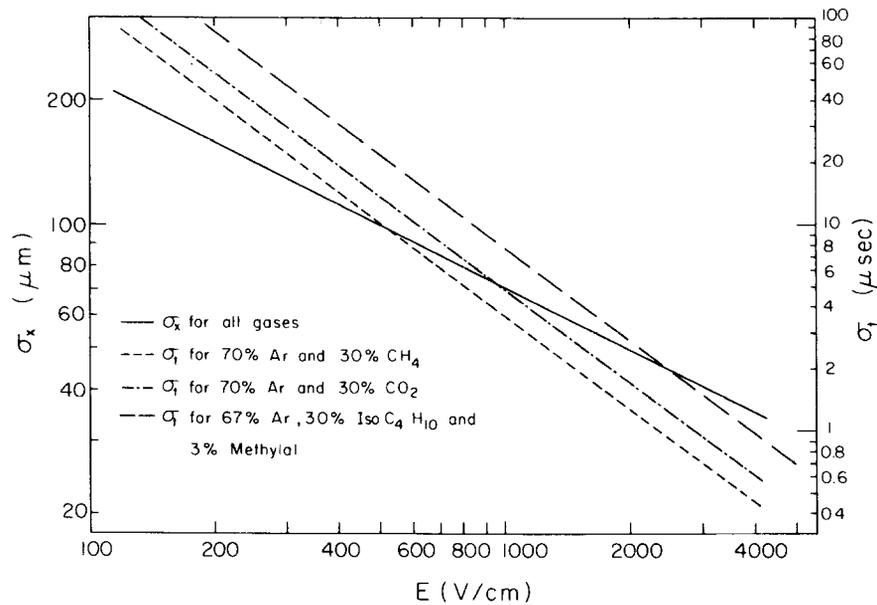
Fig. 22   Positive ion diffusion in space (σ_x) and in time (σ_t) for a drift length of 1 cm, at normal conditions as a function of electric field[20]. Notice that σ_x is the same for all gases.

4.3 Drift of electrons

A simple theory of mobility can be constructed following the same lines as for positive ions; it was found very early on, however, that except for very low fields the mobility of electrons is not constant. In fact, due to their small mass, electrons can substantially increase their energy between collisions with the gas molecules under the influence of an electric field. In a simple formulation, due to Townsend[21] one can write the drift velocity as

$$w = \frac{e}{2m} E\tau \ ,\tag{14}$$

where τ is the mean time between collisions, in general a function of the electric field E. It has been found that the collision cross-section, and therefore τ, varies for some gases very strongly with E, going through maxima and minima (Ramsauer effect). This is a consequence of the fact that the electron wavelength approaches those of the electron shells of the molecule, and complex quantum-mechanical processes take place. The energy distribution will therefore change from the original Maxwellian shape [as given by Eq. (8)] and the average energy can exceed the thermal value by several orders of magnitude, at high fields. As an example, Fig. 23 shows the energy distribution of electrons in helium at several values of the electric field[18]. Figure 24 gives instead a typical Ramsauer cross-section measurement for argon[22]; it appears that the addition of even very small fractions of another gas to pure argon can, by slightly modifying the average energy, dramatically change the drift properties, as illustrated in Fig. 25[22]. We have collected from different sources[9,12,22-24], in Figs. 26 to 30 the measured drift velocities for several pure gases and gas mixtures of interest in proportional chambers. Depending on the source, the abscissa is given in terms of the electric field at normal conditions, or of the reduced field E/P; to obtain in the last case the equivalent field at 1 atm one has to multiply the scale by 760. At high fields, typical values of w around 5 cm/μsec are obtained; use of Table 2 shows that, under similar conditions, ions are roughly a thousand times slower.
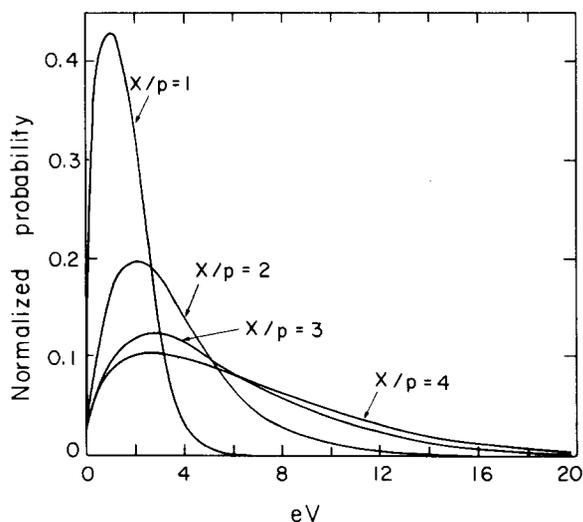

Fig. 23

Computed energy distribution of electrons in helium at different field values (X/p = 1 means 760 V/cm at atmospheric pressure)[18])
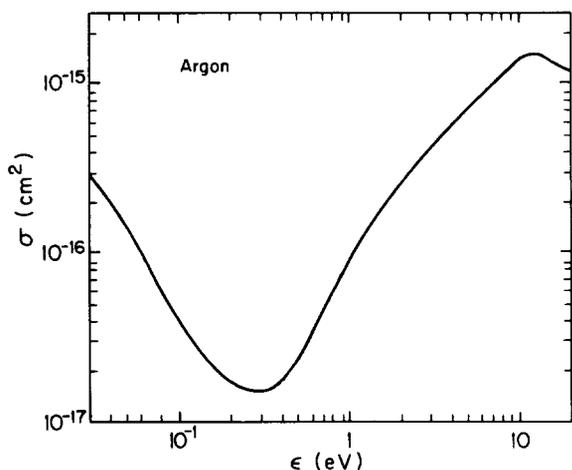
Fig. 24

Ramsauer cross-section for electrons in argon as a function of their energy[22])
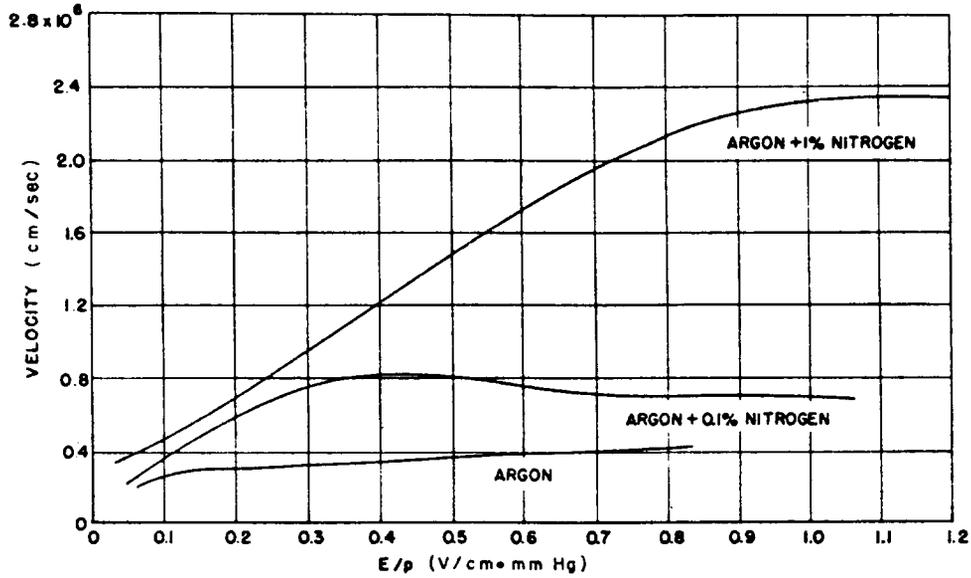
Fig. 25   Drift velocity of electrons in pure argon, and in argon with
           small added quantities of nitrogen. The very large effect on
           the velocity for small additions is apparent[22].

Fig. 26   Drift velocity of electrons in
           several gases at normal condi-
           tions[12,22,23]

Fig. 27   Drift velocity of electrons in methylal
           [(OCH₃)₂CH₂] and in ethylene (C₂H₄) [24]

Fig. 28   Drift velocity of electrons in several argon-methane
mixtures[12])
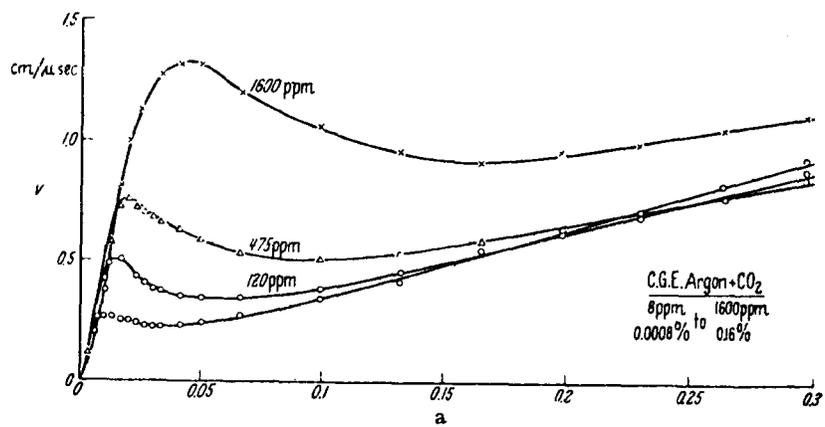
Fig. 29   Drift velocity of electrons in several argon-carbon
dioxide mixtures[12])
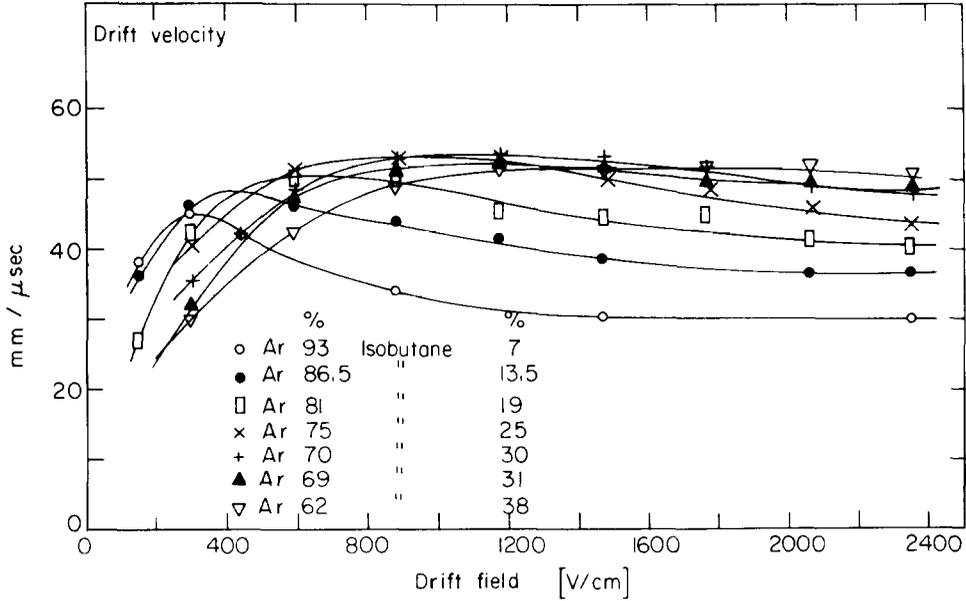
Fig. 30   Drift velocity of electrons in argon-isobutane mixtures, at
           normal conditions[9])

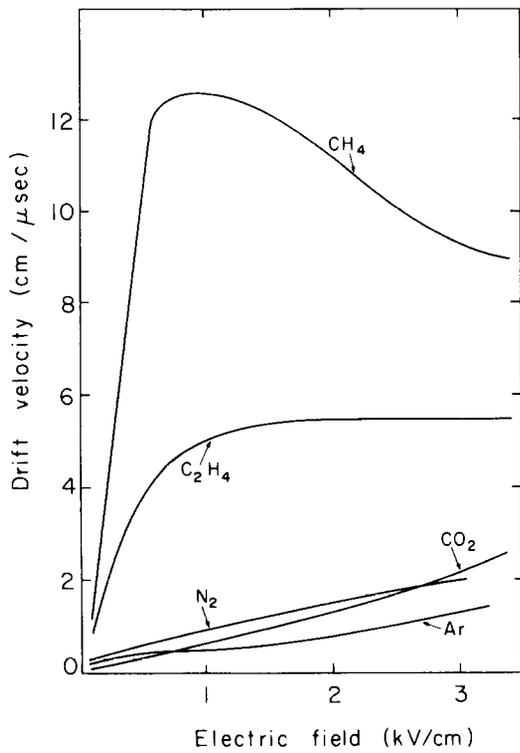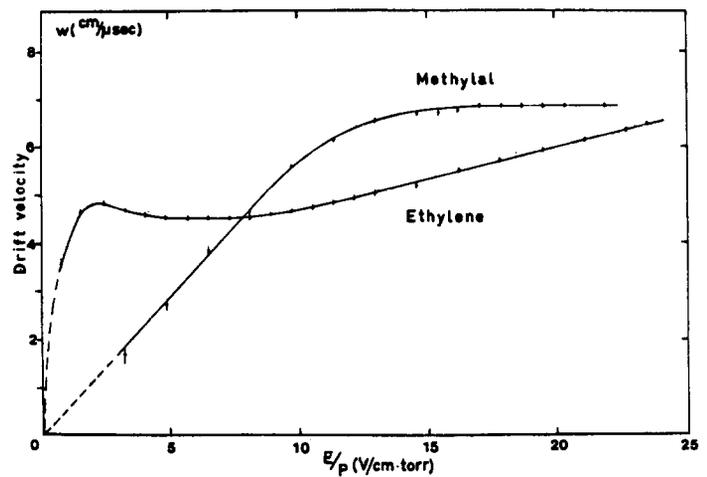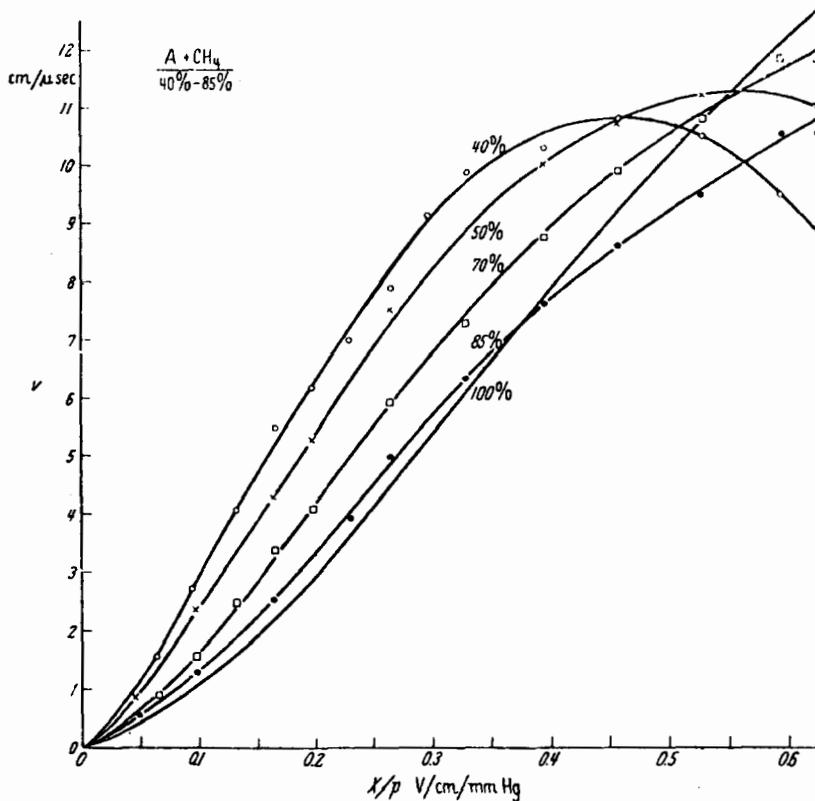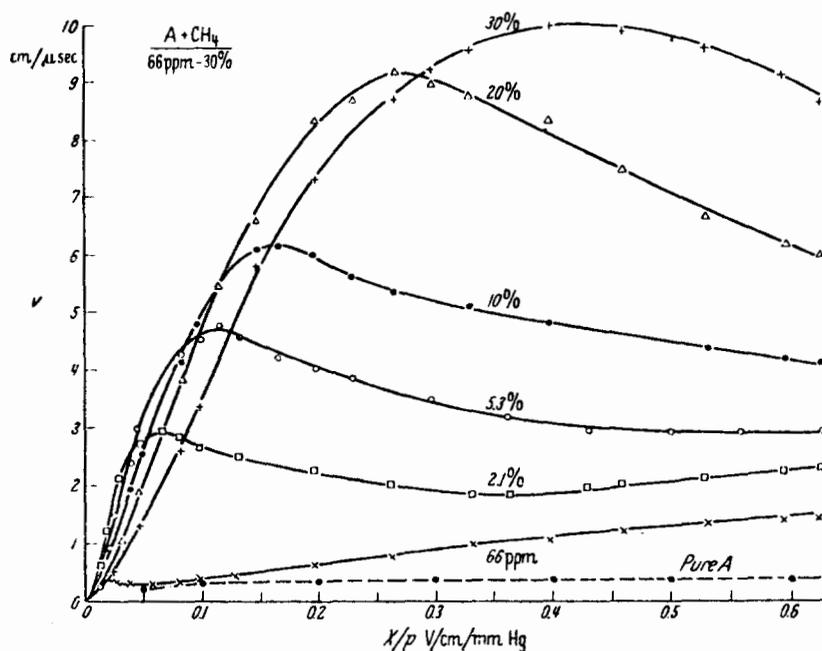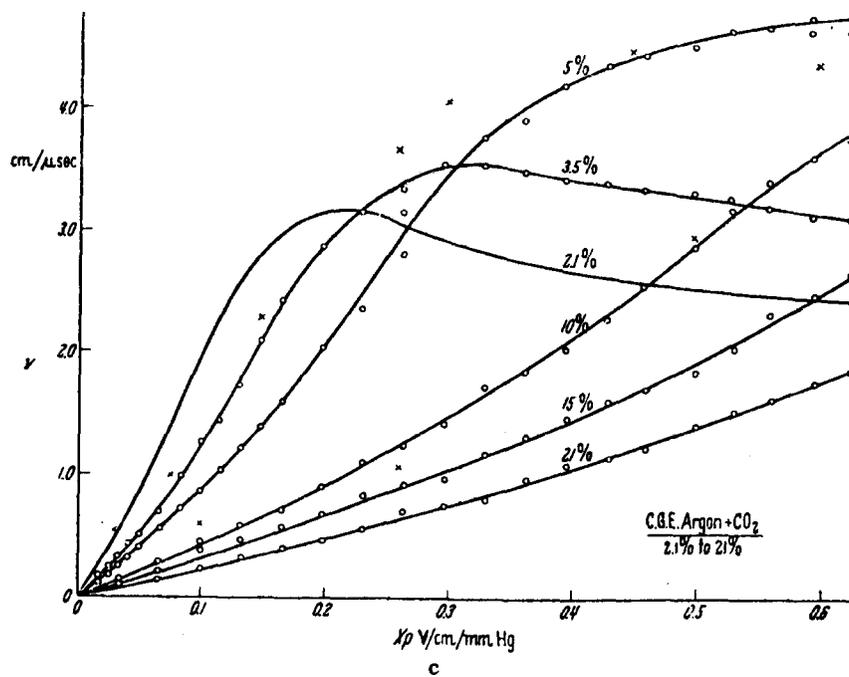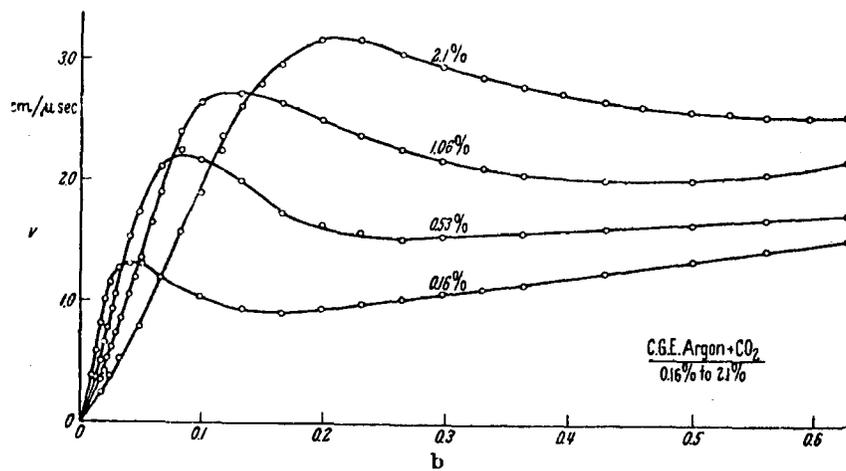A rigorous theory of electron drift in gases exists; it has recently been reviewed
for the study of drift chamber performances[25,26]. Here, we will only summarize the main
results. Under rather broad assumptions, and for fields such that only a negligible frac-
tion of the electrons get enough energy to experience ionizing collisions, one can deduce
the following expression for the energy distribution:

$$F(\varepsilon) = C \sqrt{\varepsilon} \exp \left(- \int \frac{3\Lambda(\varepsilon)\varepsilon d\varepsilon}{\left[eE\lambda(\varepsilon) \right]^2 + 3\varepsilon kT\Lambda(\varepsilon)} \right) \, , \qquad (15)$$

where the mean free path between collisions, $\lambda(\varepsilon)$, is given by

$$\lambda(\varepsilon) = \frac{1}{N\sigma(\varepsilon)} \, , \qquad (16)$$

N being the number of molecules per unit volume. At the temperature T and pressure P,
N is given by

$$N = 2.69 \times 10^{19} \, \frac{P}{760} \, \frac{273}{T} \, \text{molecules/cm}^3$$

and the cross-section $\sigma(\varepsilon)$ is deduced from the Ramsauer curve of the gas considered. In
Eq. (15), $\Lambda(\varepsilon)$ is the fraction of energy lost on each impact, or inelasticity; in other
words the amount of energy spent in processes like rotational and vibrational excitations.
If the elastic and inelastic cross-sections are known, $F(\varepsilon)$ can be computed and the drift
velocity and diffusion coefficient are given by

$$w(E) = -\frac{2}{3} \frac{eE}{m} \int \epsilon\lambda(\epsilon) \frac{\partial\left[F(\epsilon)\,u^{-1}\right]}{\partial\epsilon}\, d\epsilon \qquad (17)$$

$$D(E) = \int \frac{1}{3} u\lambda(\epsilon)F(\epsilon)d\epsilon \quad , \qquad (18)$$

where $u = \sqrt{2\epsilon/m}$ is the instant velocity of electrons of energy ϵ.

Simple rules hold for gas mixtures

$$\sigma(\epsilon) = \sum p_i\sigma_i(\epsilon) \quad \text{and} \quad \sigma(\epsilon)\Lambda(\epsilon) = \sum p_i\sigma_i(\epsilon)\Lambda_i(\epsilon)$$

with obvious meaning. It is customary to define a characteristic energy ϵ_k as follows:

$$\epsilon_k = \frac{eE\,D(E)}{w(E)} \qquad . \qquad (19)$$

Figures 31 and 32 show the computed and measured drift velocity and the characteristic energy for argon on carbon dioxide[26], while Figs. 33 and 34 give the dependence of ϵ_k on the electric field, at normal conditions, for several pure gases and gas mixtures[25].
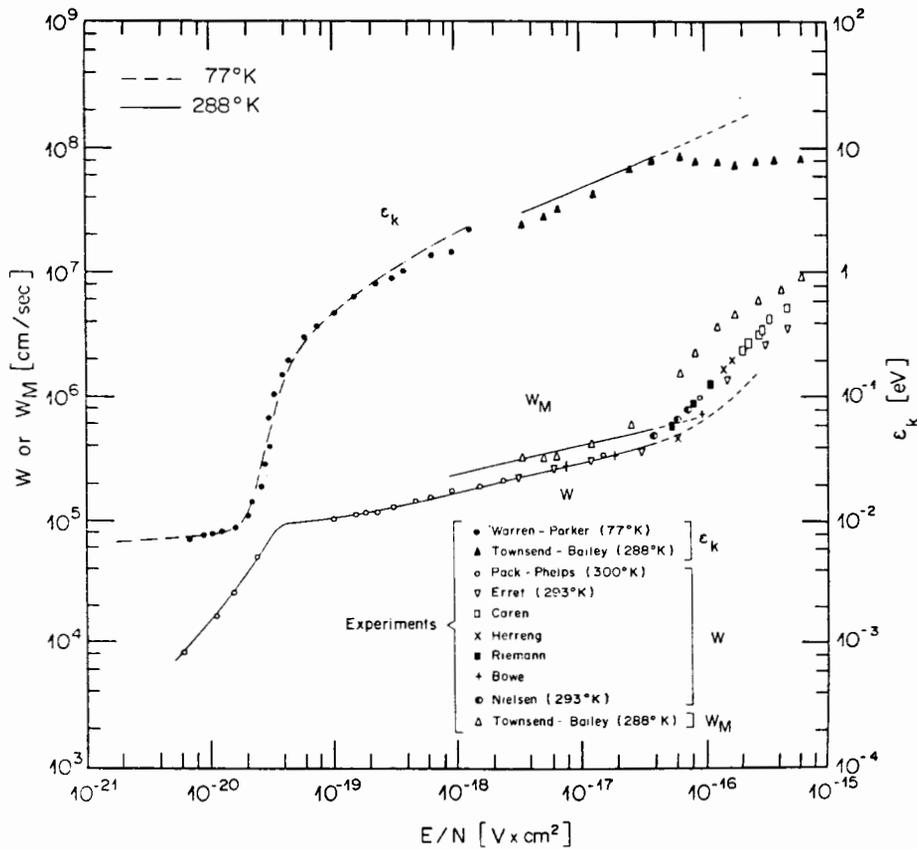
Fig. 31   Comparison of measured and computed drift velocities and characteristic energy for argon[26]
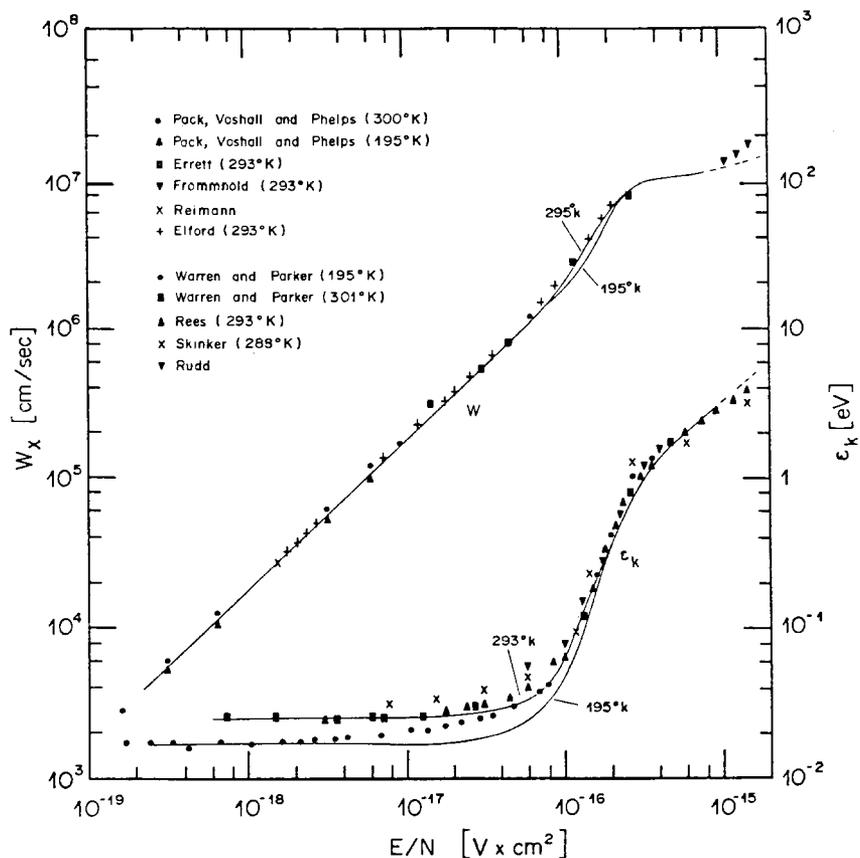
Fig. 32 Comparison of measured and computed drift velocities and charac-
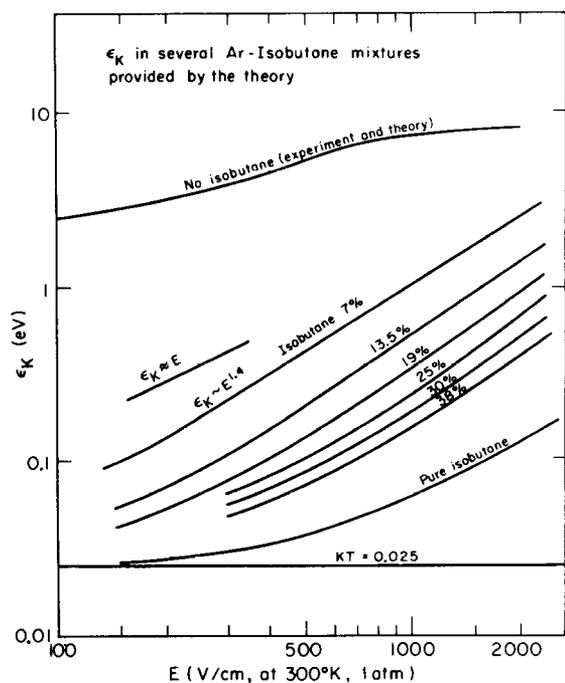teristic energy for carbon dioxide[26]

Fig. 33 Computed dependence of the charac-
teristic energy on electric field
for several argon-isobutane mix-
tures[25]
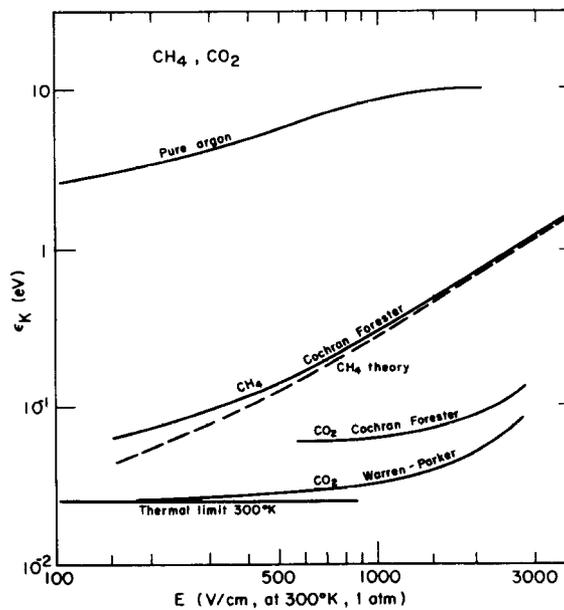
Fig. 34 Computed dependence of the charac-
teristic energy on electric field
for pure argon, carbon dioxide and
methane, from different sources[25]

4.4 Diffusion of electrons

During the drift in electric fields, electrons diffuse following a Gaussian distribution like formula (9); the change in the energy distribution due to the electric field does, of course, result in a coefficient of diffusion dependent on E, as shown by Eq. (18). Figure 35 gives, as a function of the electric field, the computed value of the standard deviation of space diffusion σ_x, as defined by formulae (10) and for 1 cm of drift[25]. The thermal limit is also shown, corresponding to a fictitious gas where the energy of electrons is not increased by the presence of the field; carbon dioxide, because of its very low characteristic energy, is very close to the thermal limit. For a 75-25 mixture of argon-isobutane, very close to the one often used in proportional and drift chambers, $\sigma_x \simeq 200$ μm independently of E. In drift chambers, one obtains the space coordinates of ionizing tracks from the measurement of the drift time, in a more or less uniform field, of the electron swarm. A small diffusion coefficient leads of course to a better accuracy; the choice of carbon dioxide is, however, often forbidden by the poor quenching properties of this gas in proportional counters (see Section 5.3) and the quoted argon-isobutane mixture is often preferred.

Notice that the limiting accuracy with which one can localize the drifting swarm is not directly given by σ_x, but by its variance, depending on the number of electrons necessary to trigger the time-measuring device. For example, if the average time of the n drifting electrons is measured, the limiting accuracy will be $\sigma_x/\sqrt{n}$. A general expression, which

Fig. 35   Computed and experimental dependence of the standard deviation of electron diffusion from the electric field for 1 cm drift, in several gases at normal conditions[25]

can be written for the case where k electrons out of n are necessary to trigger the detecting electronics[26], is
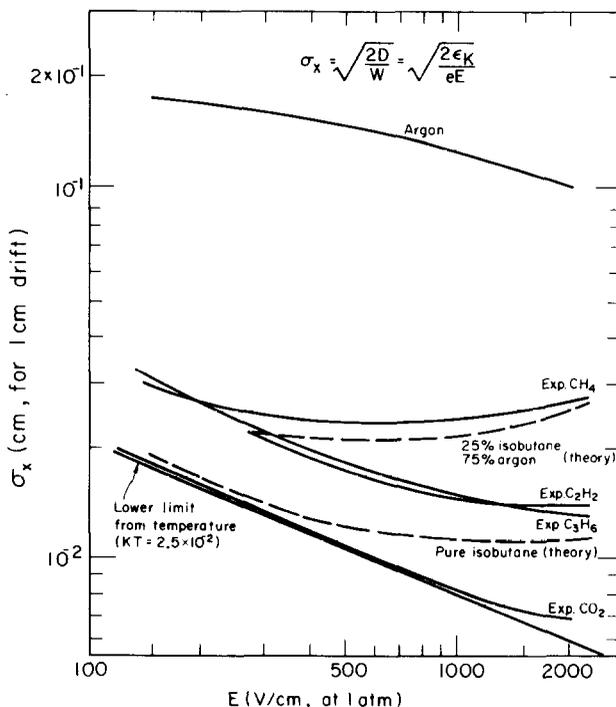
$$\sigma_k^2 = \frac{\sigma_x^2}{2 \ln n} \sum_{i=k}^{n} \frac{1}{i^2} \ .$$

For k = 1, the expression can be seen to reduce to

$$\sigma_1 = \frac{\pi}{2\sqrt{3} \ln n} \sigma_x \ , \tag{20}$$

for example, for n = 100 (typical value for 1 cm of gas), $\sigma_1 = 0.4 \ \sigma_x$. We will discuss this point further in the section devoted to high-accuracy drift chambers.

4.5 Drift of electrons in magnetic fields

The presence of a magnetic field modifies the drift properties of a swarm of electrons. The Lorentz force applied to each moving charge transforms the small segment of motion between two collisions into circular trajectories, and also modifies the energy distribution. The net effect is a reduction of the drift velocity, at least at low electric fields, and a movement of the swarm along a line different from a field line. In the case of a movement in a constant electric and magnetic field, the swarm will drift along a straight line at an angle α_H with the field lines, and with a velocity $w_H \neq w$. The same simple theory that gives the expression (14) allows one to write the effect of a magnetic field H applied in a direction perpendicular to the electric field[21] as follows:

$$w_H = \frac{w}{\sqrt{1 + \omega^2 \tau^2}} \ , \qquad \omega = \frac{eH}{m}$$

$$\tan \alpha_H = \omega \tau \ .$$

Substituting the value of τ obtained from Eq. (14), one gets an approximation which is rather good for low electric fields, as shown in Fig. 36, where experimental points are compared with calculation, for the standard gas mixture used in high-accuracy drift chambers[9], i.e. 67.2% argon, 30.3% isobutane and 2.5% methylal. At higher fields, the presence of the magnetic field modifies the energy distribution of electrons and a more rigorous analysis is necessary, similar to the one sketched in the previous section[25,26]. We will present here some experimental measurements of w_H and α_H, in the quoted gas mixture, from Ref. 9. Figure 37 shows that the drift velocity, although reduced at low electric fields, tends to reach the same saturation value for all values of magnetic field; Figure 38 gives instead the angle of drift which appears to follow almost a linear dependence on H for large electric fields. The deflection of drifting electrons has to be taken into account, especially when operating drift chambers close to or inside strong magnetic fields. Notice also, from Fig. 38, that the use of a heavier gas (xenon replacing argon) reduces the deflection of the drifting swarm.
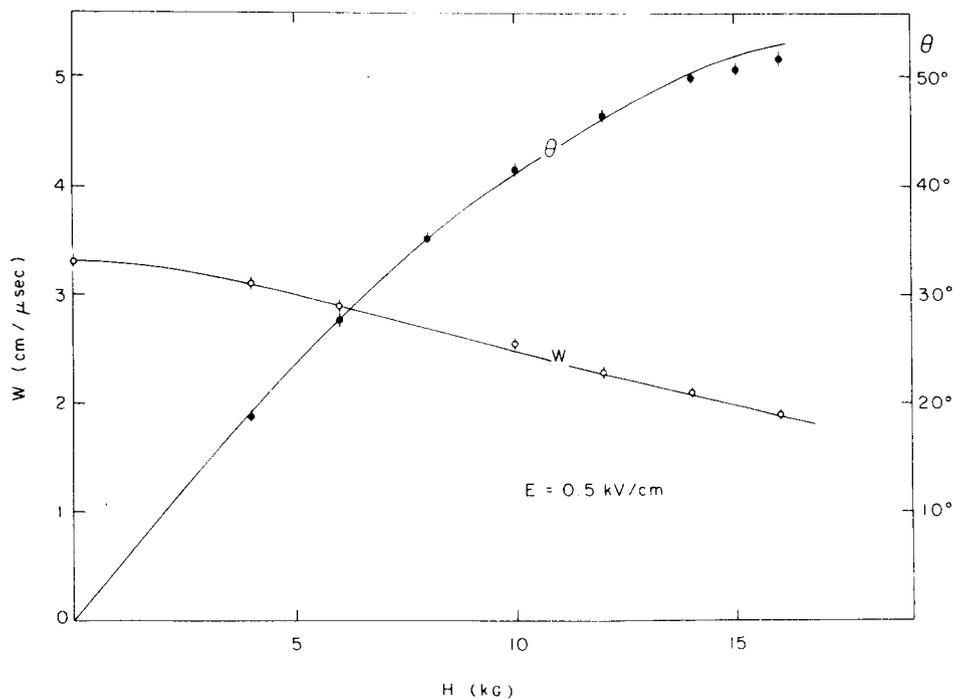
Fig. 36   Measured dependence of electron drift velocity and drift angle
from the magnetic field for a low value of electric field
(500 V/cm), in argon-isobutane-methylal (67.2%, 30.3%, 2.5%,
respectively). The curves represent the predictions of an ap-
proximated model[9].
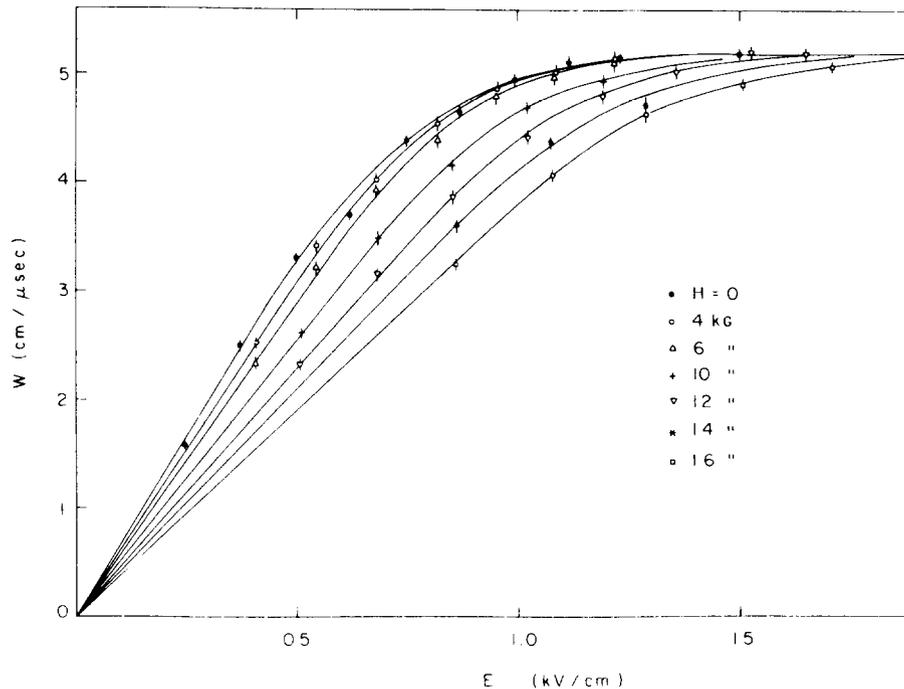
Fig. 37   Measured drift velocity of electrons, in the direction of the
motion, as a function of electric field for several values of the
magnetic field (perpendicular to the plane of drift)[9].
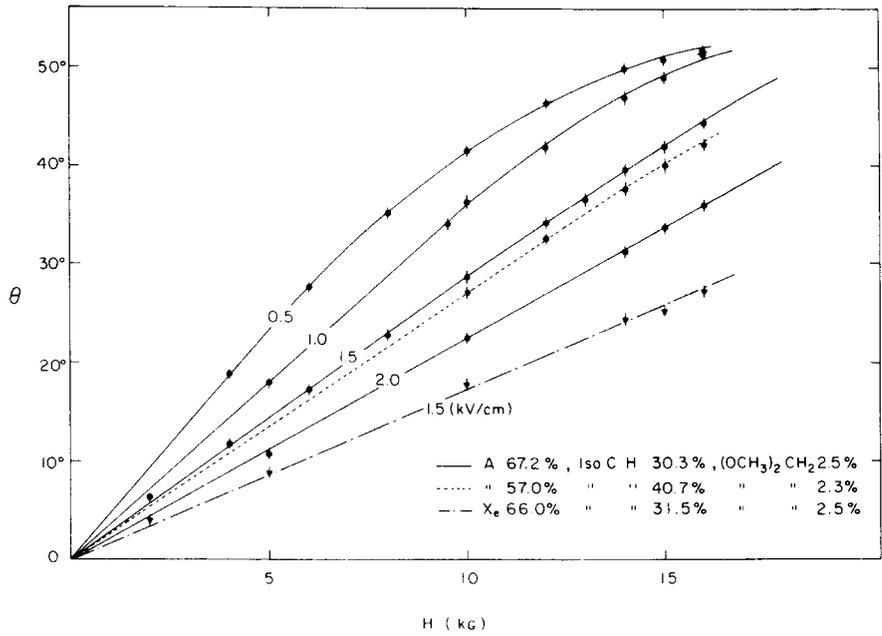
Fig. 38   Measured drift angle (angle between the electric field and
          the drift directions) as a function of electric and magnetic
          field strength[9].

4.6   Effect of electronegative gases

Addition to an inert gas of even small quantities of electronegative products sensibly
modifies the drift properties due to electron capture. The attachment coefficients h for
several gases, in the absence of electric field, were given in Table 3; the cross-section
for electron capture varies, however, with the electron energy, as shown in Fig. 39 for
oxygen. Figures 40 and 41 show instead the attachment coefficient as a function of the
reduced field E/p for air and chlorine in argon; similar curves for many other gases can
be found in Refs. 18 and 22.
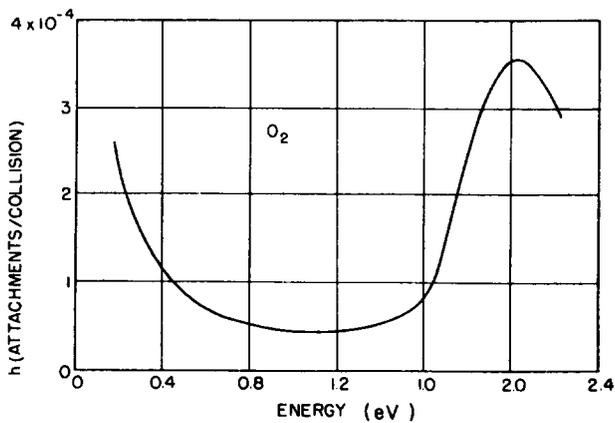
Fig. 39   Attachment coefficient for electrons
          in oxygen, as a function of electron
          energy[22].
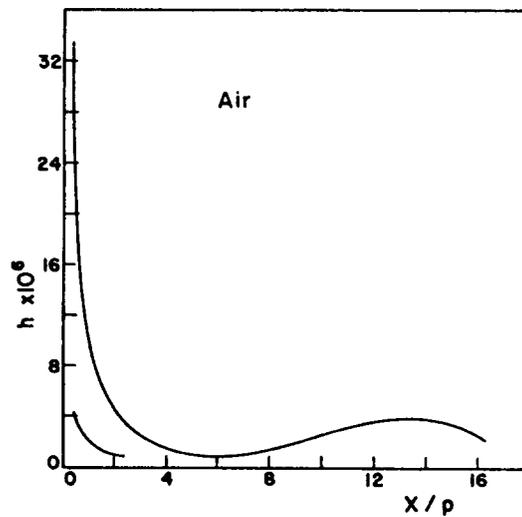
Fig. 40   Attachment coefficient for elec-
          trons in air as a function of
          the reduced electric field[22].
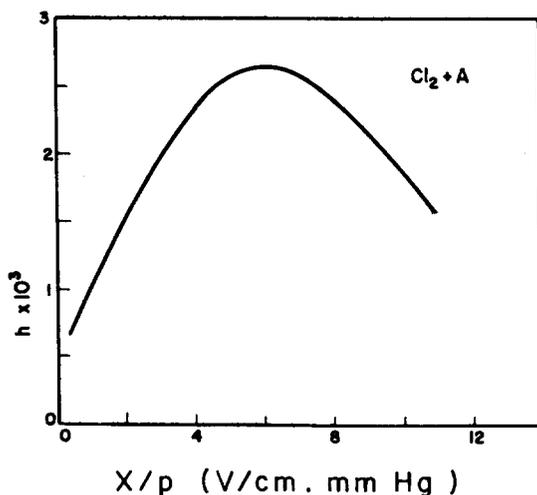
Fig. 41   Attachment coefficient for elec-
trons in an argon-chlorine mix-
ture[22].

The presence of electronegative polluants, mostly oxygen and water, in proportional counters reduces the detected pulse height because of electron capture. Let p be the fraction of electronegative polluant in the gas, λ and u the electron mean free path and instant velocity, respectively, and w the drift velocity. The number of collisions per unit time of an electron with the electronegative molecules is therefore up/λ and the probability of attachment

$$\frac{hup}{\lambda w} = \frac{1}{\lambda_c} \quad , \tag{21}$$

where λ_c is the mean free path for capture. Substituting in Eq. (21) the expression (16) and the definition of u , one gets

$$\lambda_c = \sqrt{\frac{m}{2\epsilon}} \frac{w}{Nhp\sigma(\epsilon)} \quad .$$

The loss of electrons in a swarm drifting in constant fields across a distance x is given by

$$\frac{n}{n_0} = e^{-x/\lambda_c} \quad . \tag{22}$$

As an example, let us consider the effect of air pollution in pure argon, at normal conditions. We shall assume that the presence of the pollution does not modify the energy distribution of electrons in argon. (This is, as we have seen, a rather naïve assumption!) From previous figures one gets, at E = 500 V/cm: ϵ_k = 6 eV = 1.9×10^{-12} erg, w = 4×10^5 cm/sec, $\sigma(\epsilon_k)$ = 5×10^{-16} cm^2, and for air h = 2×10^{-5}. From Eq. (21), therefore, $p\lambda_c \approx 2.5 \times 10^{-2}$ cm. A 1% pollution of air in argon, therefore, will remove about 33% of the migrating electrons, per cm of drift, due to electron capture.

4.7 High electric fields: excitation and ionization

Increasing the electric field above a few kV per cm, more and more electrons can re-
ceive enough energy between two collisions to produce inelastic phenomena, excitation of
various kinds, and ionization. Even a simplified description of the energy dependence of
inelastic processes would exceed the purpose of these notes; here, we will only summarize
some phenomenological aspects which are relevant for understanding the operation of propor-
tional counters. A molecule can have many characteristic modes of excitation, increasing
in number and complexity for polyatomic molecules. In particular, noble gases can only be
excited through photon absorption or emission, while weakly-bound polyatomic molecules, for
example the hydrocarbons used in proportional counters as a quencher, have radiationless
transitions of a rotational and vibrational nature. Addition of an organic vapour to noble
gases will therefore allow the dissipation of a good fraction of energy in radiationless
transition, and, as will be discussed later, this is essential for high gain and stable
operation of proportional counters.

When the energy of an electron increases over the first ionization potential of the
gas E_i (see Table 1), the result of the impact can be an ion pair, while the primary elec-
tron continues its trip. The probability of ionization is rapidly increasing above thresh-
old and has a maximum, for most gases, around 100 eV (see Fig. 42). Approximate curves
showing the fraction of energy going into different processes, as a function of the reduced
field E/P, are given in Fig. 43 for argon, nitrogen and hydrogen[18]. In the figure curves
labelled El represent the elastic impacts, EV the vibrational excitations, EE the excita-
tion leading to photon emission, and I the ionizations.

Consider now a single electron drifting in a strong electric field; at a given time,
it will have an energy ε with a probability given by the appropriate energy distribution
function $F(\varepsilon)$. When, following the statistical fluctuations in the energy increase between
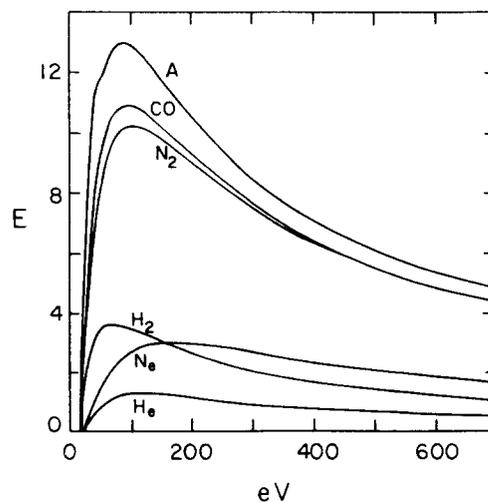
Fig. 42   Probability of ionization
by the impact of electrons,
as a function of their energy,
in several gases[22]
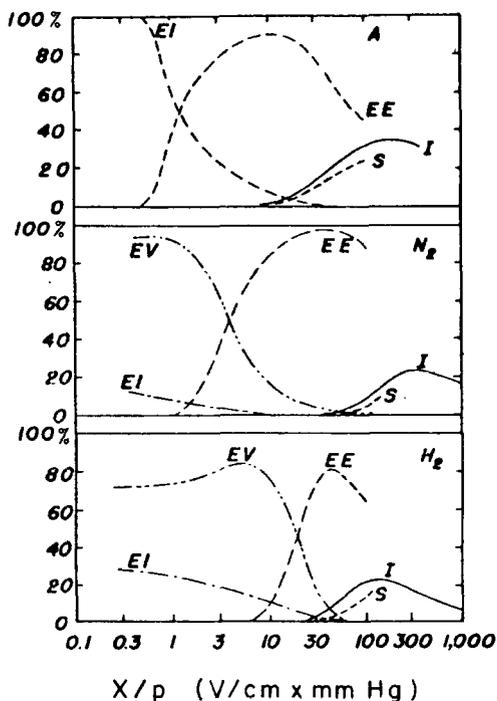
Fig. 43

Approximate curves showing the fraction of energy
going into different processes in argon, nitrogen
and hydrogen as a function of the reduced electric
field[18]. In the figure, El represents the elastic
impacts, EV the vibrational excitations, EE the ex-
citations leading to photon emission and I the ioni-
zations.

collisions, the electron gains an energy in excess of the ionization potential, an ioniza-
tion encounter may occur. The mean free path for ionization is defined as the average dis-
tance an electron has to travel before getting a chance to become involved in an ionizing
collision. The inverse of the mean free path for ionization, α, is called the first Townsend
coefficient and represents the number of ion pairs produced per unit length of drift. Values
of α/P as a function of the reduced electric field E/P are given in Fig. 44, while Fig. 45
shows the dependence of α/P on the energy of the electrons ε.
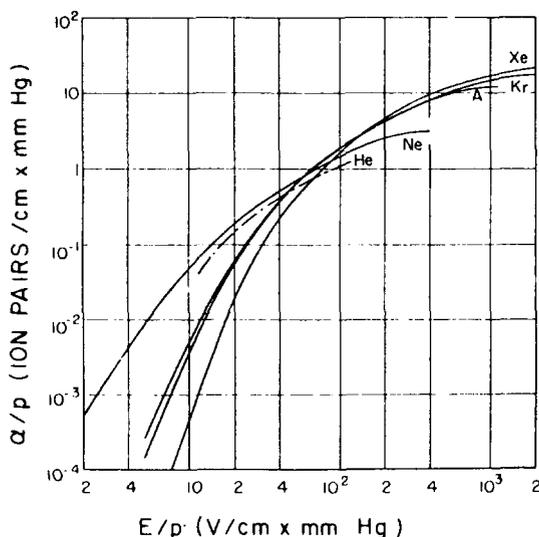
Fig. 44   First Townsend coefficient as a func-
tion of the reduced electric field,
for noble gases[22]
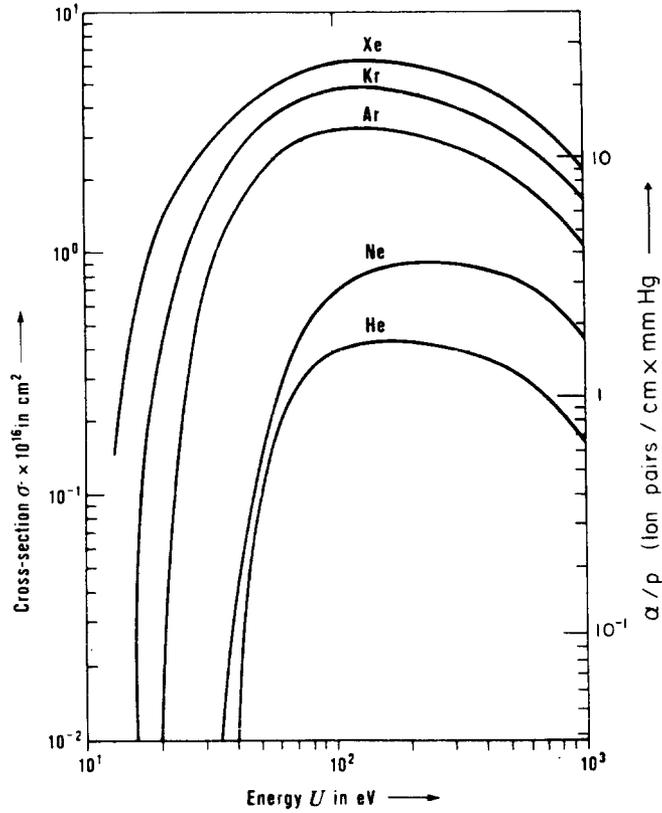
Fig. 45   Cross-section and first Townsend coefficient
as a function of electron energy, for noble
gases[28])

The process of ionization by collision is the basis of the avalanche multiplication in proportional counters. Consider an electron liberated in a region of uniform electric field. After a mean free path α^{-1}, one electron-ion pair will be produced, and two electrons will continue the drift to generate, again after one mean free path, two other ion pairs and so on. If n is the number of electrons at a given position, after a path dx, the increase in the number will be

$$dn = n\alpha\ dx$$

and, by integration

$$n = n_0\,e^{\alpha x} \quad \text{or} \quad M = \frac{n}{n_0} = e^{\alpha x} \quad . \tag{23}$$

M represents the multiplication factor. In the general case of a non-uniform electric field, $\alpha = \alpha(x)$, Eq. (23) has to be modified in the following way:

$$M = \exp\left[\int_{x_1}^{x_2}\alpha(x)\ dx\right] . \tag{24}$$
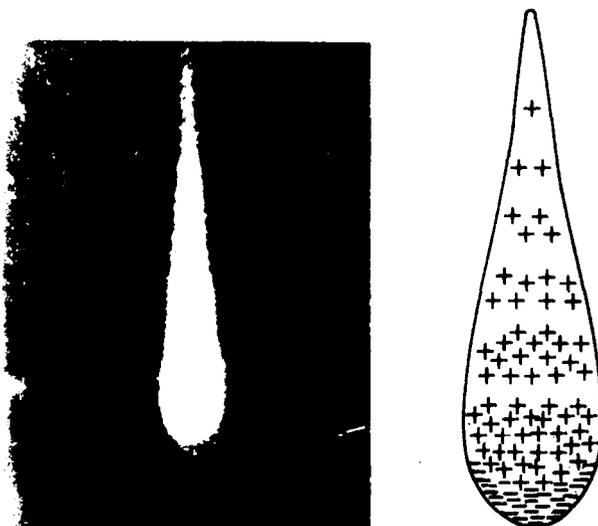
Fig. 46   Drop-like shape of an avalanche, showing the posi-
tive ions left behind the fast electron front.
The photograph shows the actual avalanche shape,
as made visible in a cloud chamber by droplets
condensing around ions[18].

If one remembers now the big difference in the drift velocity of ions and electrons --
about a factor of thousand -- and the diffusion of migrating charges in the gas, the follow-
ing picture of an avalanche multiplication appears (see Fig. 46): at a given instant, all
electrons are situated in the front of a drop-like distribution of charges, with a tail of
positive ions behind, decreasing in number and lateral extension; half of the total ions
are contained in the front part, since they have just been produced in the last mean free
path. Knowing the dependence of the Townsend coefficient on the electric field, one can
compute the multiplication factor for any field geometry. Many approximated analytic ex-
pressions exist for α, valid in different regions of E; for a summary see Ref. 25. We
will mention here a simple approximation, due to Korff[27] and valid for low values of α

$$\frac{\alpha}{P} = A\,e^{-BP/E} \quad ,$$

where A and B are constants as given in Table 5. In the same region one can assume the
coefficient to be linearly dependent on the energy of the electrons

$$\alpha = kN\varepsilon \ , \tag{25}$$

N being the number of molecules per unit volume; the values of k are given in Table 5.
The limits of the approximation can readily be estimated by inspection of Figs. 44 and 45.
Knowing the dependence of α on the electric field, the multiplication factor can be com-
puted for any field configuration; an example will be given in Section 5.1. No simple
rules can be given for the behaviour of the first Townsend coefficient in gas mixtures. As
a general trend, addition to a noble gas of a polyatomic gas or vapour increases the value
of the field necessary to obtain a given value of α; Figure 47 shows the effect of adding
several vapours to argon[28]. An exponential approximation is still possible, at least for
small values of α.

Table 5

Parameters appearing in Korff's approximated
expression for the first Townsend coefficient α [27]

Gas	A (cm^{-1} Torr)	B (V cm^{-1} Torr)	k (cm^2 V^{-1})
He	3	34	0.11×10^{-17}
Ne	4	100	0.14×10^{-17}
Ar	14	180	1.81×10^{-17}
Xe	26	350	
CO$_2$	20	466	
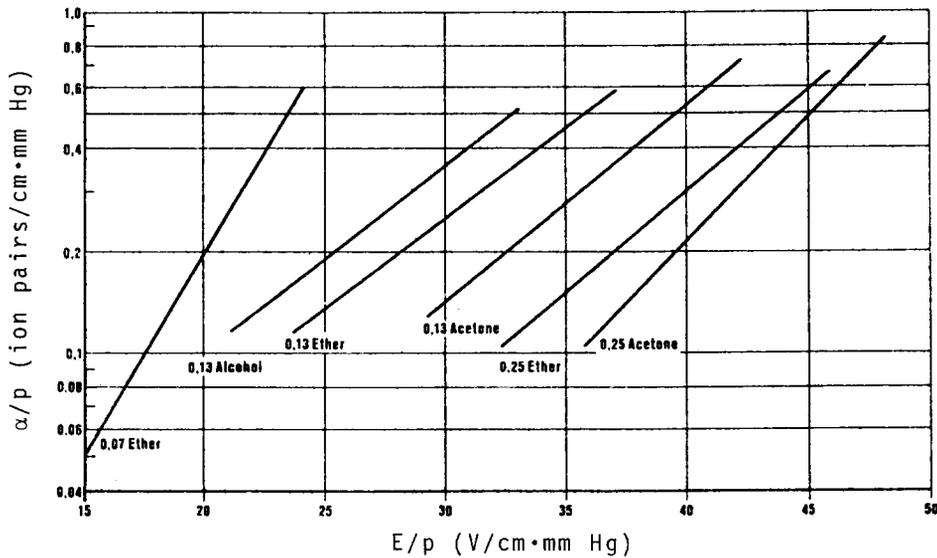
Fig. 47   First Townsend coefficient as a function of the reduced electric
field, for several vapours added to argon[28].

The multiplication factor cannot be increased at will. Secondary processes, like
photon emission inducing the generation of avalanches spread over the gas volume, and space-
charge deformation of the electric field (which is strongly increased near the front of the
avalanche), eventually result in a spark breakdown. A phenomenological limit for multipli-
cation before breakdown is given by the Raether condition

$$\alpha x \sim 20, \tag{26}$$

or $M \sim 10^8$; the statistical distribution of the energy of electrons, and therefore of M,
in general does not allow one to operate at average gains above $\sim 10^6$ if one wants to avoid
breakdowns. Notice also that by increasing the gap thickness, the Raether condition will
be met at decreasing values of α; in other words, for a given field strength, the break-
down probability increases with the gap thickness.

5. PROPORTIONAL COUNTERS

5.1 Basic operation

Consider a thin layer of gas, for example 1 cm of argon at normal conditions, between two flat electrodes. A minimum ionizing particle will release (see Section 2.7) about 120 ion pairs; if this charge is collected at one electrode, the detected signal will be

$$V = \frac{ne}{C} \; ,$$

which, for n = 120 and a typical system capacitance C = 10 pF, gives V $\sim$ 2 μV; this is so far below any possibility of detection. If, however, a strong electric field is applied between the electrodes, avalanche multiplication can occur, boosting the signal amplitude by several orders of magnitude. This kind of parallel plane detector suffers, however, from severe limitations. The detected signal, to start with, depends on the avalanche length, i.e. on the point where the original charge has been produced: no proportionality can be obtained between the energy deposit and the detected signal. Also, because of the uniform value of α over the thickness, the Raether condition (26) is readily met for some electrons in the energy distribution: only moderate gains can be obtained before breakdown, except under very special conditions[29]. A cylindrical coaxial geometry allows one to overcome the quoted limitations (Fig. 48). A thin metal wire is stretched on the axis of a conducting cylinder and insulated from it so that a difference of potential can be applied between the electrodes. The polarity is chosen so that the central wire is positive in respect to the outer cylinder. The electric field in the system is a maximum at the surface of the anode wire and rapidly decreases, as r^{-1}, towards the cathode; using thin wires, very high values of the field can be obtained close to the anode. The operation of the counter will then be as follows. In most of the region where the charges are produced by the primary interaction processes, the electric field only makes electrons drift towards the anode and, of course, positive ions towards the cathode. But very close to the anode, normally at a few wire radii, the field gets strong enough so that multiplication starts; a typical drop-like avalanche develops with all electrons in the front and ions behind.
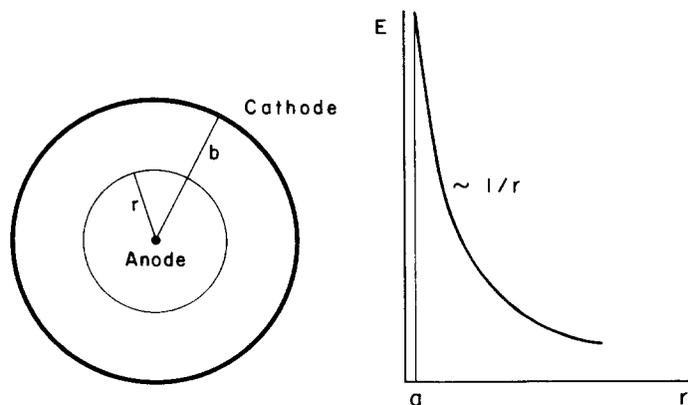
Fig. 48   The coaxial cylindrical proportional counter, and the shape of the electric field around the thin anode. Only very close to the anode the field grows high enough to allow avalanche multiplication.
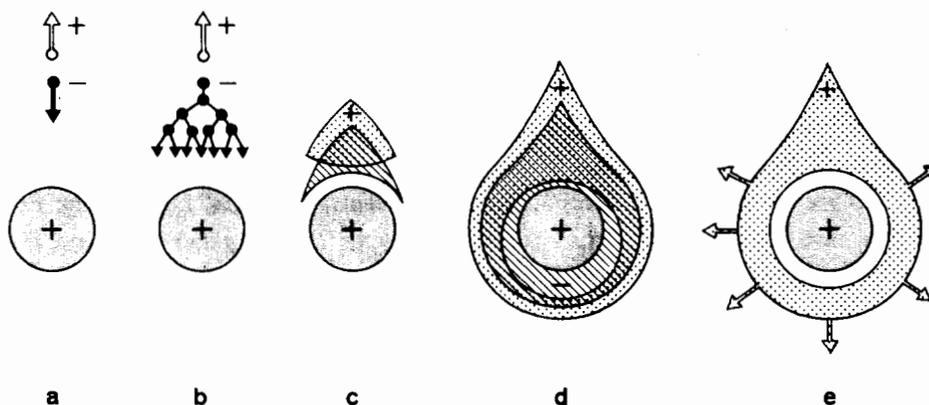
Fig. 49   Time development of an avalanche in a proportional counter[30]. A single
           primary electron proceeds towards the anode, in regions of increasingly
           high fields, experiencing ionizing collisions; due to the lateral dif-
           fusion, a drop-like avalanche, surrounding the wire, develops. Electrons
           are collected in a very short time (1 nsec or so) and a cloud of positive
           ions is left, slowly migrating towards the cathode.

Because of lateral diffusion and the small radius of the anode, the avalanche surrounds the
wire as shown in Fig. 49 [30]; electrons are collected and positive ions (half of them
produced in the last mean free path) begin to drift towards the cathode.

Figure 50 shows how the detected charge depends on the potential difference V_0 between
anode and cathode. At very low voltages, charges begin to be collected but recombination
is still the dominant process; then full collection begins and the counter is said to
operate in the ionization chamber mode. At a certain voltage, called threshold voltage V_T,
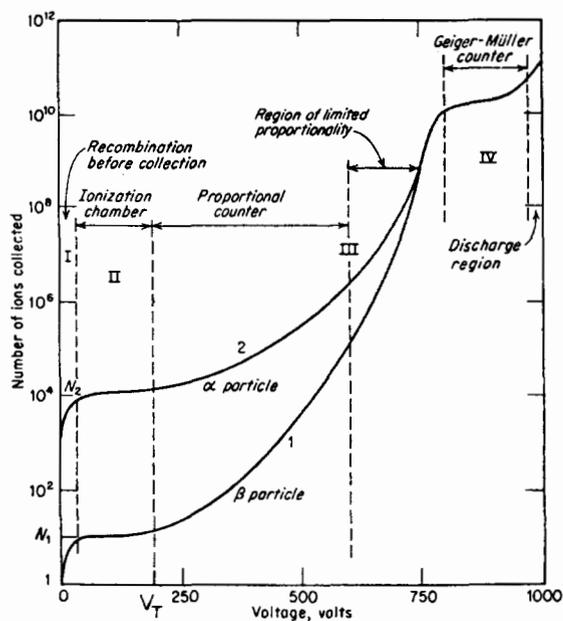
Fig. 50   Gain-voltage characteristics for a
           proportional counter, showing the
           different regions of operation
           (from W. Price, see bibliography
           for Sections 2 and 3).

the electric field close to the surface of the anode is large enough to begin the process of multiplication. Increasing V_0 above V_T, gains in excess of 10^4 can be obtained, still having the detected charge proportional, through a multiplication factor M, to the original deposited charge. At even higher voltages, however, this proportionality is gradually lost, as a consequence of the electric field distortions due to the large space charge built around the anode. This region of limited proportionality eventually ends in a region of saturated gain, where the same signal is detected independently of the original ionizing event. Proceeding even further, the photon emission process outlined in Section 4.7 begins to propagate avalanches in the counter, and the full length of the anode wire is surrounded by a sheath of electrons and ions: this is the typical Geiger-Müller operation.

In the development of multiwire proportional chambers, in order to reduce the cost and complexity of the electronics, very often one tends to work at the highest possible gains, without entering into the Geiger-Müller region which would introduce prohibitive dead-times for the counter (see later), i.e. either in the semiproportional or in the saturated mode. The maximum amplification is limited, of course, by discharge or spark breakdown; the maximum gain that can be obtained before breakdown depends on the gas used (see later).

Let a and b then be the radii of anode and cathode; at a distance r from the centre, the electric field and potential can be written as

$$E(r) = \frac{CV_0}{2\pi\epsilon_0} \frac{1}{r}$$

$$V(r) = \frac{CV_0}{2\pi\epsilon_0} \ln \frac{r}{a} , \qquad \text{where } C = \frac{2\pi\epsilon_0}{\ln (b/a)} , \tag{27}$$

$V_0 = V(b)$ is the over-all potential difference and $V(a) = 0$; C is the capacitance per unit length of the system and ϵ_0 is the dielectric constant (for gases $\epsilon_0 \simeq 8.85$ pF/m). Following Rose and Korff[27,31] we will compute the multiplication factor of a proportional counter, within the limits of the approximation (25). If $1/\alpha$ is the mean free path for ionization, the average energy ϵ obtained by an electron from the electric field between collisions is E/α; using the explicit value of E and expression (25) one gets

$$\epsilon = \sqrt{\frac{CV_0}{2\pi\epsilon_0 kN} \frac{1}{r}}$$

and therefore

$$\alpha(r) = \sqrt{\frac{kNCV_0}{2\pi\epsilon_0} \frac{1}{r}} . \tag{28}$$

The multiplication factor can then be obtained from the definition (24). To fix the limits of integration, we will assume that avalanche multiplication begins at a distance r_c from the centre, where the electric field exceeds a critical value E_c:

$$M = \exp\left[\int_a^{r_c} \alpha(r) \, dr\right] . \tag{29}$$

Recalling the definition of threshold voltage V_T, one can write

$$E_c = \frac{CV_T}{2\pi\varepsilon_0} \frac{1}{a} \quad \text{and} \quad \frac{r_c}{a} = \frac{V_0}{V_T} \quad . \tag{30}$$

Substituting Eq. (28) in Eq. (29), integrating and using Eq. (30) one gets to the two alternative expressions:

$$M = \exp\left[2\sqrt{\frac{kNCV_0 a}{2\pi\varepsilon_0}} \left(\sqrt{\frac{V_0}{V_T}} - 1 \right) \right] \tag{31}$$

or

$$M = \exp\left[\sqrt{2kNE_c} \; a \sqrt{\frac{V_0}{V_T}} \left(\sqrt{\frac{V_0}{V_T}} - 1 \right) \right] \quad . \tag{31'}$$

For $V_0 \gg V_T$, the gain is seen to depend exponentially on the charge per unit length $Q = CV_0$;

$$M = K e^{CV_0} , \tag{32}$$

having introduced expression (30) in (31) and approximating the term in parenthesis to $(V_0/V_T)^{1/2}$. Once the threshold voltage has been determined, using the value of k given in Table 5, the multiplication factor can be computed and compared with the measurements; Figure 51 (from Ref. 31) shows that the agreement is excellent at least for moderate gains.
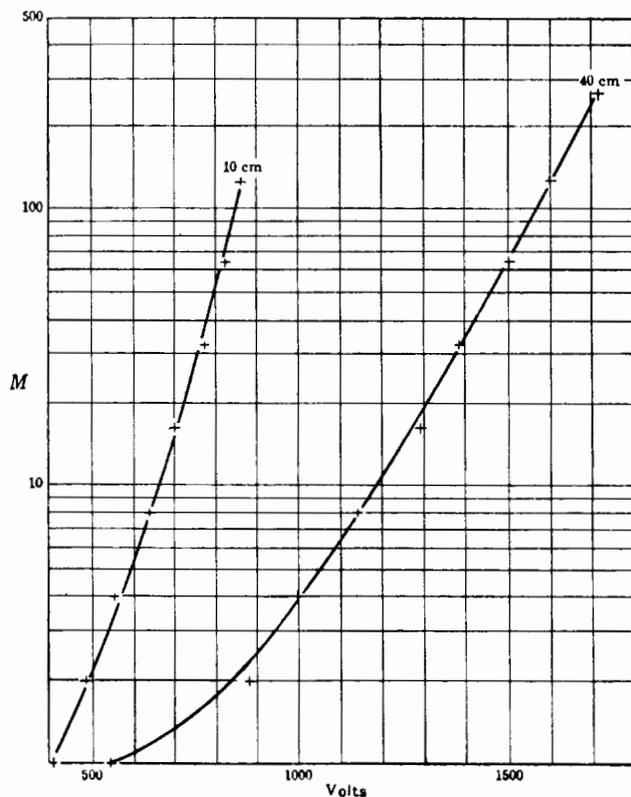

Fig. 51 Comparison between the computed [through expression (31)] and the measured multiplication factor in argon-filled proportional counters[31]. The two curves refer to the indicated gas pressures.

For higher values above 10^4 , the approximation used for α is not justified; in Ref. 25 a summary of calculations by different authors is given. For a qualitative understanding of the proportional counters' operation, however, either expressions (31), (31') or (32) are quite sufficient.

5.2 Time development of the signal

We can now analyse in detail the time development of the avalanche and of the detected signal. As shown in Fig. 49, the whole process begins at a few wire radii, i.e. typically at less than 50 μm from the anode surface. Taking a typical value of 5 cm/μsec for the drift velocity of electrons in this region, it appears that the whole process of multiplication will take place in less than 1 nsec: at that instant, electrons have been collected on the anode and the positive ion sheath will drift towards the cathode at decreasing velocity. The detected signal, negative on the anode and positive on the cathode, is the consequence of the change in energy of the system due to the movement of charges. Simple electrostatic considerations show that if a charge Q is moved by dr, in a system of total capacitance ℓC (ℓ is the length of the counter), the induced signal is

$$dv = \frac{Q}{\ell C V_0} \frac{dV}{dr} dr \quad . \tag{33}$$

Electrons in the avalanche are produced very close to the anode (half of them in the last mean free path); therefore their contribution to the total signal will be very small: positive ions, instead, drift across the counter and generate most of the signal. Assuming that all charges are produced at a distance λ from the wire, the electron and ion contributions to the signal on the anode will be, respectively,

$$v^- = - \frac{Q}{\ell C V_0} \int_a^{a+\lambda} \frac{dV}{dr} dr = - \frac{Q}{2\pi\varepsilon_0\ell} \ln \frac{a + \lambda}{a}$$

and

$$v^+ = \frac{Q}{\ell C V_0} \int_{a+\lambda}^{b} \frac{dV}{dr} dr = - \frac{Q}{2\pi\varepsilon_0\ell} \ln \frac{b}{a + \lambda} \quad .$$

The total maximum signal induced on the anode is seen to be

$$v = v^+ + v^- = - \frac{Q}{2\pi\varepsilon_0\ell} \ln \frac{b}{a} = - \frac{Q}{\ell C}$$

and the ratio of the two contributions is

$$\frac{v^-}{v^+} = \frac{\ln (a + \lambda) - \ln a}{\ln b - \ln (a + \lambda)} \quad .$$

Typical values for a counter are a = 10 μm, λ = 1 μm, and b = 10 mm; substituting in the previous expression one finds that the electron contribution to the signal is about 1% of the total. It is therefore, in general, neglected for all practical purposes. The time development of the signal can easily be computed assuming that ions leaving the surface of

the wire with constant mobility are the only contribution. In this case, integration of formula (33) gives for the signal induced on the anode

$$v(t) = -\int_0^t dv = -\frac{Q}{2\pi\varepsilon_0\ell} \ln \frac{r(t)}{a} \quad . \tag{34}$$

From the definition of mobility, Eq. (11), it follows that

$$\frac{dr}{dt} = \mu^+ \frac{E}{P} = \frac{\mu^+ CV_0}{2\pi\varepsilon_0 P} \frac{1}{r}$$

and therefore

$$\int_a^r r \, dr = \frac{\mu^+ CV_0}{2\pi\varepsilon_0 P} \int_0^t dt \quad \text{or} \quad r(t) = \left(a^2 + \frac{\mu^+ CV_0}{\pi\varepsilon_0 P} t\right)^{\frac{1}{2}} \quad .$$

Substituting in Eq. (34) one gets

$$v(t) = -\frac{Q}{4\pi\varepsilon_0\ell} \ln \left(1 + \frac{\mu^+ CV_0}{\pi\varepsilon_0 Pa^2} t\right) = -\frac{Q}{4\pi\varepsilon_0\ell} \ln \left(1 + \frac{t}{t_0}\right) . \tag{35}$$

The total drift time of the ions, T, is obtained from the condition $r(T) = b$, and is

$$T = \frac{\pi\varepsilon_0 P(b^2 - a^2)}{\mu^+ CV_0} \tag{36}$$

and it is easily seen that $v(T) = -Q/\ell C$ as it should be. As an example, let us consider an argon-filled counter under normal conditions, and with $a = 10$ μm, $b = 8$ mm; it follows from Eqs. (27) that $C = 8$ pF/m. From Table 2, $\mu^+ = 1.7$ cm^2 sec^{-1} V^{-1} atm^{-1}; for a typical operational voltage $V_0 = 3$ kV, one gets $T = 550$ μsec. The time growth of the signal is very fast at the beginning, as shown in Fig. 52; from Eq. (35) one can see that

$$v\left(\frac{a}{b} T\right) \simeq \frac{Q}{2\ell C} \quad ,$$

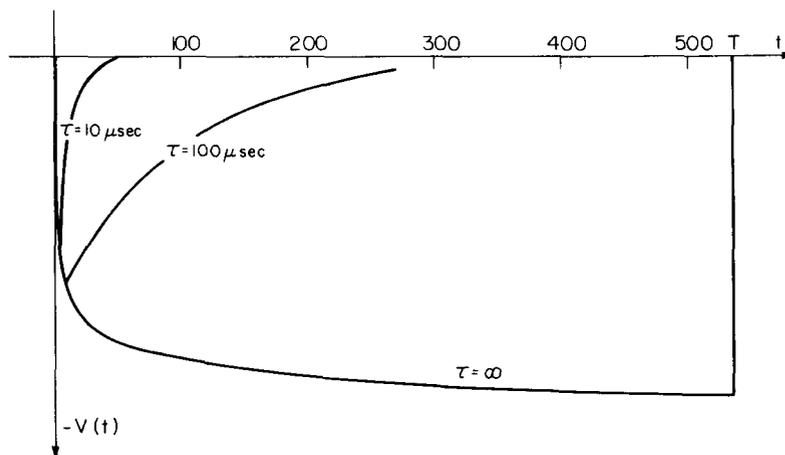Fig. 52   Time development of the pulse in a proportional counter; T is the total drift time of positive ions from anode to cathode. The pulse shape obtained with several differentiation time constants is also shown.

hence half of the signal is developed after one thousandth of the total time, about 700 nsec in the example. It is therefore normal practice to terminate the counter with a resistor R, such that the signal is differentiated with a time constant $\tau = RC$; very short pulses can be obtained using low impedance terminations, with the aim of increasing the rate capability of the counter (see below). The figure shows some examples of pulse shape obtained by differentiation. At the limit for $R \to 0$, one speaks rather of a current signal than a voltage; this is given by

$$i(t) = \ell C \frac{dv(t)}{dt} = -\frac{QC}{4\pi\varepsilon_0} \frac{1}{t_0 + t} \quad .$$

The current is maximum for $t = 0$:

$$i_{max} = i(0) = -\frac{\mu^+ QC^2 V_0}{4\pi^2 \varepsilon_0^2 a^2 P} \quad .$$

Substituting the numerical values of the previous example, and assuming $Q = 10^6 e$, (where e is the electron charge) one gets $i_{max} \simeq 13$ μA, which is a typical value for the operation of multiwire proportional chambers.

5.3 Choice of the gas filling

Since avalanche multiplication occurs in all gases, virtually any gas or gas mixture can be used in a proportional counter. In most cases, however, the specific experimental requirements restrict the choice to several families of compounds; low working voltage, high gain operation, good proportionality, high rate capabilities, long lifetime, fast recovery, etc., are examples of sometimes conflicting requirements. In what follows, we will briefly outline the main properties of different gases in the behaviour of the proportional counter; a more detailed discussion can be found in the bibliography for this section (in particular in the book by Korff).

Comparison of Figs. 44 and 47 shows that avalanche multiplication occurs in noble gases at much lower fields than in complex molecules: this is a consequence of the many non-ionizing energy dissipation modes available in polyatomic molecules. Therefore, convenience of operation suggests the use of a noble gas as the main component; addition of other components, for the reasons to be discussed below, will of course slightly increase the threshold voltage. The choice within the family of noble gases is then dictated, at least for the detection of minimum ionizing particles, by a high specific ionization; with reference to Table 1, and disregarding for economic reasons the expensive xenon or krypton, the choice falls naturally on argon. An argon-operated counter, however, does not allow gains in excess of 10^3-10^4 without entering into a permanent discharge operation; this is for the following reasons. During the avalanche process, excited and ionized atoms are formed. The excited noble gases can return to the ground state only through a radiative process, and the minimum energy of the emitted photon (11.6 eV for argon) is well above the ionization potential of any metal constituting the cathode (7.7 eV for copper). Photoelectrons can therefore be extracted from the cathode, and initiate a new avalanche very soon after the primary.

Argon ions, on the other hand, migrate to the cathode and are there neutralized extracting an electron; the balance of energy is either radiated as a photon, or by secondary emission, i.e. extraction of another electron from the metal surface. Both processes

result in a delayed spurious avalanche: even for moderate gains, the probability of the processes discussed is high enough to induce a permanent régime of discharge.

Polyatomic molecules have a very different behaviour, especially when they contain more than four atoms. The large amount of non-radiative excited states (rotational and vibrational) allows the absorption of photons in a wide energy range: for methane, for example, absorption is very efficient in the range 7.9 to 14.5 eV, which covers the range of energy of photons emitted by argon. This is a common property of most organic compounds in the hydrocarbon and alcohol families, and of several inorganic compounds like freons, CO_2, BF_3 and others. The molecules dissipate the excess energy either by elastic collisions, or by dissociation into simpler radicals. The same behaviour is observed when a polyatomic ionized molecule neutralizes at the cathode: secondary emission is very unlikely. In the neutralization, radicals recombine either into simpler molecules (dissociation) or forming larger complexes (polymerization). Even small amounts of a polyatomic quencher added to a noble gas changes completely the operation of a counter, because of the lower ionization potential that results in a very efficient ion exchange (see Section 4.2). Good photon absorption and suppression of the secondary emission allows gains in excess of 10^6 to be obtained before discharge.

The quenching efficiency of a polyatomic gas increases with the number of atoms in the molecule; isobutane (C_4H_{10}) is very often used for high-gain stable operation. Secondary emission has been observed, although with low probability, for simpler molecules like carbon dioxide, which may therefore occasionally produce discharge.

Addition of small quantities of electronegative gases, like freons (CF_3Br in particular) or ethyl bromide (C_2H_5Br) allows one to obtain the highest possible gains before Geiger-Müller discharge, i.e. saturated operation (see Section 5.1). Apart from their additional photon-quenching capability, the electronegative gases capture free electrons forming negative ions that cannot induce avalanches (at least in the field values normally met in a proportional counter). If the mean free path for electron capture is shorter than the distance from anode to cathode, electrons liberated at the cathode by any of the described processes will have very little probability of reaching the anode, and gains around 10^7 can be safely obtained before discharge or breakdown. To preserve detection efficiency, however, only limited amounts of electronegative gases can be used. Unfortunately, the use of polyatomic organic gases can have a dramatic consequence on the lifetime of counters, when high fluxes of radiation are detected. To start with, the dissociation process, which is at the basis of the quenching action, quickly consumes the available molecules in a sealed counter. For a gain of 10^6 and assuming there are 100 ion pairs detected in each event, about 10^8 molecules are dissociated in each event. In a typical 10 cm^3 counter operated at atmospheric pressure in a 90-10 mixture of noble gas and quencher, there are about 10^{19} polyatomic molecules available and therefore a sealed counter is expected to change its operational characteristics substantially after about 10^{10} counts. As we will see later, multiwire proportional chambers are normally operated in an open flow of gas, essentially because the necessity for large surfaces of detection with thin gas windows does not allow efficient sealing, and therefore gas consumption is not a problem. However, we have seen that some products of molecular recombination are liquid or solid polymers. These products will deposit on cathodes and anodes, depending on their affinity, and substantially modify the operation of the counter after integral fluxes of radiation around 10^7-10^8 counts per

cm^2. The following process takes place (Malter effect)[32]. When a thin layer of insulator develops on the cathode, as a result of the deposit of polymers, positive ions created in further avalanches deposit on the outer side of the layer and only slowly leak through the insulator to be neutralized on the cathode. When the detected radiation flux grows above a threshold value (10^2 or 10^3 counts per second per cm^2) the production rate of the ions exceeds the leakage rate and very quickly a high density of charge develops across the thin layer. The dipole electric field can be so high as to extract electrons from the cathode and through the insulator: a régime of permanent discharge is therefore induced, even if the original source of radiation is removed. Temporary suppression of the counter voltage stops the discharge; the counter, however, remains damaged and an exposure to lower and lower radiation fluxes will start the process again. Only complete cleaning can regenerate a damaged counter.

Flows of 10^8 counts per cm^2 are very quickly met in high-energy beams having typical intensities of $10^6/sec$ cm^2. Use of non-polymerizing quenchers, like alcohols, aldehydes, and acetates, was soon recognized to strongly suppress the ageing effect; however, their low vapour pressure as compared with hydrocarbons does not allow one to obtain an efficient quenching against photoionization and secondary emission (for example, isopropylic alcohol has a vapour pressure, at 20°, of 30 Torr). A solution to the dilemma has been found by taking advantage of the ion exchange mechanism already mentioned several times. If a non-polymerizing agent is chosen having its ionization potential lower than those of the other constituents of the gas mixture, addition of even a small quantity of the new quencher will modify the nature of the ions neutralized at the cathode into a non-polymerizing species. Propylic alcohol $[C_3H_7OH]$ and methylal $[(OCH_3)_2CH_2]$ are often used, having ionization potentials of 10.1 and 10.0 eV, respectively. Integrated rates in excess of 10^{10} counts per cm^2 have been measured, without alteration of the counter properties[33].

Use of a single inorganic quenching gas, like carbon dioxide, would of course avoid the ageing effect; the quoted instability of operation at high gains of argon-carbon dioxide counters, however, limits their use. Incidentally, radiation damage of carbon dioxide counters has been reported, probably as a result of a small amount of polluting agents in the gas[34,35]. Use of gas mixtures of three or four components may appear to be a nuisance, but in practice the advantages of having a high gain, stable operation in a large multiwire proportional chamber complex widely counteract the mixing problems.

5.4 Space-charge gain limitation

The growth in the avalanche process of a positive ion sheath around the wire has as a consequence the local reduction of the electric field; the normal field is completely restored only when all ions have been neutralized at the cathode (i.e. after several hundred μsec). When the counter is operated in the proportional or semiproportional mode, the extension of the avalanche along the wire is very small, between 0.1 and 0.5 mm, and therefore the field modification is confined to a small region of the counter. In Geiger-Müller operation, on the other hand, the avalanches spread all along the wire and the field in the whole counter is distorted: for several hundred μsec no further detection is possible.

When a counter is operated in a proportional mode, the effect of a uniformly distributed flow of radiation is to reduce the average gain. Figures 53 and 54 show the
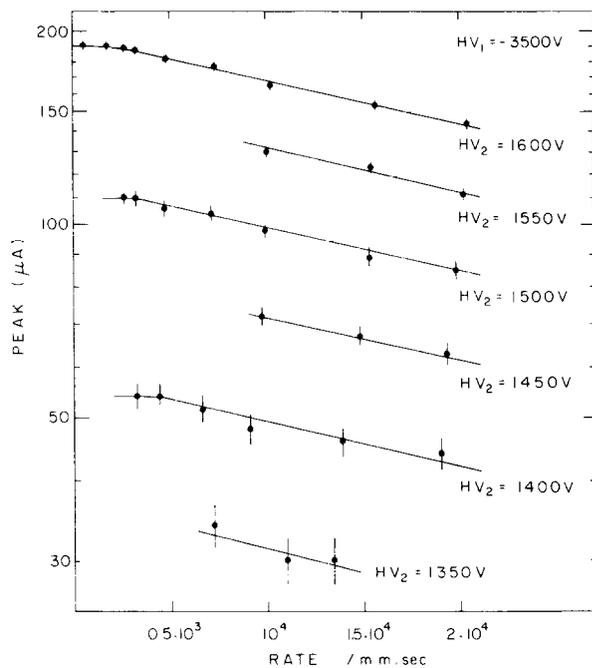
Fig. 53   Rate dependence of the peak current on
5.9 keV X-rays in a drift proportional
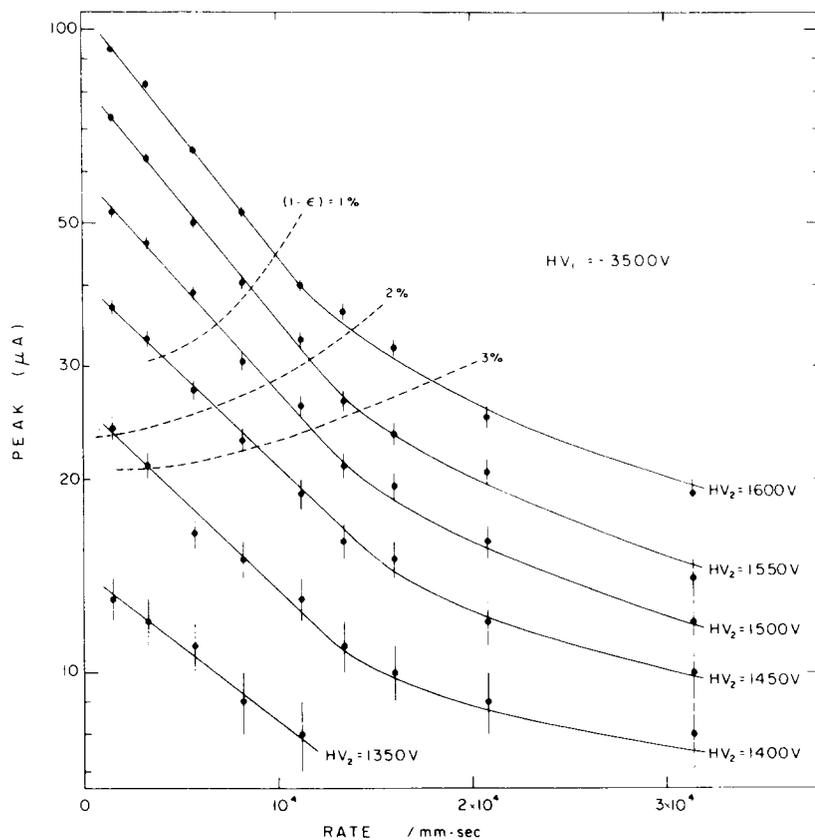chamber, for several anodic potentials[9]

Fig. 54   Rate dependence of the peak current for minimum ionizing
particles, in a drift chamber. The dashed curves show
the equal inefficiency intercept, for a fixed detection
threshold (5 μA) [9].

pulse-height reduction due to space charge, as measured in a drift chamber for ^{55}Fe 5.9 keV X-rays and for minimum ionizing particles[9]. The incident fluxes are given in counts per second per millimetre of anode wire; the corresponding surface rate can be obtained taking into account the counter geometry. Following the formulation of Hendricks[36], one can compute the approximate change in the anodic potential V_0 due to a flux R of ionizing events, each producing nMe charges in the avalanche,

$$\Delta V = \frac{nMeRT}{4\pi^2\varepsilon_0} = KMR \quad , \tag{37}$$

where T is the total drift time of positive ions, as given by Eq. (36). Introducing Eq. (37) into the dependence of the multiplication factor on the voltage, one can obtain the corresponding change in the gain. This could be done using expression (31); however, it appears that in the region of gain values we are normally concerned with (10^6 or more), the simpler expression for M given by formula (32) can be used; in this case $M_0 = K e^{CV_0}$ and $M = M_0 e^{-\Delta V}$. Substituting this in Eq. (37) one gets

$$\Delta V e^{\Delta V} = KM_0R \quad ,$$

which, for small variations of ΔV ($e^{\Delta V} \simeq 1$) gives $\Delta V = KM_0R$ and

$$M = M_0 e^{-KM_0R} \quad .$$

The exponential decrease in the multiplication factor with the rate is precisely what has been observed (see Figs. 53 and 54), at least for moderate rates. At higher rates, $e^{\Delta V} > 1$ and therefore $\Delta V < KM_0R$; then the decrease of the gain with rate is less than exponential as shown by the data. A practical consequence of a gain decreasing with the rate is, of course, loss of efficiency when operating at fixed detection thresholds, as is the case in multiwire proportional chambers. We will come back to this point in Section 6.

6. MULTIWIRE PROPORTIONAL CHAMBERS

6.1 Principles of operation

Proportional counters have been and are widely used whenever measurement of energy loss of radiation is required. The space localization capability of a counter is, however, limited to the determination that a particle has or has not traversed the counter's volume. Stacking of many independent counters is possible, but is not very attractive mechanically. There was a vague belief that multiwire structures in the same gas volume would not properly work, because the large capacitance existing between parallel non-screened wires would cause the signal to spread, by capacitive coupling, in all wires, therefore frustrating any localization attempt in the structure. It was the merit of Charpak and collaborators to recognize that the positive induced signals in all electrodes surrounding the anode interested by an avalanche largely compensate the negative signals produced by capacitive coupling; these authors operated in 1967-68 the first effective multiwire proportional chambers[1], which comprised a set of anode wires closely spaced, all at the same potential, each wire acting as an independent counter.

A multiwire proportional chamber consists essentially of a set of thin, parallel and equally spaced anode wires, symmetrically sandwiched between two cathode planes; Fig. 55 gives a schematic cross-section of the structure. For proper operation, the gap ℓ is normally three or four times larger than the wire spacing s. When a negative potential is applied to the cathodes, the anodes being grounded, an electric field develops as indicated by the equipotentials and field lines in Fig. 56 and in a magnified view around the anodes, in Fig. 57 [37]. Suppose now that charges are liberated in the gas volume by an ionizing event; as in a proportional counter, conditions are set such that electrons will drift along field lines until they approach the high field region, very close to the anode wires, where avalanche multiplication occurs; Fig. 58 [38] shows the variation of the electric field along a direction perpendicular to the wire plane, for a typical multiwire proportional chamber.
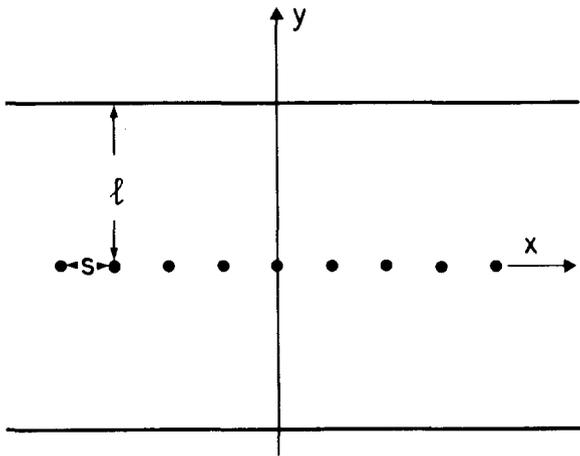
Fig. 55   Principle of construction and definition of parameters in a multiwire proportional chamber. A set of parallel anode wires is mounted symmetrically between two cathode planes (wires or foils).

Fig. 56   Electric field equipotentials and field lines in a multiwire proportional chamber. The effect on the field of a small displacement of one wire is also shown[37].

Fig. 57   Enlarged view of the field around the anode wires (wire spacing 2 mm, wire diameter 20 μm) [37]

Distance from centre of wire

Fig. 58   Variation of the electric field along the axis per-
pendicular to the wire plane and centred on one wire
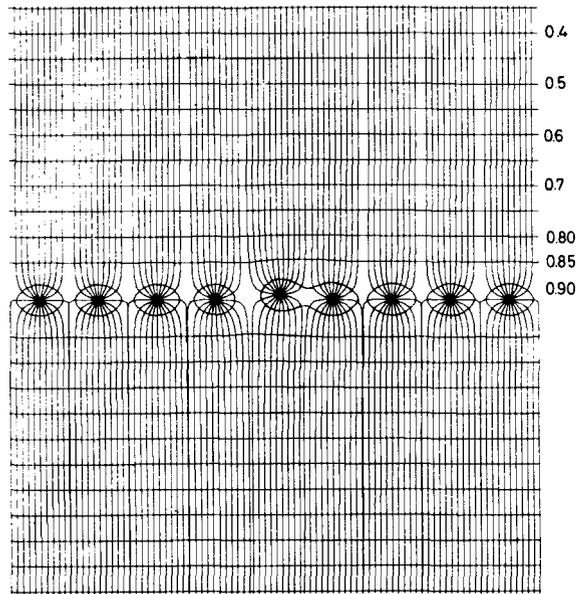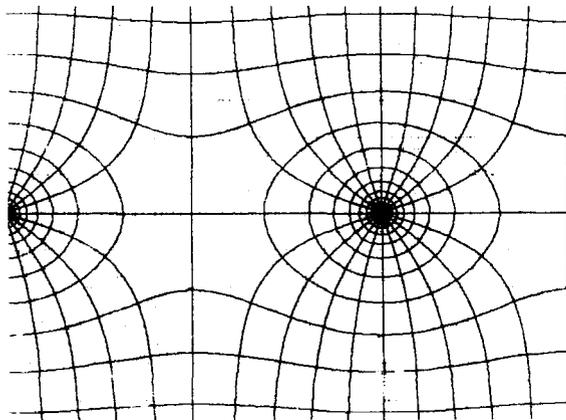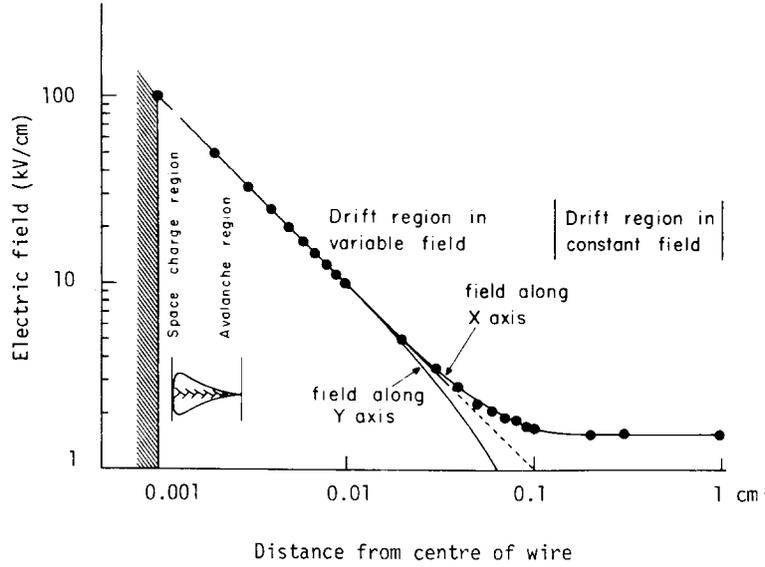in a multiwire proportional chamber (x), and along
the direction parallel to the wire plane (y) [38]

The analytic expression for the electric field can be obtained by standard electrostatic algorithms, and is given in many textbooks[39,40]. An approximated expression has been given by Erskine[37], who also computed the field deformations due to wire displacements.

With the definitions of Fig. 55 and requiring $V(a) = V_0$, $V(\ell) = 0$, one gets

$$V(x,y) = \frac{CV_0}{4\pi\varepsilon_0}\left\{\frac{2\pi\ell}{s} - \ln\left[4\left(\sin^2\frac{\pi x}{s} + \sinh^2\frac{\pi y}{s}\right)\right]\right\}$$

(38)

$$E(x,y) = \frac{CV_0}{2\varepsilon_0 s}\left(1 + \mathrm{tg}^2\frac{\pi x}{s}\,\mathrm{tgh}^2\frac{\pi y}{s}\right)^{\frac{1}{2}}\left(\mathrm{tg}^2\frac{\pi x}{s} + \mathrm{tgh}^2\frac{\pi y}{s}\right)^{-\frac{1}{2}}$$

and the capacitance per unit length is given by

$$C = \frac{2\pi\varepsilon_0}{(\pi\ell/s) - \ln(2\pi a/s)}\ ,$$

(39)

where a is the anode wire radius. Notice that, since $a \ll s$, the value given by Eq. (39) is always smaller than the capacity of the plane condenser with the same surface $(2\varepsilon_0 s/\ell)$. Computed values of C are given in Table 6 for several typical geometries; in general, one can see that the capacitance is quickly decreasing with the wire spacing, while it does not depend very much on the wire diameter. Along the symmetry lines $x = 0$ and $y = 0$, the electric field can be written as

$$E_y = E(0,y) = \frac{CV_0}{2\varepsilon_0 s}\coth\frac{\pi y}{s}$$

$$E_x = E(x,0) = \frac{CV_0}{2\varepsilon_0 s}\cot g\frac{\pi x}{s}\ .$$

Table 6

Capacitance per unit length, in pF/m, for several
proportional chambers' geometries

ℓ (mm)	2a (μm)	s (mm)			
		1	2	3	5
8	10	1.94	3.33	4.30	5.51
	20	2.00	3.47	4.55	5.92
	30	2.02	3.56	4.70	6.19
4	10	3.47	5.33	6.36	7.34
	20	3.63	5.71	6.91	8.10
	30	3.73	5.96	7.28	8.58

It is also instructive to consider the following approximations:

$$\text{for } y \ll s : \quad E(x,y) \simeq \frac{CV_0}{2\pi\epsilon_0} \frac{1}{r} \ , \quad r \simeq (x^2 + y^2)^{1/2} \ ; \tag{40}$$

$$\text{for } y \geq s : \quad \coth\frac{\pi y}{s} \simeq 1 \ , \quad E_y = \frac{CV_0}{2\epsilon_0 s} \ . \tag{41}$$

Equation (40) shows that the field is radial around the anode, with an expression identical
to that of a cylindrical proportional counter, Eq. (27). One can therefore use the main
results obtained in Sections 5.1 and 5.2 to discuss the operational characteristics of a
multiwire proportional chamber, provided that the correct value for the capacity per unit
length is used.

6.2 Choice of geometrical parameters

The accuracy of localization in a multiwire proportional chamber is obviously determined
by the anode wire spacing; spacings of less than 2 mm are, however, increasingly difficult
to operate. One can understand the reasons by inspection of the expressions (40) and (41)
and of the approximate multiplication factor, expression (32). For a fixed wire diameter,
to obtain a given gain one has to keep the charge per unit length CV_0 constant, i.e. increase
V_0 when s (and therefore C) is decreased. For example, going from 2 to 1 mm spacing V_0 has
to be almost doubled (see Table 6). At the same time, however, the electric field in the
drift region is also doubled; the chance that some drifting electrons meet the Raether con-
dition (26) is strongly increased. Practical experience has shown that, if 2 mm wire spacings
are possible, 1 mm wire spacings are rather hard to operate for surfaces larger than 100 cm^2
or so. Decreasing the wire diameters helps, but there are obvious mechanical and electro-
static limitations (see Section 6.4). Notice that scaling down all geometrical parameters
(i.e. the distance and diameter of the wires, and the gap) is not sufficient to preserve good
operation: in fact, the mean free path for ionization remains invariant, unless the gas pres-
sure is correspondingly increased. Work in this direction has been carried out to obtain good
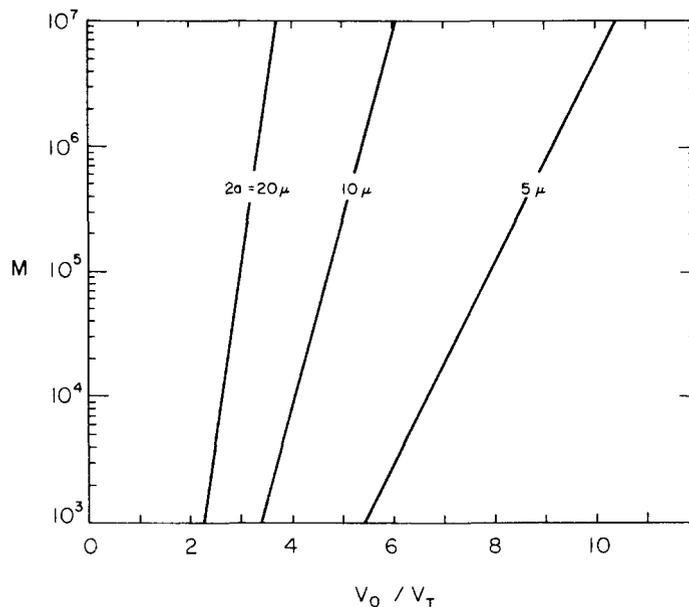accuracies over small surfaces[41].

Fig. 59 Dependence of the multiplication factor on
the operational voltage, relative to the thresh-
old voltage, in a 2 mm spacing multiwire propor-
tional chamber with several wire diameters
[computed from expression (31)].

Let us now investigate the influence of the wire diameter, on a given geometry. Figure 59
shows how the gain varies, as a function of the ratio V_0/V_T, for an s = 2 mm, ℓ = 8 mm chamber
with several anode radii; the approximate expression (31) has been used, with the correct
value for C as given by formula (39) for each geometry and for argon (k = 1.8 × 10^{-21} m^2 V^{-1}).
Clearly, although in principle any wire diameter allows one to obtain any gain, the steeper
slope obtained for large diameters means a much more critical operation. We can represent the
effect of all mechanical and electrical tolerances (see the next section) as a widening of
the lines drawn in the figure into narrow bands; for a given V_0/V_T, the multiplication factor
will vary, across the chamber, between two extremes. The steeper the slope of a given band,
the more likely it is that one section of a chamber will begin to discharge when another sec-
tion is not yet properly amplifying. Obviously, however, thick anode wires are easier to
handle than thin ones and a compromise has to be found; diameters around 10 μm are a prac-
tical limit, while that of 20 μm is more frequently used.

6.3 Dependence of the gain on mechanical tolerances

The gain of a chamber at a given operational voltage depends on the detailed shape and
value of the electric field in the multiplication region and can therefore change along a
wire or from wire to wire as a consequence of mechanical variations. The maximum tolerable
differences in gain depend, of course, on the specific application: in pulse-height mea-
suring devices, requirements are much more severe than in threshold-operated chambers.

A detailed analysis of the gain variations due to several kinds of mechanical tolerances
can be found in Erskine[37] and Dimčowski[42]. Here we would like to give only a qualitative

formulation, based on the approximated expression (32) for the multiplication factor. Let $Q = CV_0$ be the charge per unit length of the wires; differentiation of Eq. (32) gives

$$\frac{\Delta M}{M} = \ln M \frac{\Delta Q}{Q} .$$

(42)

The problem of gain variation is therefore reduced to the calculation of the change in the wires' charge.

Recalling the expression for the capacitance per unit length C in a proportional chamber, Eq. (39), we can compute the effect of a uniform change in the wire radius Δa and in the gap $\Delta \ell$

$$\frac{\Delta Q}{Q} = \frac{C}{2\pi\varepsilon_0} \frac{\Delta a}{a}$$

$$\frac{\Delta Q}{Q} = \frac{C\ell}{2\pi\varepsilon_0 s} \frac{\Delta \ell}{\ell} .$$

(43)

Consider, for example, a typical $\ell = 8$ mm, s = 2 mm chamber with 2a = 20 μm operating at a gain around 10^6. The gain variation will be

$$\frac{\Delta M}{M} \simeq 3 \frac{\Delta a}{a} \quad \text{and} \quad \frac{\Delta M}{M} \simeq 12 \frac{\Delta \ell}{\ell} .$$

Typical diameter variations around 1% have been measured on standard 20 μm wires, which result in a 3% change in gain, while a 0.1 mm difference in the gap length results in about 15% gain change.

The effect of a displacement of one wire in the wire plane is also a change in the charge, in the displaced wire as well as in its neighbours. Erskine[37] has computed the relative charge modification for a displacement of a wire (wire 0) both in the x and in the y directions (see Fig. 55 for the definition of the reference system). The results for a typical chamber geometry are shown in Figs. 60 a and b. It appears that a 0.1 mm displacement
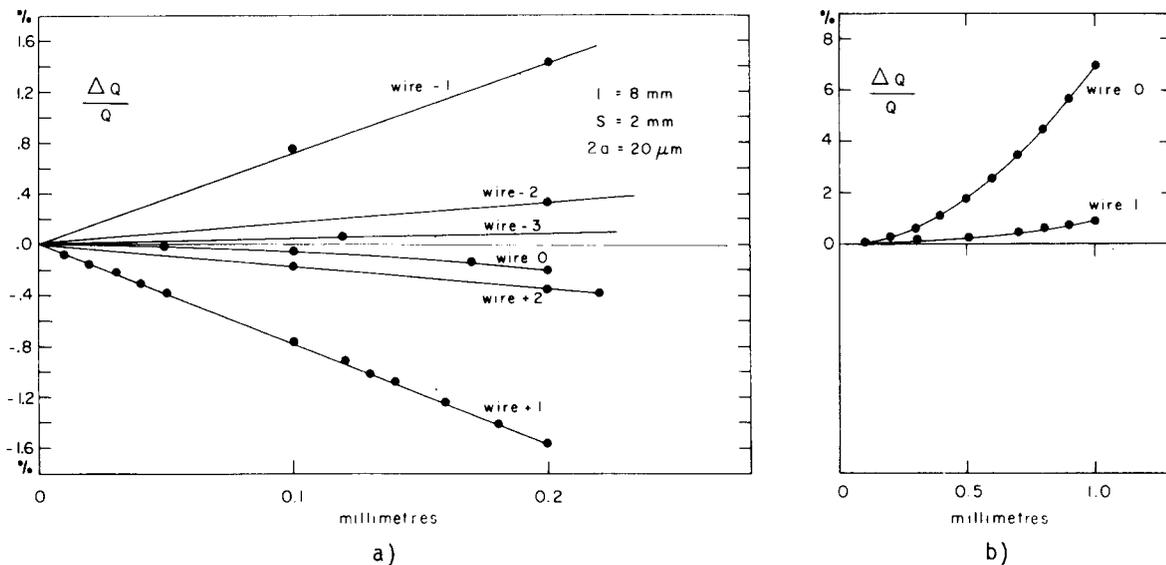

Fig. 60 Relative change in the charge per unit length due to wire displacements[37]. In (a), wire 0 is displaced in the x direction (see Fig. 55), in (b) in the y direction. The change in the charge of the neighbouring wires is also shown.

of a wire in the wire plane results in a 1% change in the charge of the two adjacent wires, and from Eq. (42) this means, at gains around 10^6, more than a 10% change! This is obviously the most critical parameter in chambers' construction, if a good energy resolution is required.

Expression (42) can also be used to estimate the variation of the multiplication factor with the operational voltage V_0; a 1% change in V_0 results in an increase of about 15% in M at gains around 10^6. Practical experience shows that, with normal mechanical tolerances and for medium-size chambers, an over-all gain variation around 30-40% can be expected, and this has to be taken into account when designing the detection electronics.

6.4 Electrostatic forces

In a structure like that of a multiwire proportional chamber, the anode wires are not in a stable equilibrium condition when a difference of potential is applied. In fact, assuming that one wire is slightly displaced from the middle plane, it will be attracted more to the side of the displacement and less to the other, and the movement would continue indefinitely if there was no restoring force (the mechanical tension on the wires). It has been observed in large size chambers (1 m or more) that, above a certain value of the operational voltage, the wires are unstable and the new equilibrium has all wires alternatively displaced up and down, as shown in Fig. 61. Following Trippe[43] we can compute the critical length of a chamber for wire stability. Assuming a radial field as given by Eq. (40), not modified by the small displacement δ, the force between two equal linear charges CV_0 at a distance r, per unit length, is

$$F(r) = \frac{(CV_0)^2}{2\pi\epsilon_0} \frac{1}{r} ,$$

and, from Fig. 61 and approximating the tangents to the arcs, the total force on a given wire, per unit length, in the direction normal to the wire plane, is

$$\sum F_\perp \simeq 2 \frac{(CV_0)^2}{2\pi\epsilon_0} \left\{ \frac{1}{s} \frac{2\delta}{s} + \frac{1}{3s} \frac{2\delta}{3s} + \dots \right\} = \frac{(CV_0)^2 \pi}{4\epsilon_0} \frac{\delta}{s^2} .$$
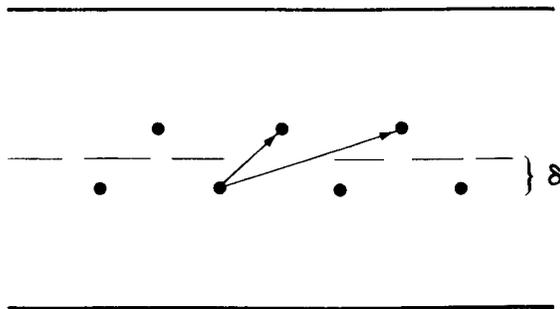

Fig. 61   Electrostatic instability in multi-wire proportional chambers. The wires are shown alternatively displaced by a quantity δ from the central plane.

If T is now the mechanical tension of the wire, the restoring force, in the direction perpendicular to the wire plane and per unit length, is

$$R = T \frac{d^2\delta}{dx^2} ,$$

where $\delta = \delta(x)$ is the displacement of the wire along its length, with the conditions $\delta(0) = \delta(L) = 0$ if L is the total wire length. For equilibrium, therefore, one must have $R = -\sum F_\perp$, or

$$T \frac{d^2\delta}{dx^2} = - \frac{(CV_0)^2 \pi}{4\varepsilon_0} \frac{\delta}{s^2} .$$

The equation has the solution

$$\delta(x) = \delta_0 \sin\left(\frac{CV_0}{2s} \sqrt{\frac{\pi}{\varepsilon_0 T}} x \right)$$

and the boundary condition $\delta(L) = 0$ means

$$\frac{CV_0}{2s} \sqrt{\frac{\pi}{\varepsilon_0 T}} L = \pi \quad \text{or} \quad T = \frac{1}{4\pi\varepsilon_0} \left(\frac{CV_0 L}{s} \right)^2 .$$

For tensions larger than this, no solution is possible other than $\delta(x) \equiv 0$, which means that the wires remain stable. The required stability condition is, therefore,

$$T \geq T_c = \frac{1}{4\pi\varepsilon_0} \left(\frac{CV_0 L}{s} \right)^2$$

or, for a given maximum tension T_M allowed by the elasticity module of a given wire, the critical stability length is

$$L_c = \frac{s}{CV_0} \sqrt{4\pi\varepsilon_0 T_M} . \tag{44}$$

Table 7 gives for tungsten wires of several diameters the maximum mechanical tension that can be applied before inelastic deformation. As an example, in an s = 2 mm, ℓ = 8 mm multiwire proportional chamber with 20 μm wires, the critical length is about 85 cm for an operational voltage V_0 = 5 kV (normal for this geometry, see Section 6.5). When larger sizes are necessary, some kind of mechanical support has to be foreseen for the wires, at intervals shorter than L_c [44,45]. Using thinner wires, if on the one hand one gains in performance as shown above, on the other hand one needs much more closely spaced supports and this is a severe mechanical complication and a source of localized inefficiencies.

Table 7

Maximum mechanical tension (in newtons) for tungsten wires, as a function of their diameter

2a (μm)	T_M (N)
5	0.04
10	0.16
20	0.65
30	1.45

Another consequence of electrostatic forces in a multiwire chamber is the over-all attraction of the outer electrodes towards the anode plane, and therefore an inflection of the cathode planes with a reduction of the gap width in the centre of a large chamber. As

we have seen in the previous section, the multiplication factor is very sensitive to the gap width and this can be a problem in large size chambers. Taking into account all charge distributions in the multiwire chamber structure, one can compute the over-all electrostatic force per unit surface, or pressure, on each cathode[46]; the calculation is, however, rather tedious. We can reach essentially the same result using the approximated expression (41) for the field in the drift volume. The field at the surface of the cathode conductors is then

$$E_S = \frac{E_y}{2} = \frac{CV_0}{4\varepsilon_0 s} .$$
(45)

Simple charge balance shows that the average charge per unit surface on each cathode is $CV_0/2\,s$ [this can also be deduced from expression (41) if one remembers the basic electrostatic relationship $E = \sigma/\varepsilon_0$]. The electrostatic pressure on each cathode is, therefore,

$$p = \frac{C^2 V_0^2}{8\varepsilon_0 s^2} .$$
(46)

The limits of validity of this expression can be found in the requirement that the field (and therefore the charge distribution) on the surface of the cathodes is constant; from Fig. 56, one can see that this assumption is essentially true for chambers having $\ell \gg s$.

The maximum inwards deflection of a square foil of surface H^2, stretched with a linear tension T, and subject to a pressure p, is given by

$$\Delta y = \frac{p}{T} \frac{H^2}{8} .$$
(47)

Combining Eqs. (46) and (47), one cane deduce the maximum deflection for a given chamber geometry, or the maximum size for a chamber if a limit is set for the deflection. In case of large surfaces, a mechanical gap-restoring spacer may be necessary.

As an example, let us compute the maximum gap reduction in an s = 2 mm, 8 mm gap chamber with H = 3 m operating at 4.5 kV; from Table 6 one obtains

$$Q = CV_0 = 1.5 \times 10^{-8} \text{ C/m}$$

and, from Eq. (46), p = 0.8 N/m². The yield strength of aluminium alloys is around 2×10^8 N/m², and for a 20 μm thick foil this gives a maximum stretching tension T of 4×10^3 N/m. Introducing this value in Eq. (47), one can see that the maximum deflection is about 220 μm, which implies a gain increase in the centre of the chamber of about 35% at gains around 10^6 (see Section 6.3), in general not tolerable for correct operation. A mechanical gap-restoring device or spacer is necessary; several kind of spacers have been developed[47,48] but they are, of course, a source of inefficiency.

6.5 General operational characteristics: proportional and semi-proportional

A large variety of gases and gas mixtures is currently used in multiwire proportional chambers. Except for special applications (for example, high densities or very good proportionality) all mixtures are more or less equivalent, in terms of performances, at least for moderate gains. Exceptionally large gains are, however, possible only in several specific mixtures containing an electronegative controlled impurity.

A general discussion on gases for proportional counters was given in Section 5.3; here we will present only a collection of experimental observations. A stable proportional or semi-proportional operation can be achieved in mixtures of argon or xenon with carbon dioxide, methane, isobutane, ethylene, ethane, etc; gains above 10^5 can be obtained before breakdown. For a typical energy loss of 6 keV this implies (see Table 1) a charge signal around 3 pC, or 300 mV on a 10 pF load. A collection of measured average pulse heights on ^{55}Fe X-rays on a very large impedance (100 kΩ) is shown in Figs. 62 and 63 [49], for mixtures of argon-
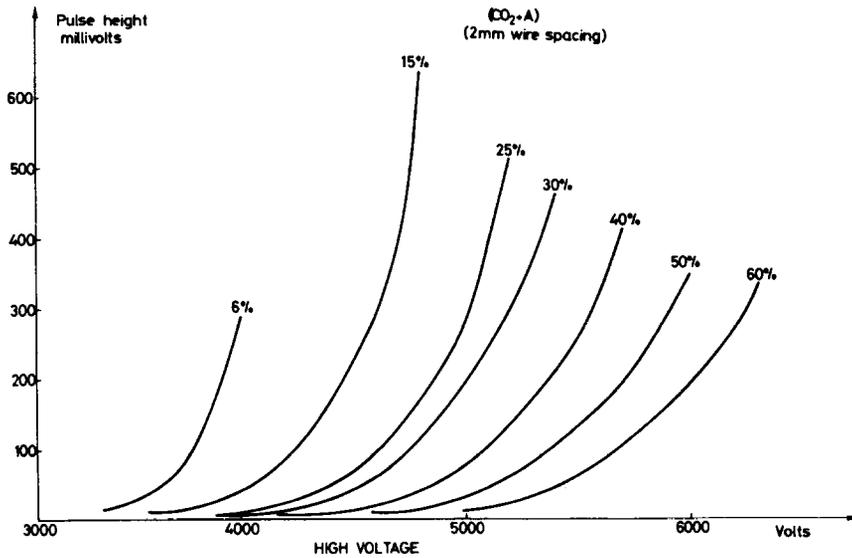

Fig. 62 Peak pulse height on ^{55}Fe 5.9 keV X-rays, in a 2 mm wire spacing chamber for several argon-carbon dioxide mixtures (on 100 kΩ)[49].
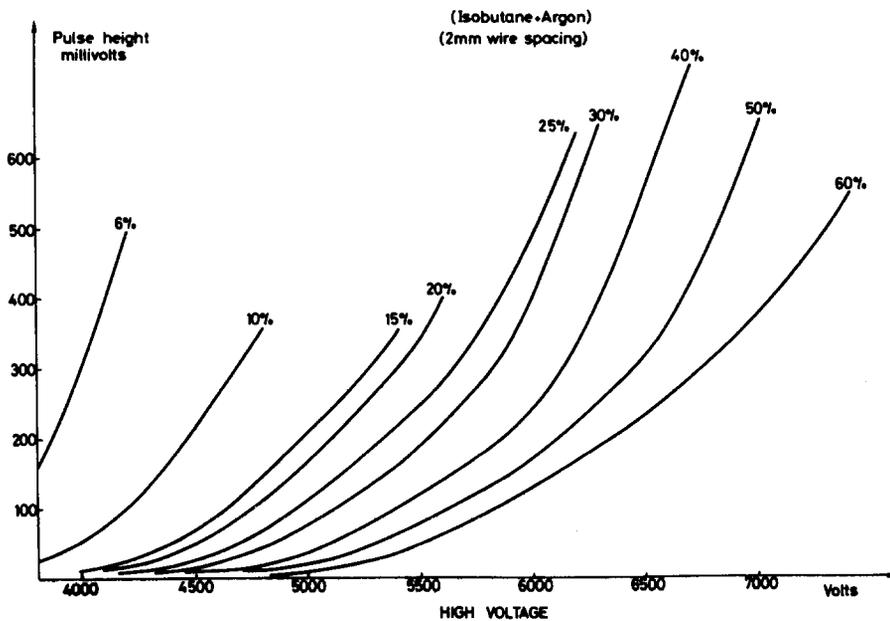

Fig. 63 Peak pulse height on ^{55}Fe in a 2 mm wire spacing chamber for several argon-isobutane mixtures (on 100 kΩ)[49].

a)   b)
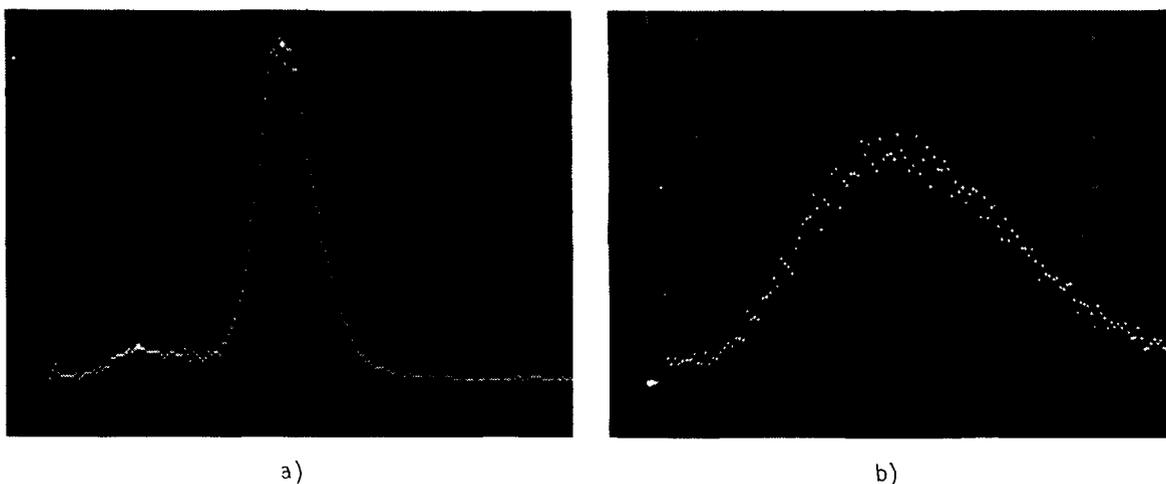
Fig. 64   Pulse-height distribution in the proportional region for ^{55}Fe 5.9 keV X-rays (a)
and for minimum ionizing particles (b) in a standard ℓ = 8 mm, s = 2 mm wire chamber.
The horizontal scale corresponds to about 1 mV/div. (on 1 kΩ).

carbon dioxide and argon-isobutane, respectively.   In Fig. 64 the actual pulse-height distri-
butions are shown as measured under identical conditions for 5.9 keV X-rays (Fig. 64a) and
for minimum ionizing particles (Fig. 64b) in a 2 × 8 mm gap chamber, operating with a 60-40
argon-isobutane mixture.   As from the considerations of Section 2 and from Table 1, in the
quoted geometry the average energy loss of minimum ionizing particles is also around 6 keV,
the characteristic Landau distribution of pulse height is, however, observed.   In both cases,
the horizontal scale is about 1 μA/div., or 1 mV/div. on a 1 kΩ load. Full efficiency of detec-
tion for minimum ionizing particles can be obtained with an electronic threshold around one
tenth of the peak amplitude, i.e. about 0.5 mV on 1 kΩ;   this is a typically adopted value
for operation in the porportional region.   Notice also in Fig. 64a the characteristic 3.2 keV
escape peak of argon.

Figure 65 shows the approximate limits of operation of a standard 8 mm gap, 2 mm spacing
chamber for argon-isobutane and argon-carbon dioxide mixtures;   the beginning of the plateau
is, of course, determined by the detection electronics' threshold, 0.5 mV in this case.
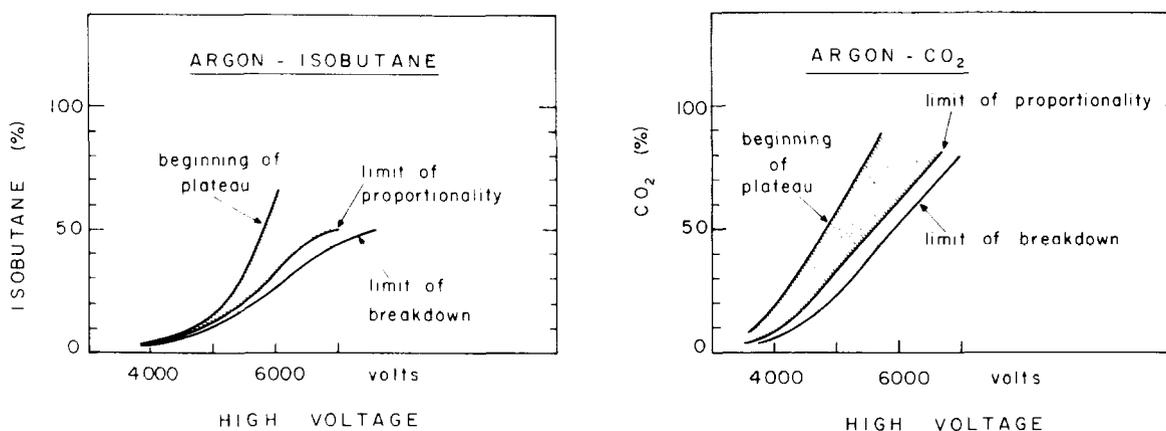

Fig. 65   Approximate limits of operation of an 8 mm gap, 2 mm wire spacing chamber, as a
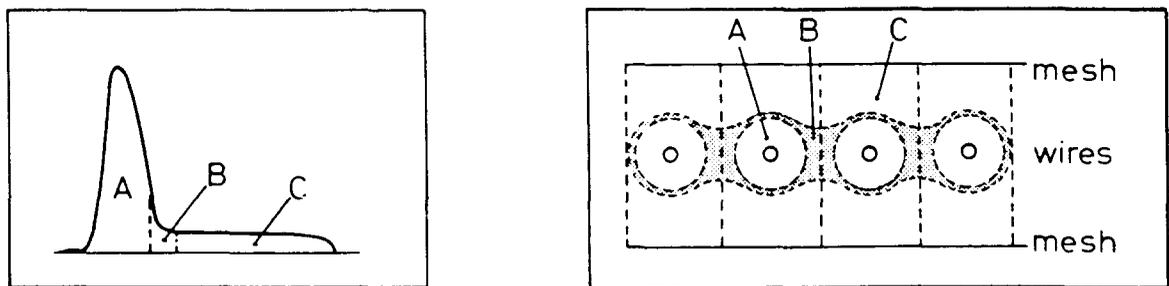function of isobutane and carbon dioxide content in argon[49].

Fig. 66   Timing properties of a multiwire proportional chamber[38]. Depending on where the
           original charge has been deposited, one can distinguish a "fast" region A, a "drift"
           region C, and an intermediate region B contributing to the tail in the fast region
           time distribution.

The timing properties of a proportional chamber are determined by the collection time of
the electrons produced by the ionizing track; the peculiar structure of the electric field
around the wires allows the separation of three regions, indicated as A, B, and C in Fig. 66.
Electrons produced in region A are quickly collected (typical drift velocities in this region
of high fields are above 5 cm/μsec); tracks crossing the low field region B, however, will
produce a characteristic tail in the time distribution. Electrons produced in region C, on
the other hand, smoothly drift to the anode where they are amplified and collected. The time
resolution of a chamber is defined as the minimum gate width necessary on the detection elec-
tronics for full efficiency; it is of around 30 nsec for a 2 mm spacing chamber. Figure 67
shows the typical time distribution observed in such a chamber, when all wires are connected
together (meaning that each track crosses region A or B of at least one wire), while Fig. 68
shows the same spectrum for a single wire and an inclined beam: the long uniform tail in this
case corresponds to tracks crossing region C of the considered wire. When detecting tracks
not perpendicular to the chamber, the number of wires hit on each track (or cluster size) will
obviously depend on the time gate on the associated electronics. If the gate length is the

|—————|
10 nsec
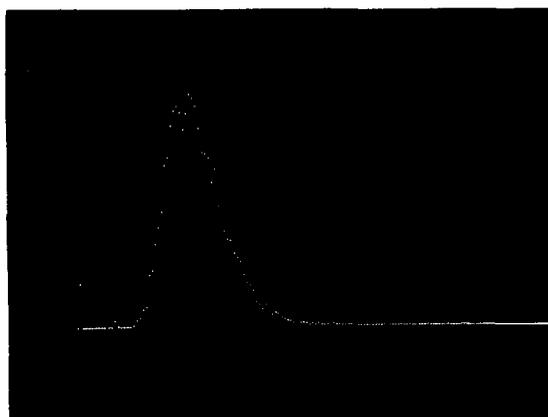
|———————————|
100 nsec

Fig. 67   Typical time distribution measure-
           ment in a chamber when all wires
           are connected together (total OR)
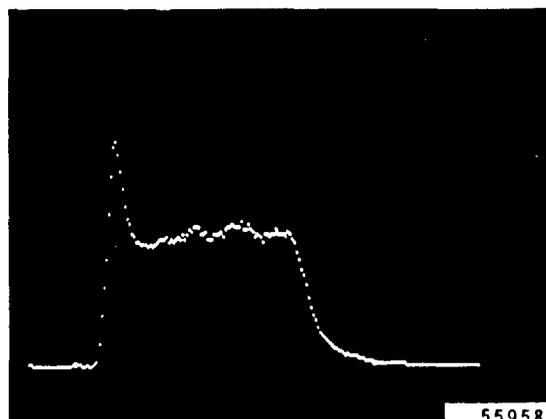
Fig. 68   Typical time distribution measured
           on a single wire for an inclined
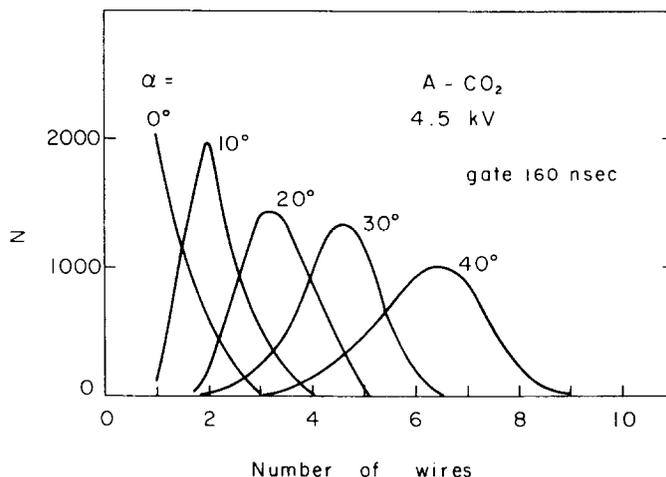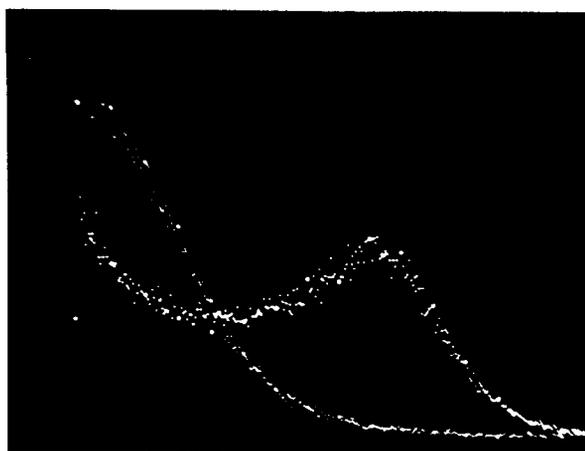   beam of minimum ionizing electrons.

Fig. 69   Average cluster size as a function of the
incidence angle ($0°$ means a track perpendi-
cular to the wire planes) for a large time
gate width[49])

minimum allowed by the requirement of full efficiency (around 30 nsec), the cluster size
will be of one or two wires in a ratio depending on the angle; if, one the other hand, the
gate length corresponds to the maximum drift time from region C (about 200 nsec for an 8 mm
gap), the cluster size will correspond to the maximum allowed by geometry. Figure 69 shows
the measured average cluster size as a function of the angle of incidence of the tracks ($\alpha = 0°$
means tracks perpendicular to the wires plane) for a large gate width. A detailed discussion
on cluster size and efficiency can be found in Fischer et al.[50]).

6.6 Saturated amplification region

Addition to a proportional gas mixture of small quantities of electronegative vapours,
like freon (CF_3Br) or ethylbromide (C_2H_5Br) allows the multiplication factor to be pushed to
values as high as 10^7 before breakdown, at the same time obtaining a saturated gain con-
dition, i.e. a pulse-height distribution which is entirely independent of the amount of charge
lost in the ionizing event. This particular behaviour was first noticed by Charpak and col-
laborators[49]) in the so-called "magic gas", argon-isobutane-freon in the volume proportions
70-29.6-0.4. The appearance of saturation in these conditions is illustrated by Fig. 70,
where the pulse-height spectra for minimum ionizing electrons and 5.9 keV photoelectrons are
compared at increasingly high operational voltages. In Fig. 70a, the amplification is still
proportional (the lower peak corresponds to fast electrons), in Fig. 70b saturation appears
and it is full in Fig. 70c. It has been proved that, under these conditions, one single
photoelectron provides the full pulse height[51]). Notice that the horizontal scales in the
three pictures are not the smae, owing to the large increase in the multiplication factor.
In Fig. 70c, the peak pulse height corresponds to about 50 μA, or 50 mV on 1 kΩ; thresholds
of detection around 5-10 μA are sufficient for full efficiency. Notice also, comparing
Figs. 70c and 64b, the reduced dynamic range of saturated pulses: this is greatly reducing
the overload recovery time problems of the electronics.

a)   HV = 4100 V

b)   HV = 4300 V
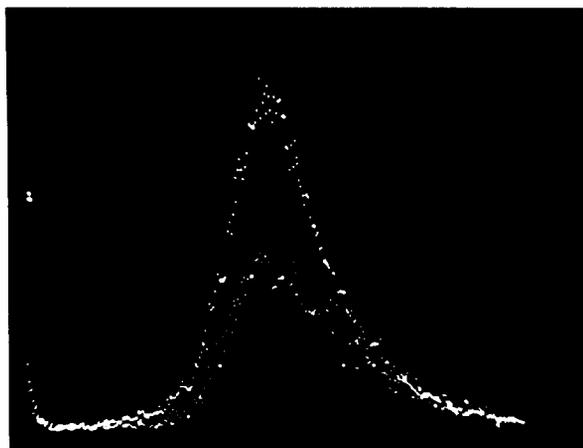
c)   HV = 4500 V

Fig. 70   Pulse-height spectra measured in a 5 mm gap, 2 mm
wire spacing multiwire chamber for ^{55}Fe X-rays and
minimum ionizing electrons at increasing anodic volt-
ages, in "magic" gas, showing the pulse-height satura-
tion effect[38]. Notice that the horizontal scales in
the three pictures do not coincide (the average pulse
height is increasing by more than one order of magni-
tude from (a) to (c).
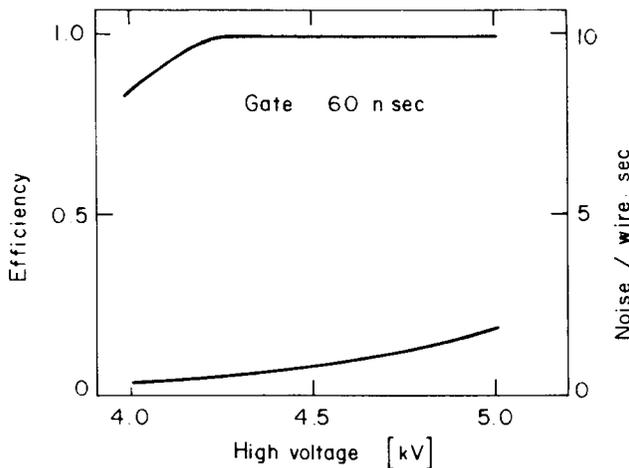
Fig. 71   Typical efficiency plateau and noise rate
           versus high voltage for an 8 mm gap, 2 mm
           wire spacing chamber, operating with magic
           gas and 5 mV (on 1 kΩ) detection thresholds[45]

Figure 71 shows a typical efficiency plateau for minimum ionizing particles, of a multi-wire proportional chamber operated with magic gas; the average wire noise rate, i.e. the counting rate in the absence of radiation, is also indicated.

The amount of electronegative gas that can be used in a chamber is obviously limited by the requirement of full efficiency; roughly speaking, the mean free path for electron capture λ_c should not be smaller than half the wire spacing. Figure 72 shows the measured efficiency for a 2 mm wire spacing chamber, at increasingly high concentrations of freon; under reasonable assumptions on the detection and capture mechanisms, the experimental points are well approximated by a calculation that assumes $\lambda_c^{-1} = 1.5$ p mm^{-1}, where p is the percentage of freon.
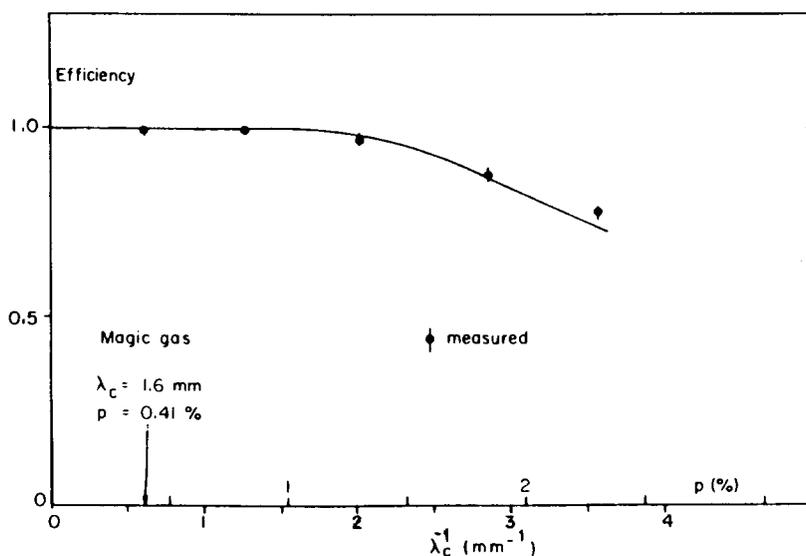

Fig. 72   Average efficiency for minimum ionizing particles, as
           a function of freon content in a 2 mm wire spacing
           chamber[51]

An important consequence of the presence of an electronegative gas in the mixture is a different behaviour in the cluster size versus gate length; electrons produced in the drift region (region C of Fig. 66) have a very small probability of reaching the anodes, and the cluster size is limited even for long gates, as illustrated in Fig. 73.
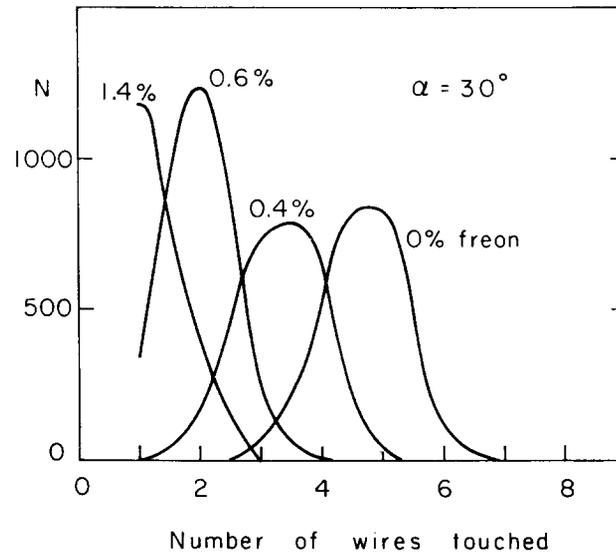
Fig. 73   Cluster size for 30° tracks, for a
large time gate, as a function of
freon content[49]. Reduction of the
sensitive zone around the wires re-
sults in a reduced cluster size.

6.7 Limited Geiger and full Geiger operation

A peculiar mode of operation has been observed in proportional chambers having thick wires widely spaced[52]. At sufficiently high voltages, and using a reduced concentration of organic quenchers (for example a 90-10 argon-isobutane mixture), a transition is observed from the normal proportional régime to a damped Geiger propagation, limited in spatial ex- tension to 10 mm or so along the wire. Although very attractive because of the remarkable signal pulse height that can be obtained (30-40 mV on 50 Ω, see Fig. 74), this mode of opera- tion has a severe rate limitation in the long time it takes the positive ion sheath to clear the activated anode wire section. For an 8 mm gap chamber, the assumption that after each count a 10 mm long section of the wire is dead for about 300 μsec provides a good agreement with the experimentally measured efficiency.

Full Geiger propagation has been observed in multiwire proportional chambers when only a small percentage of quencher, like methylal or ethyl bromide, is added to pure argon: again, very long dead-times are obtained. On the other hand, a measurement of the propaga- tion time of the Geiger streamer along the wires can be used to provide two-dimensional images of the conversion points[53].
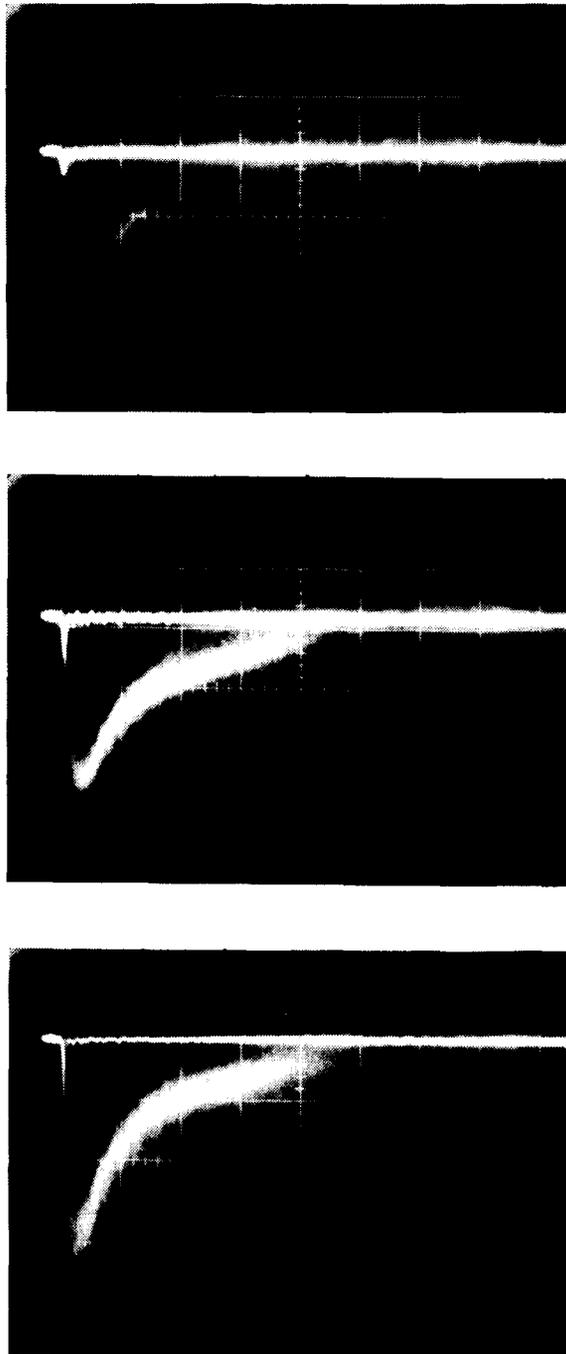
Fig. 74   Transition between the proportional and the limited
           Geiger operation in a multiwire chamber as seen di-
           rectly on a 50 Ω termination[52]. Horizontal and ver-
           tical scales are, respectively, 200 nsec/div. and
           10 mV/div. In (a) the small peak at the left shows
           the detection of 5.9 keV X-rays still in the propor-
           tional (or semiproportional) region, while limited
           Geiger pulses begin to appear; Figs. 74b and c, ob-
           tained at increasingly high voltages, show that all
           detected pulses enter the limited Geiger mode. The
           time extension of the signal (less than a μsec) proves
           the limited extension of the Geiger streamer (around
           1 cm).

6.8 Rate effects and ageing

We have already discussed in Section 5.4 the effect on the gain of a positive space charge built up at high rates. Since the gain reduction is a localized effect, extending perhaps one or two gap lengths around the hot spot in a chamber, substantial modification in the distributions of measured particles can be produced if the rate limit is locally exceeded. Measurements of the average pulse-height reduction as a function of rate were given in Figs. 53 and 54 for a specific geometry and gas mixture; of course, the effect depends on the gap and ion mobility, which however cannot vary over a very wide range. Inspection of the figures shows clearly that, at fixed threshold of detection, one will start losing efficiency when the lower part of the pulse-height spectrum distribution decreases below threshold. High chamber gains and low thresholds are therefore recommended for higher rate full efficiency operation. It appears in practice, however, that at any given chamber gain the threshold value cannot safely be reduced below one tenth or one twentieth of the average pulse height (essentially because of noise due to micro-discharges), and therefore almost identical efficiencies of detection versus rate have been measured in a large variety of gases and conditions. We will quote here a measurement realized in a multiwire proportional chamber having 1 mm wire spacing, and operating in magic gas [Fig. 75 [54]], and a similar measurement obtained in a drift chamber having 50 mm wire spacing and operating in argon-isobutane [Fig. 76 [9]]. The efficiency loss per unit length of the anode wire at high rates is about the same; obviously, the different surface acceptance in the two cases (50 to 1) reduces correspondingly the tolerable surface rate. Small wire spacings are therefore necessary for operation at high rates, although the spatial extension of the positive charges may create some degree of interdependence between wires.
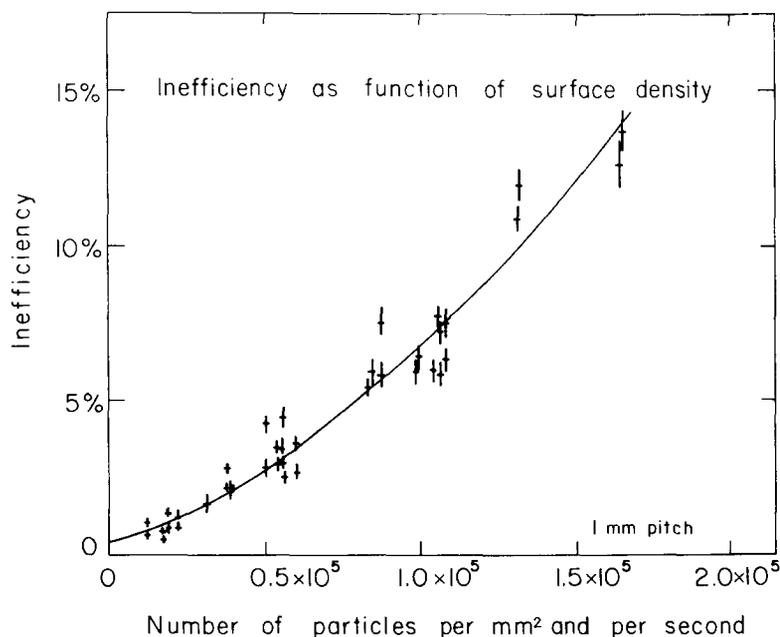

Fig. 75   Space-charge effect on chamber efficiency. Measured inefficiency on a $s = 1$ mm chamber, operating in magic gas, as a function of beam intensity[54].
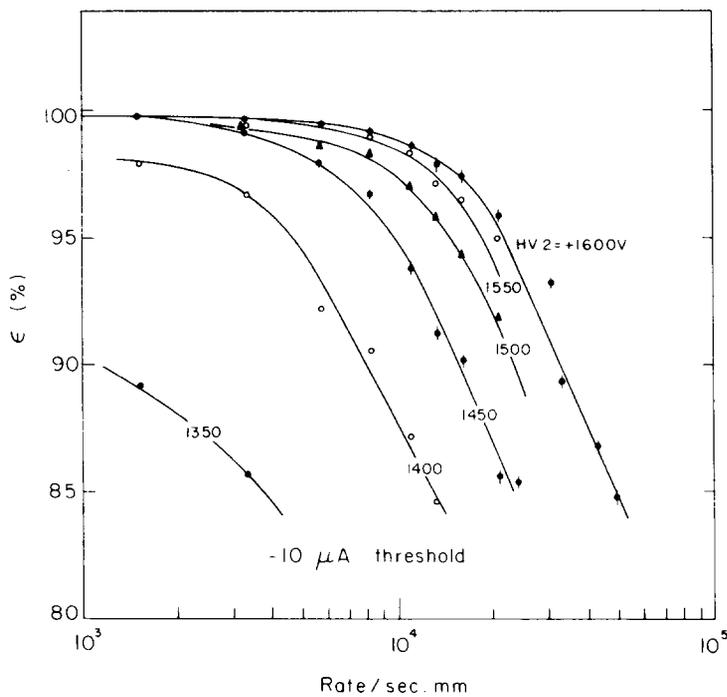
Fig. 76   Space-charge effect measured in a drift
chamber[9]. To present the results in a
plot independent from the wire spacing,
the horizontal scale has been given as
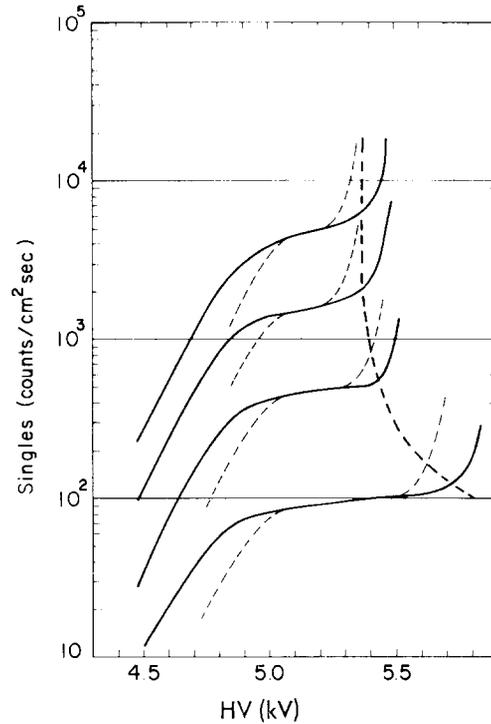rate per unit length of the anodic wire.

Fig. 77   Ageing effect in a chamber
operating with organic gas
mixtures (argon-isobutane
70-30)[33]. The singles count-
ing rate has been measured in
a chamber for increasing in-
tensities of [55]Fe X-rays, as
a function of high voltage,
before and after an irradia-
tion of about 10^7 counts/cm^2.
After the irradiation, the
average pulse height is re-
duced, for a given voltage,
and the discharge knee appears
at lower voltages.

Another effect related to high counting rates is the polymerization of some quenchers
or impurities with the appearance of secondary discharge (see also Section 5.3). A multiwire
chamber -- in which, either owing to improper cleaning or to the deposit of polymers due to
long exposures to radiation, the secondary discharge mechanism is active -- has a very charac-
teristic behaviour. Normally operating at low counting rates, it manifests an increasing and
sustained background rate (or dark current) when exposed to higher radiation fluxes even for
a short time, in the damaged regions. Rapid switch off and on of the operational voltage,
however, restores the original low-noise condition by capacitive removal of the positive ion
sheath on the insulating layers, which is responsible for the secondary sustained discharge.
The appearance of radiation damage can be quantitatively measured monitoring the singles
counting rates on a variable intensity radioactive source, as a function of the voltage.
Figure 77 shows such a measurement using a [55]Fe X-ray source before and after a long irra-
diation (around 10^7 counts/cm^2) [33]. The background rate is clearly increased, and appears
at lower and lower voltages for increasing rates of the source. A shift to higher voltages

of the lower edge of the plateau also appears, either due to the field reduction induced by the charge dipole created on the cathodes over the thin insulator film, or to an increase on the anode wire diameter due to conductive deposits (a thin carbonaceous deposit is normally found covering the anodes of a damaged chamber).

Use of non-polymerizing additives having an ionization potential lower than any other constituent in the gas mixture eliminates, or at least displaces by several orders of magnitude, the integral flux capability of a proportional chamber. In Fig. 78 [33] the efficiency plateau on minimum ionizing particles, the background rate, and the singles rate on ^{55}Fe are measured in a chamber operating with magic gas and methylal (72% argon, 23.5% isobutane, 0.5% freon and 4% methylal) before and after a total irradiation of 3.3×10^{10} counts/cm^2. No change is observed in the main operational parameters. Total exposures exceeding 10^{12}/cm^2 have been reported, without detectable ageing effects.
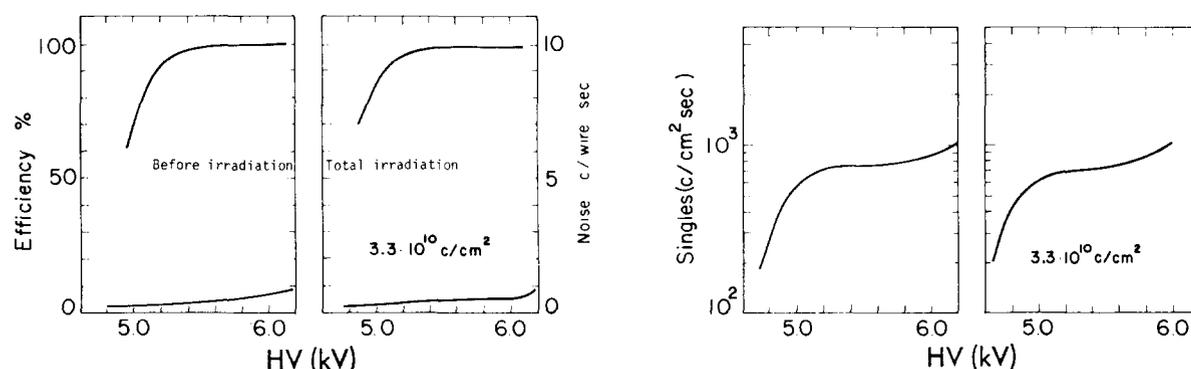

Fig. 78   Effect of a long irradiation in a chamber operating with 4% methylal added to magic gas[33]. At left, the effect on efficiency for minimum ionizing particles, and on the noise, and at right the effect on ^{55}Fe singles rate.

6.9 Mechanics and electronics

Just for completeness, I shall give here some hints on the mechanical construction of a multiwire chamber, as well as a basic description of the attached electronics; the reader should, however, refer to the quoted literature to obtain more details.

The basic problem of chamber construction is to support, on suitable frames, a succession of foils or wire planes constituting the electrodes, within a given set of mechanical and electrical tolerances, and to make the whole structure gas tight. Several methods of construction have been developed; we shall mention here two representative examples. The first, and more frequently used, consists in fabricating a set of self-supporting insulating frames, normally of extruded or machined fibre-glass, one per electrode. The wire electrodes are in general soldered on printed circuits, which are an integral part of the frames; the chamber is then mounted either gluing together the required number of frames (in case of small chambers) or assembled with pins and screws traversing the frames, the gas tightness being guaranteed by suitable rubber O-rings embedded in the frames, and by two thin gas windows (mylar or equivalent) on the two outer surfaces. Figure 79 shows an assembled three-gap chamber of this kind[45] and Fig. 80 [55] an exploded view of a similar chamber; the complexity and the large number of parts required is apparent. The reader will find elsewhere[44,45,55-61], a selection of papers devoted to a detailed description of this method of construction.
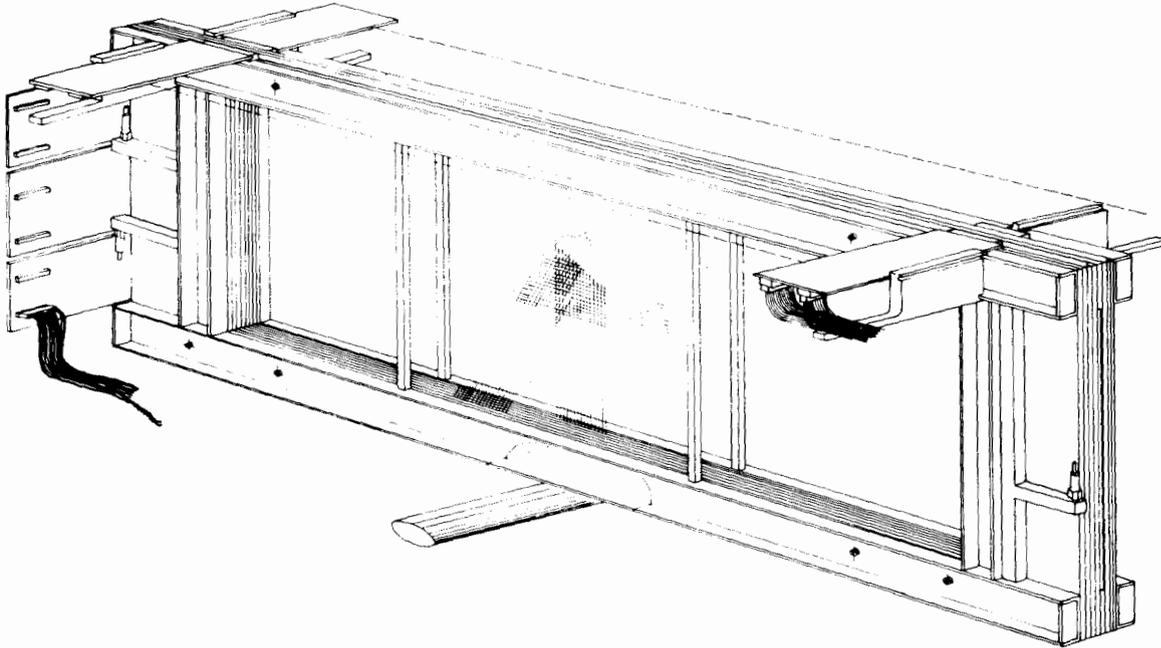
Fig. 79   Schematic view of an assembled three-coordinate medium-size multiwire proportional chamber[45].

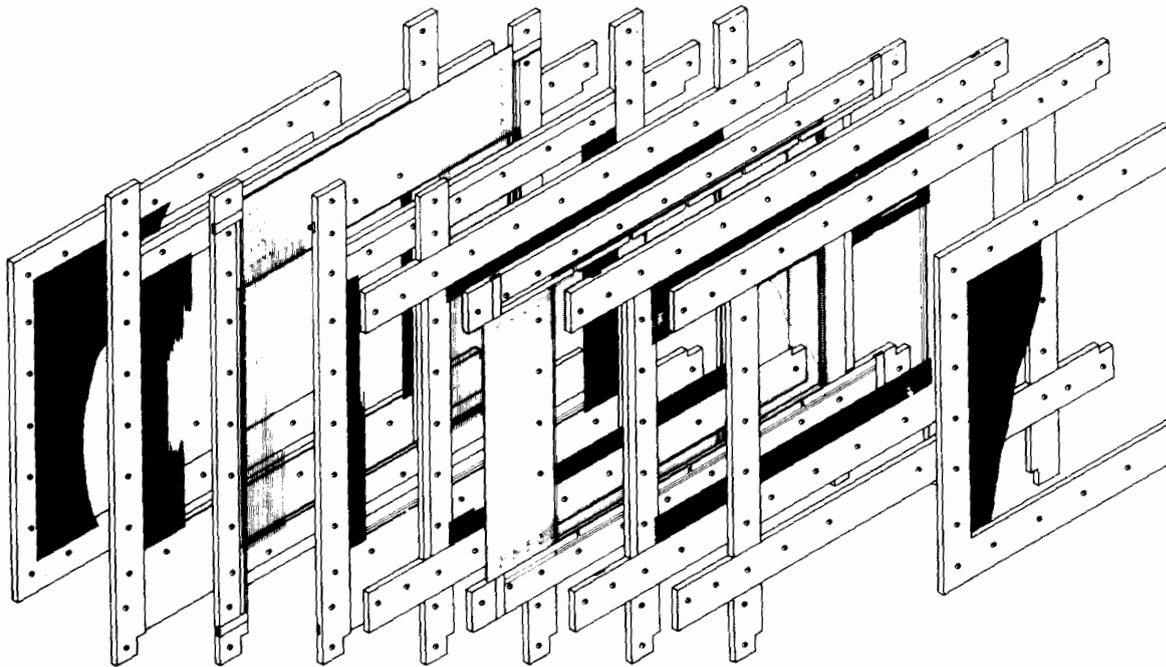Fig. 80   Exploded view of a 2-coordinates multiwire chamber, showing the number and the complexity of the required parts[55].

A drawback of the described technique lies in the rather unfavourable ratio between the active and the total surface (for a 1 m² chamber it is typically around 70%). In case the total available detection area is limited, as in a spectrometer magnet, the loss is considerable. For this reason, a different construction principle has been developed, based on the use of metallized self-supporting honeycomb or expanded polyurethane planes that constitute both the cathode plane and the chamber support[47]. A sketch of such self-supporting chambers is shown in Fig. 81 for a two-gap element; notice the very thin (1 cm or less) passive frame on the edges, on which the anode wires are stretched and soldered and the particular shape of one side, intended to contain the vacuum tubes at the CERN Intersecting Storage Rings. The perspective cut shows also the fishbone structure of the cathode plane strips, used to obtain an ambiguity-resolving third coordinate. The obvious advantages of large active area and ease of construction are, on the other hand, counterbalanced by a rather substantial increase in the chamber thickness in the active area (0.6 g/cm² against a few mg/cm² for a conventional construction).

cables + preampli for vertical wires ①

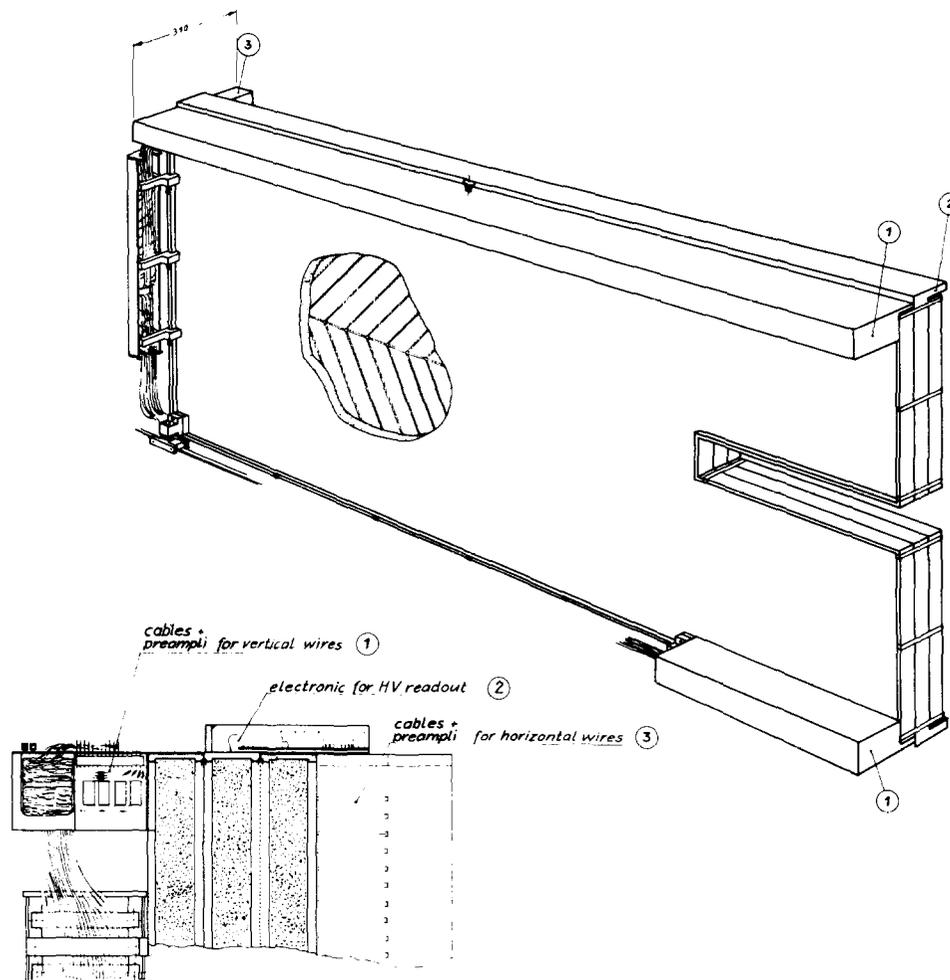electronic for HV readout ②

cables + preampli for horizontal wires ③

Fig. 81   Principle of construction of a self-supporting multiwire proportional chamber[47]. The basic building elements are foam or honeycomb plates, coated with insulating or conducting thin sheets as shown in the cross-section.

As already mentioned in Section 6.4, when the size of a chamber exceeds a square metre or so, electrostatic wire instabilities and over-all electrode deflections appear, which spoil the chamber's operation unless suitable mechanical support lines are used to balance the electrostatic forces. Supports must obviously be insulators if they are in contact with the anodes and, because they have a dielectric rigidity very different from that of a gas, a substantial field modification is produced that spoils the efficiency over a large area (a centimetre or so around the support). Several solutions have been developed in which an insulated wire or a conductive strip, close to the anode wires but not in contact with them, is raised to a potential high enough to, at least partially, restore the field and therefore the efficiency of detection. In Fig. 82 an example is given of a vinyl-insulated support line and of the corresponding local efficiency measurement[45]; the photograph in Fig. 83 [48] shows a corrugated thin kapton strip, with a printed conductor on one side, which corrects both the anode wire instability and the gap squeezing, with essentially the same efficiency reduction as the previous support line.
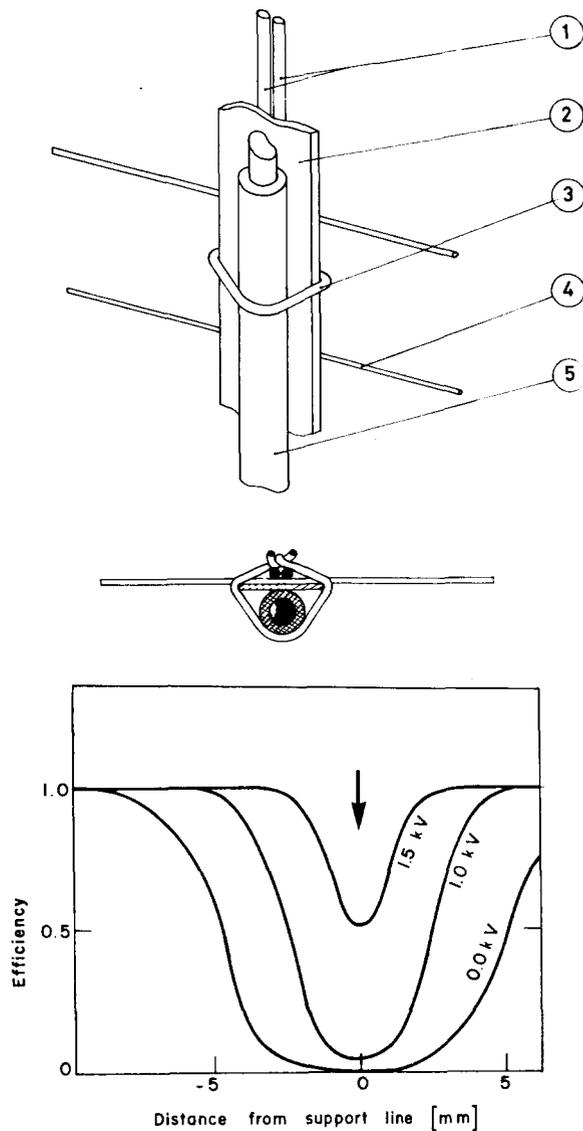

Fig. 82

One of the several support lines developed to avoid electrostatic instability in proportional chambers, together with a measurement of efficiency across the region perturbed by the line[45]. A correction potential given to the central conductor greatly reduces the extension of the inefficient region, as shown by the family of curves.
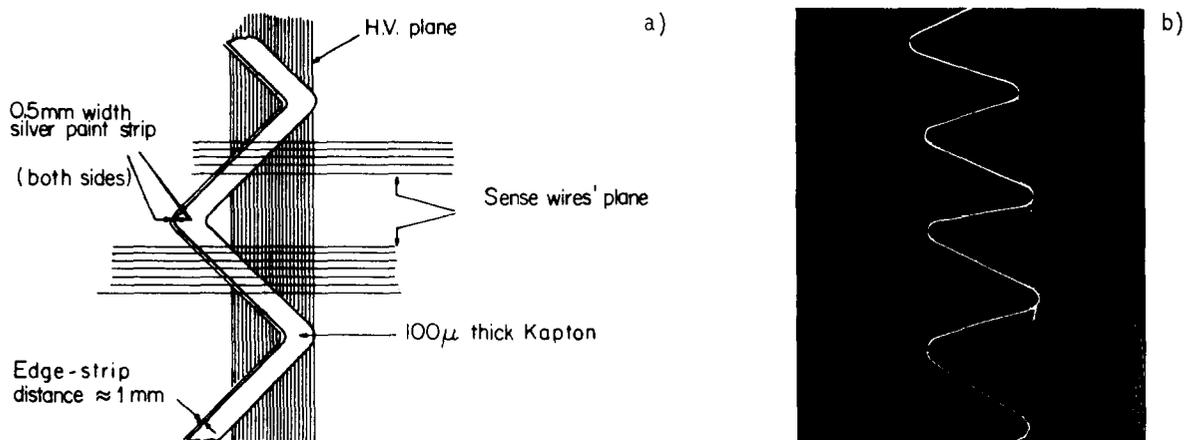
Fig. 83   Example of a mechanical device used both to avoid gap compression (due to the anode-cathode planes attraction) and anode wire instabilities, with a potential-correcting conductor on the anodic side[48])

As far as the electronics is concerned, I will again refer the reader to the abundant literature existing on the subject; almost every group using proportional chambers has developed its own electronic circuit [see the previously quoted references for the chamber's construction, and also Lindsay et al.[62)]. Completely assembled systems are commercially available[63,64). The basic principle of a single-wire electronic channel is shown in Fig. 84. The signal from one anode wire is amplified, discriminated, and shaped to a logical level; typical discrimination levels are between 0.5 mV and 5 mV on 1 kΩ (0.5 to 5 μA), depending on chamber gain and performances (see Section 6.5). The pulse is then delayed by either a passive or an active delay element (cable, delay line, or one-shot monostable), so that the experimenter can select, using a logic gate after the delaying element, only events considered good by fast trigger electronics. In the trigger may participate external devices (such as scintillation counters, particle identifiers, etc.) as well as the signals from the wires or group of wires of the chambers, available through the fast OR output. For accepted events, the wire pattern stored in the memory elements (one per wire) is then read out in a sequential way into a computer.

We shall only mention here that several alternatives to the one channel-per-wire electronics have been developed, based either on delay line read-outs[65-67) or on other analogic methods[68,69).
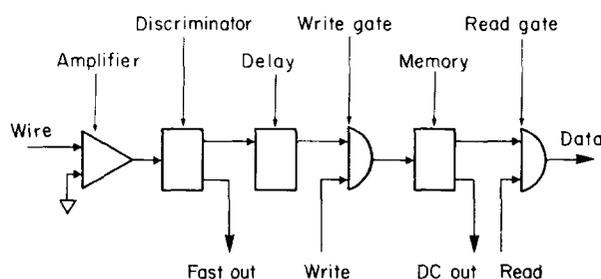

Fig. 84   Basic scheme of the electronics required on each wire in a proportional chamber

7. DRIFT CHAMBERS

7.1 Principles of operation

The possibility of measuring the electrons' drift time to get information about the spatial coordinates of an ionizing event was recognized in the very early works on multiwire proportional chambers[1]. In its basic form, a single-cell drift chamber consists of a region of moderate electric field, followed by a proportional counter (Fig. 85). Suitable field shaping electrodes, wires or strips, as shown in the figure, allow one to obtain the desired electrical configuration. Electrons produced at time t_0 by the incoming charged particle migrate against the electric field with velocity w, and reach the anode wire where avalanche multiplication occurs at a time t_1. The coordinate of the track, in respect to the anode wire, is therefore given by

$$x = \int_{t_0}^{t_1} w \, dt \, , \tag{48}$$

which reduces, for a constant drift velocity, to $x = (t_1 - t_0)w$. It is obviously very convenient to have a linear space-time relationship, and this can be obtained in structures with uniform electric field. If a large surface of detection is required, however, a simple structure like the one of Fig. 85 leads to uncomfortably large working voltages and very long drift times; nevertheless, chambers of this kind having as much as 50 cm drift lengths have been operated, with an over-all drift voltage around 50 kV and maximum drift time (or memory)
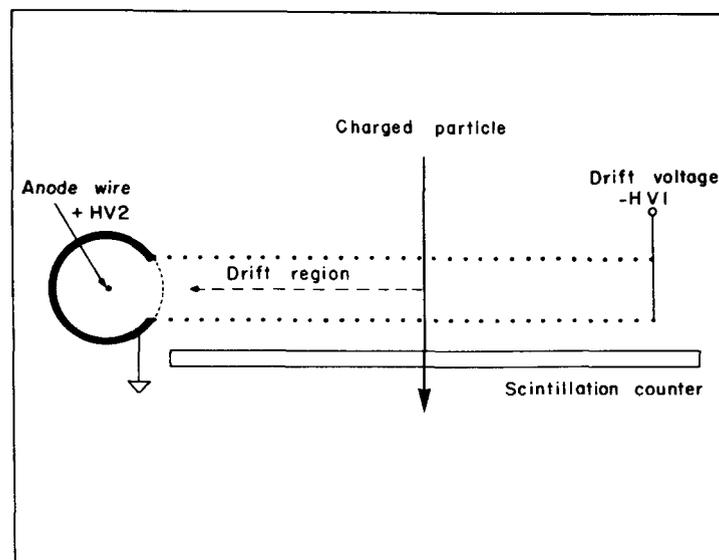
Fig. 85   Principle of operation of a single-cell drift chamber. A set of cathode wires, at suitable potentials, generate in the drift space a region of uniform field. The electrons produced by an ionizing event migrate to one end of the cell, where avalanche multiplication occurs in a single wire proportional counter. The coordinate is then proportional to the time of drift (the time reference being given by an external scintillation counter).

of 7 µsec [70]. For even larger surfaces, or in cases where shorter memory times are necessary because of the expected particle rates, a multicell structure can be used; in this case, since the region of the anode wire becomes necessarily part of the active volume, it is not possible to obtain a constant drift field all across the cell.

In principle, a structure identical to the one of a multiwire proportional chamber can be used to realize a multiwire drift chamber; however, the low field region between the anode wires would result in a strong non-linearity of the space-time relationship, especially for large wire spacings. A modification of the original proportional chamber structure allows the elimination of low field regions in the central plane, as shown in Figs. 86 a and b. The anode wires are alternated with thick field-shaping cathode wires that reinforce the electric field in the critical region. Chambers of this design with anode wire spacing of 1 cm were the first operational drift chambers[71], and were built, with wider wire spacings, up to sizes of about 4 × 4 m² [72]. Other designs, similar in principle to the one described, have been developed, which allow a simpler construction of large surface, mechanically very stiff, drift chambers; Fig. 87 shows one example[73]. Thin aluminium profiles (I-beams), insulated from the cathode planes and kept at a negative potential, serve both the purpose of mechanical spacers and field-reinforcing electrodes. The cathodes are grounded, while the anode wires are maintained at a positive potential to collect and amplify the electrons.
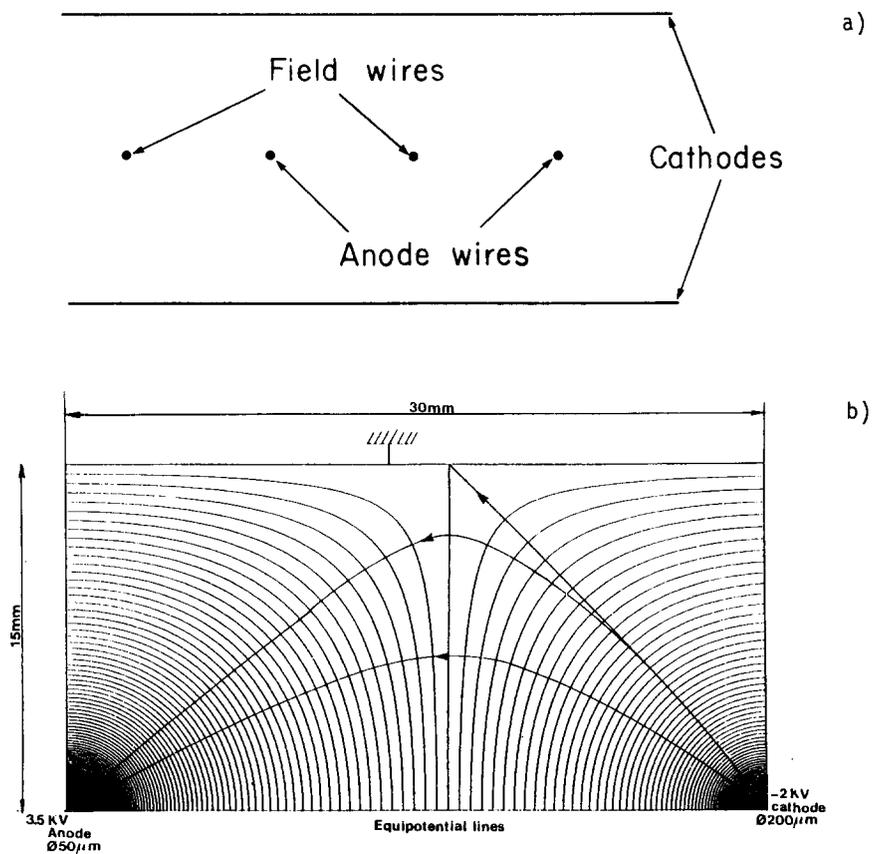

Fig. 86   Principle of the multiwire drift chambers with uniform cathode planes: (a) the basic geometry and (b) the electric field equipotentials in a chamber having 2 × 15 mm gap and 60 mm between anode wires[75].
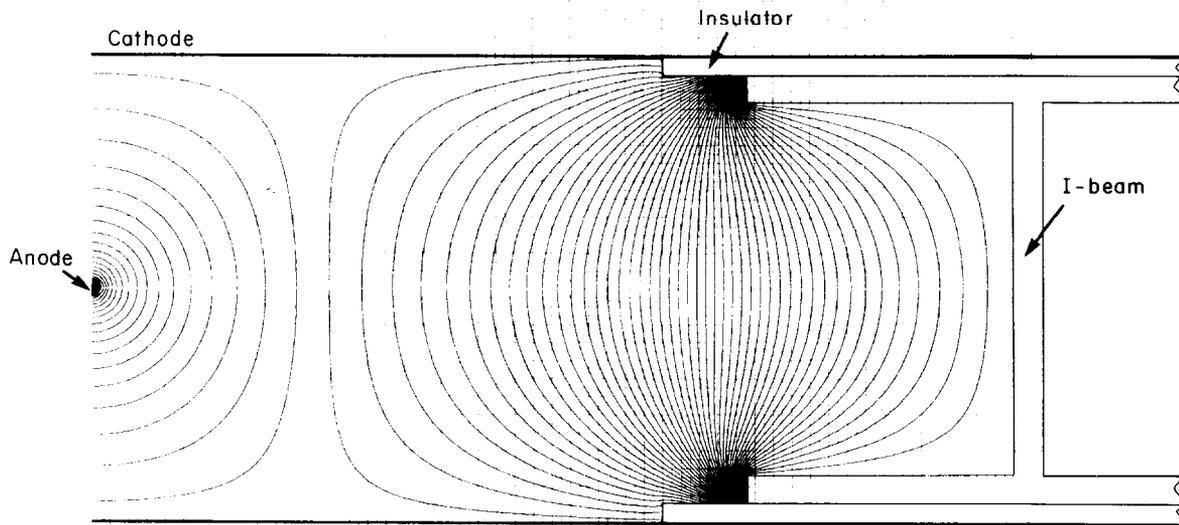
Fig. 87   Equipotentials computed in the Harvard-MIT drift chambers[73]. The field wire has been replaced by an I-shaped profile, insulated from the cathode planes, and serving both the purpose of field reinforcing element and of mechanical stiffener. The gap is 26 mm, the anode wire spacing about 10 cm.

The major limitation of the structures represented in Figs. 86 and 87 lies in the fact that, in order to obtain a relatively uniform drift field, the ratio of the gap length to the wire spacing has to be maintained close to unity. For typical convenient wire spacings (5 to 10 cm) this implies rather thick chambers, and therefore a reduced packaging density. Moreover, it takes a long time to collect at the anode all the electrons produced by a track, and therefore multitrack capability per wire is excluded. These considerations have led to the development of the structure shown in Fig. 88 [9,74]. Two sets of parallel cathode wires are connected to increasingly high negative potentials on both sides starting from the centre of a basic cell; the anode wire is maintained at a positive potential, and two field wires, at the potential of the adjacent cathode wires, sharpen the transition from one cell to the next. The equipotential lines are shown on the figure, for a typical choice of operational
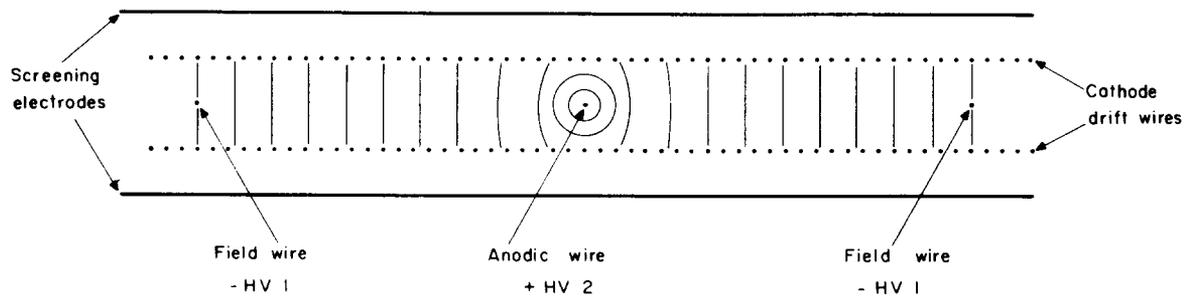

Fig. 88   Principle of construction of the adjustable field multiwire drift chambers[9]. Cathode wires are connected to uniformly decreasing potentials, starting from ground in front of the anode. Field wires reinforce the field in the transition region to the next cell.

voltages; a uniform field drift region is produced in most of the cell. Small gap-to-anode wire spacing ratios can therefore be implemented; typical values of 6 mm and 50 mm have been used for the gap and the anode spacing, respectively. Notice that, since the cathode planes are not equipotentials, some field lines escape from the structure; subsidiary grounded screening electrodes, as shown in the figure, guarantee the immunity of the drift field from external perturbations.

Other structures, intermediate between the ones described, have been developed; Fig. 89 shows, for example, a modification of the geometry of Fig. 86, with the introduction of several additional field-shaping wires that allow reduction of the long collection time on a track by limiting the effective volume of detection[75]. Figure 90 shows instead a scheme where flat electrodes on both sides of the anodes replace the field-shaping wires[76].
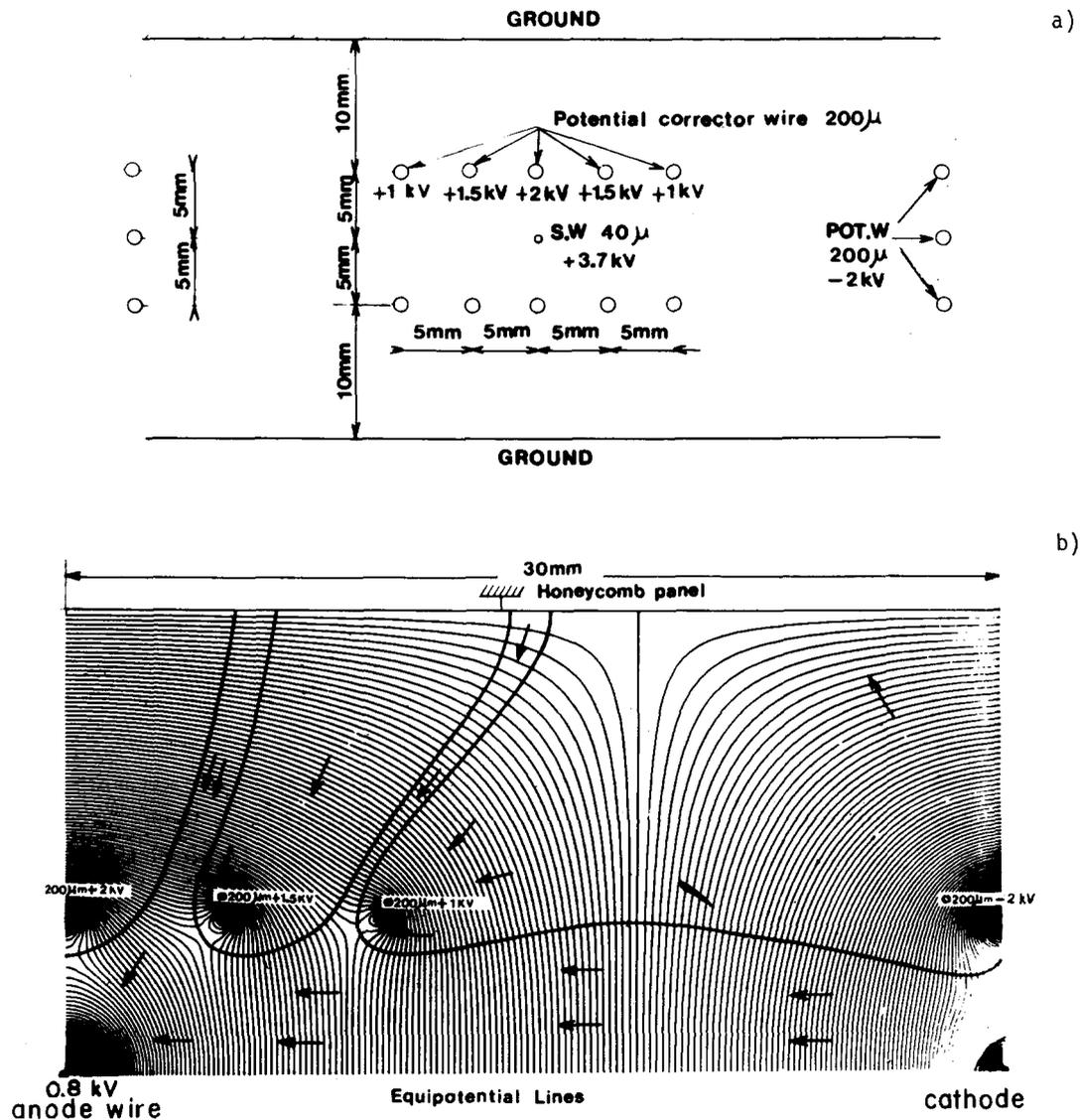

Fig. 89 (a) Geometry of the Saclay chambers, and (b) electric field equipotential in one quarter of the structure[75]. The role of the intermediate potential wires is to limit the accepted fraction of ionizing track so as to have a more or less uniform response along the drift cell.
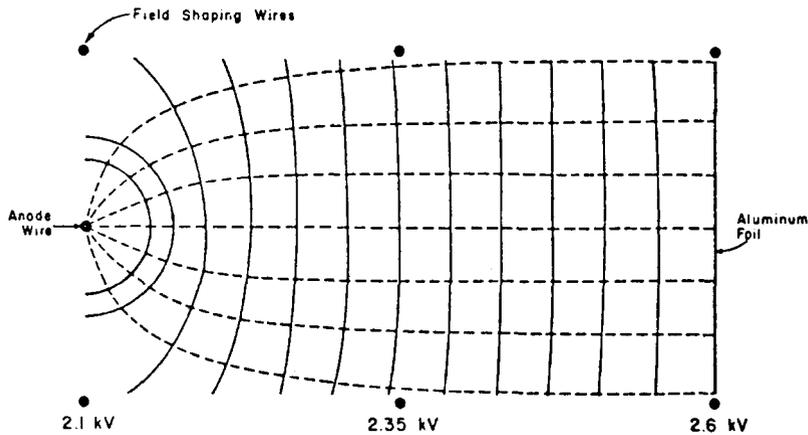
Fig. 90   The drift chambers developed at Fermilab with a thin
            aluminium foil separating adjacent cells[76].

7.2 Space-time correlation and intrinsic accuracy

The ultimate accuracy that can be obtained in a drift chamber depends both on the good
knowledge of the space-time relationship and on the diffusion properties of electrons in gases.
From the considerations of Section 4.4 it appears that, for most gases commonly used in pro-
portional counters, intrinsic accuracies (due to diffusion) below 100 μm are possible for
minimum ionizing particles. The space-time correlation, however, may not be known at this
level of accuracy, especially for large chambers where various mechanical tolerances can
locally modify the electric field structure. Very good results in terms of stability of
operation and reproducibility have been obtained combining the good electric field charac-
teristics of the structure shown in Fig. 88 and the saturated drift velocity peculiarity ob-
tained in selected gas mixtures. Inspection of Fig. 30 shows, for example, that in a 70-30
mixture of argon-isobutane the electrons' drift velocity is roughly constant at fields ex-
ceeding 1 kV/cm. If a chamber is designed in such a way as to avoid regions of field lower
than the quoted value, the sensitivity of the response to local field variation is strongly
reduced.

We shall describe in what follows the main results obtained with a drift chamber of the
kind depicted in Fig. 88, with 6 mm cathode plane separation and 50 mm cell size, operating
in a gas mixture of argon, isobutane and methylal in the proportions, respectively, 67.2%,
30.3% and 2.5% [9]. The dependence of the drift velocity on electric field for this mixture was
given in Fig. 37 [*]. Similar sets of measurements exist for all other drift chamber struc-
tures and can be found in the corresponding quoted references.

A simple way of measuring the space-time relationship in a drift chamber is to record
its time spectrum on a uniformly distributed beam. In fact,

$$\frac{dN}{dt} = \frac{dN}{ds}\frac{ds}{dt} = k \ w(t) \ . \tag{52}$$

Therefore the time spectrum represents the drift velocity as a function of time of drift,
and its integral the space-time relationship. An example of this kind of measurement is

---

*) Notice, comparing Figs. 30 and 37, that the addition of methylal to an argon-isobutane mix-
    ture (necessary for the reasons illustrated in Sections 5.3 and 6.8) increases the satura-
    tion voltage to about 1.2 kV/cm.

given in Fig. 91. Obviously, the limitation of the method lies in the accuracy with which a uniform beam can be produced over a large surface; for more accurate measurements, several methods of mechanical or electronic scanning have been used. Figure 92 shows the result obtained in a chamber of the kind illustrated in Fig. 88 [9]; the space-time correlation has

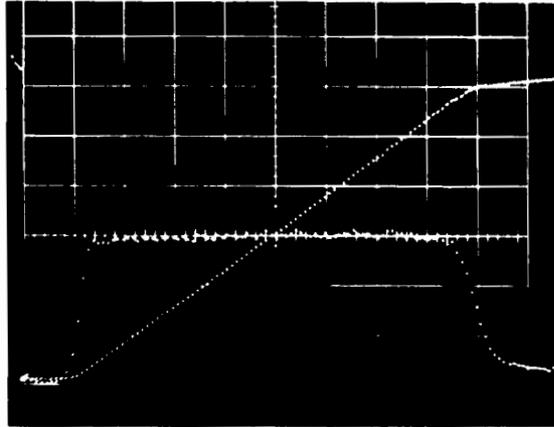Fig. 91   Example of time spectrum and its integral
in a uniform beam, representing respectively
the drift velocity and the space-time rela-
tionship. The measurement has been obtained
by the author with a chamber of the kind de-
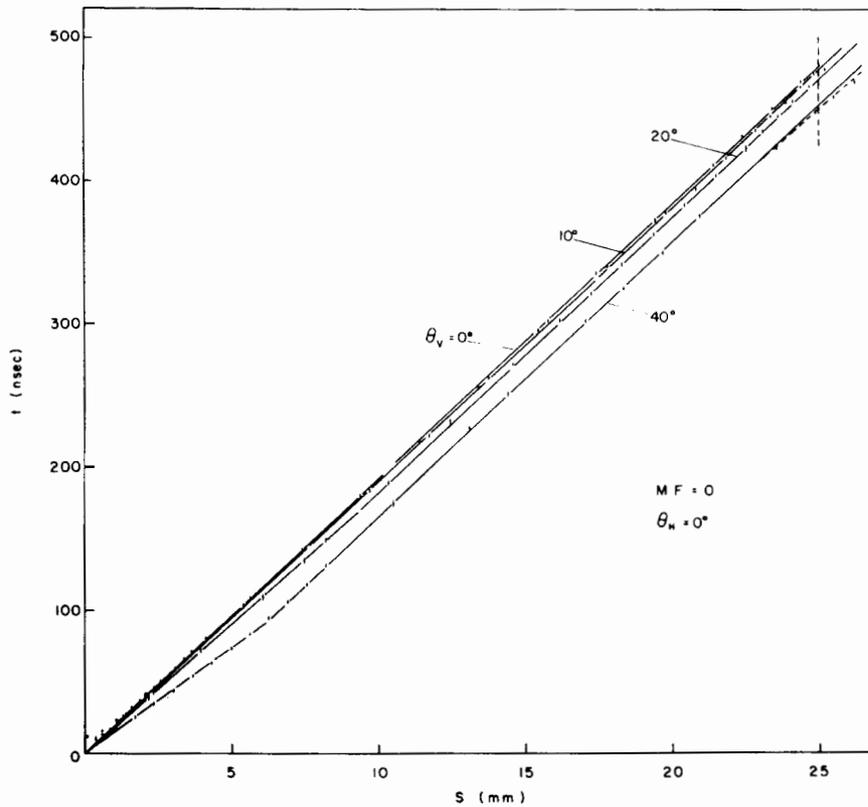scribed in Fig. 88.

Fig. 92   Measured and computed space-time relationship for the
chamber in Fig. 88, as a function of the minimum ionizing
beam angle of incidence[9]

been measured for several angles of incidence of the minimum ionizing beam, and it is strictly linear, within the measurement errors (±50 μm) over all the cell for tracks perpendicular to the chamber plane ($\theta_V = 0°$) with a slope of 5.20 ± 0.02 cm/μsec. For a beam inclined in the plane perpendicular to the wires, the correlation is modified by the fact that the electrons having the shortest time of drift are not those produced in the middle plane of the drift cell. However, a simple two-straight-lines approximation is possible to the measurement, as shown in the figure, under the assumption that the shortest distance to an inclined track is radial around the anode wire and follows the cathode planes thereafter, i.e. as expressed by

$$\begin{cases} x = \dfrac{w}{\cos \theta_V}\, t & \text{for} \quad 0 \le t \le \dfrac{g}{w \sin \theta_V} \\[3mm] x = wt + \dfrac{g}{\sin \theta_V}\left(\dfrac{1}{\cos \theta_V} - 1\right) & \text{for } t \ge \dfrac{g}{w \sin \theta_V} \end{cases} \qquad (53)$$

where g is the total gap width. No deviation for linearity is observed for a beam inclined in a plane parallel to the wires. Normally, of course, the angle of incidence of the tracks is not known *a priori*; an iterative procedure using the data from a set of chambers is then followed , computing an approximated incidence angle under the assumption of a linear correlation. The procedure is, in general, very quickly converging. In structures where the electric field is less uniform, the space-time relationship is obviously more or less deviating from linearity especially if regions of field are met low enough not to allow drift velocity saturation. As an example, Fig. 93 shows the measured correlation in a very large (3.6 × × 3.6 m²) chamber with the structure shown in Fig. 86 and 10 cm between anode wires[72].
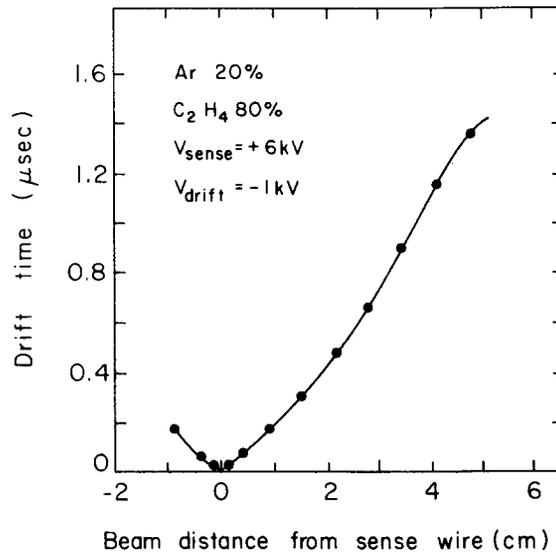

Fig. 93   Space-time relationship for the chamber illustrated in Fig. 86, with 10 cm wire spacing[72]. Due to the large electric field variability, the correlation is not linear.
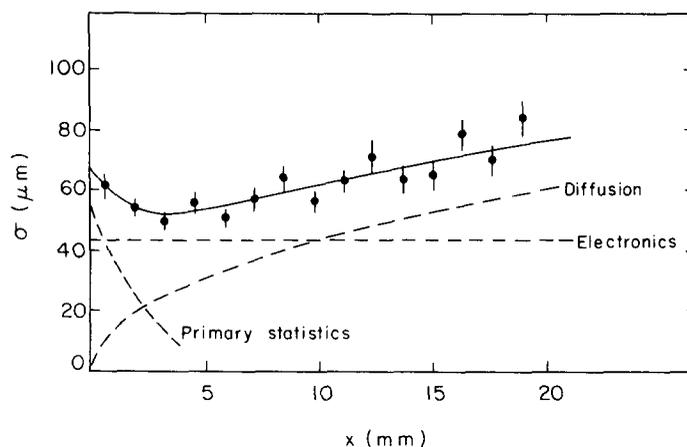
Fig. 94   Measured intrinsic accuracy in the drift chamber
of Fig. 88, as a function of drift space[10]. The
experimental results have been decomposed into
three contributions: a constant electronics dis-
persion, a physical diffusion term function of
the square root of the drift space, and a contri-
bution of the primary ion pair statistics.

The intrinsic accuracy of a chamber can be estimated by the usual method of measuring
the same track in a set of equal chambers, and computing the standard deviation of the dif-
ference, in a given chamber, between the measured and fitted coordinate. One of the best
results obtained so far is presented in Fig. 94 [10], which gives the accuracy as a function
of the drift distance in a chamber like the one in Fig. 88, but with 42 mm anode wire dis-
tance. The result can be decomposed into three main contributions: a square root depen-
dence on the distance of drift, due to electron diffusion, a constant electronics spread
estimated to correspond to about 40 μm as from the figure, and a contribution of the primary
electrons' production statistics, particularly important close to the anode wire (see the dis-
cussion in Section 2.8).

As far as the proportional gain is concerned, drift chambers are, in general, easier to
operate than multiwire proportional chambers, being essentially isolated proportional counters;
all considerations on multiplication factors and gas choice, developed in Sections 5 and 6,
apply as well with the necessary modifications due to the geometry. Exceedingly long effi-
ciency plateaux (about 30% of the working voltage) have been obtained with rather high dis-
crimination thresholds, 5 to 15 μA [77]. The gas purity is, of course, of primary importance
in a drift chamber, especially if long drift spaces are used; the effect of electronegative
gas pollution has been discussed in Section 4.6. Common practice has shown that commercial
grade purities are sufficiently good for moderate drift lengths (a few cm), but that the gas
tightness of the chamber and of the tubing has to be carefully checked. In some cases, a
gas monitoring device at the output of a chamber or a chamber system is advisable.

7.3 Stability of operation

It should be emphasized that the intrinsic accuracy given in Fig. 94 is the result of
a local measurement, normally realized in a short run and essentially independent of the de-
tailed space-time correlation. To make use of the quoted accuracies in an actual coordinate
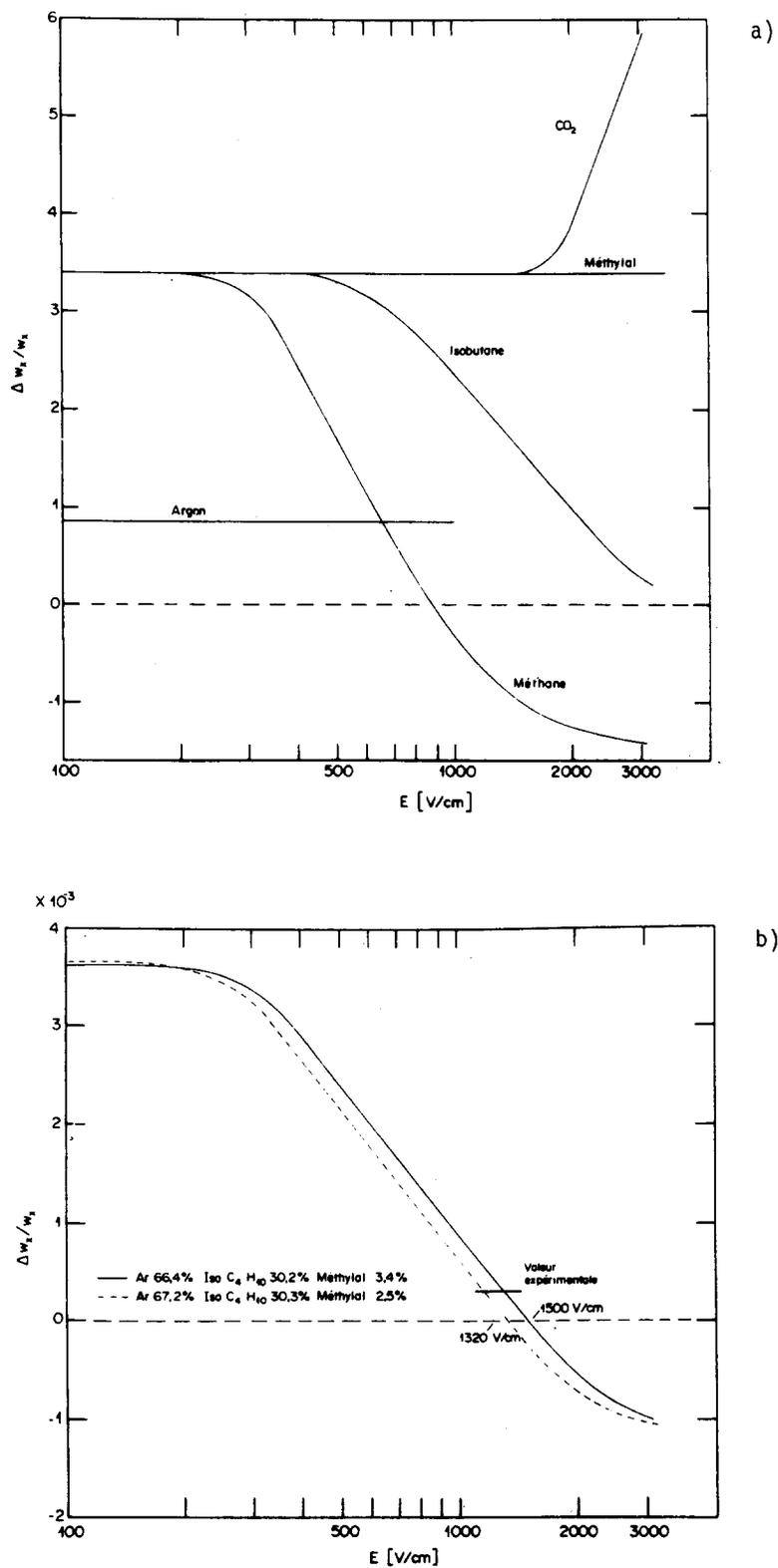measurement, one has, of course, to know precisely the space-time correlation or the drift

Fig. 95 Computed relative dependence of the drift velocity
on the temperature, at 20°C and 1 atm (a) for
several gases and (b) for the particular mixture
used in high-accuracy drift chambers[26])

velocity $w = w(t)$. For a given chamber geometry, the major factors that can influence the drift velocity are: the electric field strength and direction, the atmospheric pressure, the gas composition and temperature, the presence of external factors modifying the drift properties (electric or magnetic stray fields), and the mechanical imperfections. Alghough it is, in principle, possible to take all these factors into account by proper calibration or monitoring, for a realistic system it is more reasonable to set definite limits to the tolerable variations, as a function of the desired final accuracy. The choice of a drift-velocity saturating gas obviously decreases or eliminates the dependence on the reduced electric field E/P. It appears also [25,26] that for several gases and gas mixtures the temperature dependence of w is reduced at high fields (see Fig. 95a); for the particular mixture used by the authors of Ref. 9, the calculation gives a value very close to the experimentally measured one, i.e. $\Delta w/w = 3 \times 10^{-4}$ per °C at a field around 1.4 kV/cm (Fig. 95b). At low fields, and for the same mixture, the relative variation is about one order of magnitude larger. The dependence on gas composition also reduces at saturation, and has been measured in the quoted gas mixture to be $\Delta w/w = 1.2 \times 10^{-3}$ for 1% change in the gas[77]. Using the measured relative variations, one can see that to maintain a ±50 μm stability over 25 mm of drift ($\Delta w/w = \pm 2‰$) a maximum temperature variation of ±7°C, and a maximum gas composition change of ±1.6% can be tolerated.

Mechanical tolerances and electrostatic deformations contribute, of course, directly to the limiting accuracy, and may moreover produce electric field distortions. For large size chambers one should also take into account the thermal expansion of the materials.

7.4 Behaviour of drift chambers in magnetic field

We have seen in Section 4.5 that the presence of a magnetic field other than parallel to the drift direction modifies both the drift velocity and the angle of the electron swarm. In some cases this can be a perturbing factor, if a chamber is situated too close to a stray field, in others instead installation and proper operation of a chamber inside a magnet is desired. Several structures have been studied that permit the use of a drift chamber in strong magnetic fields. Figure 96, for example, shows the computed electron trajectories in
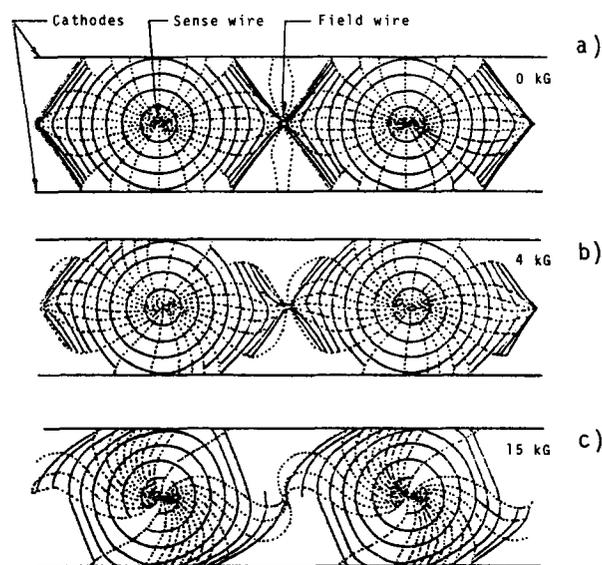

Fig. 96

Computed electron trajectories in a chamber like the one of Fig. 86, for several values of the magnetic field, parallel to the wires[78]
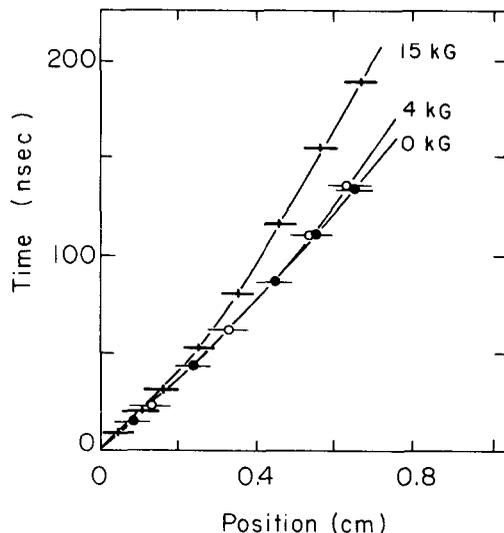
Fig. 97   Computed space-time relationship for
normal tracks in the geometry of
Fig. 96, at increasing values of
the magnetic field[78])

a structure similar to the one of Fig. 86, at increasingly high values of the magnetic field parallel to the sense wires, and Fig. 97 the corresponding time-space relationships[78]. Obviously, precise knowledge of the magnetic field strength and direction is necessary for each position in the chamber and a rather complex parametrization or tabulation for the correlation must be used. In the case of a uniform magnetic field, the electric field in a structure like the one of Fig. 88 can be modified to compensate for the angle of drift. By a suitable choice of the drift voltage connections, the equipotential surfaces in the chamber can be tilted by an angle corresponding to the expected angle of drift (see Fig. 98), the fine adjustment being then possible by a modification of the field strength (see Fig. 38) still maintaining the saturation properties of the velocity. The result of such a procedure can

Fig. 98   Modification of the electric field equipotentials in the structure of
Fig. 88, to allow operation in strong magnetic fields (parallel to the
wires)[77])

Fig. 99   Space-time relationship measured, for several angles of
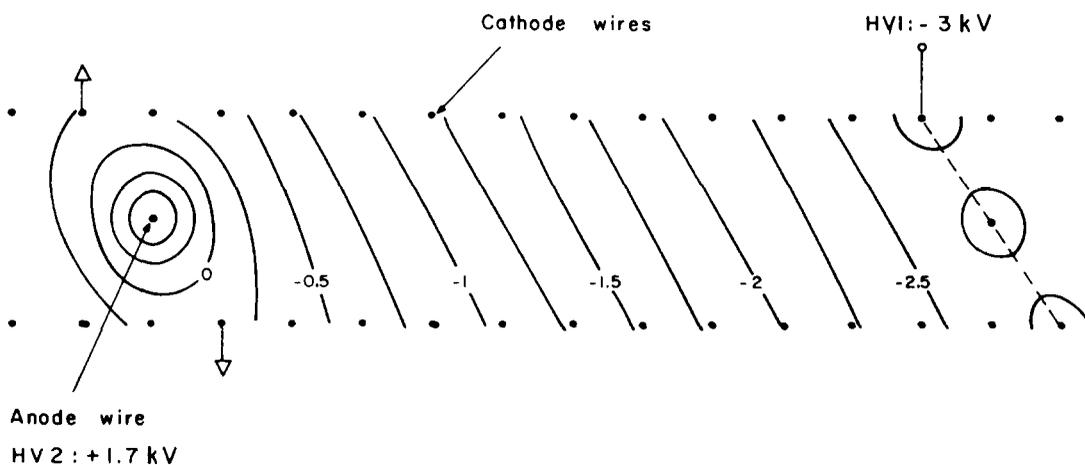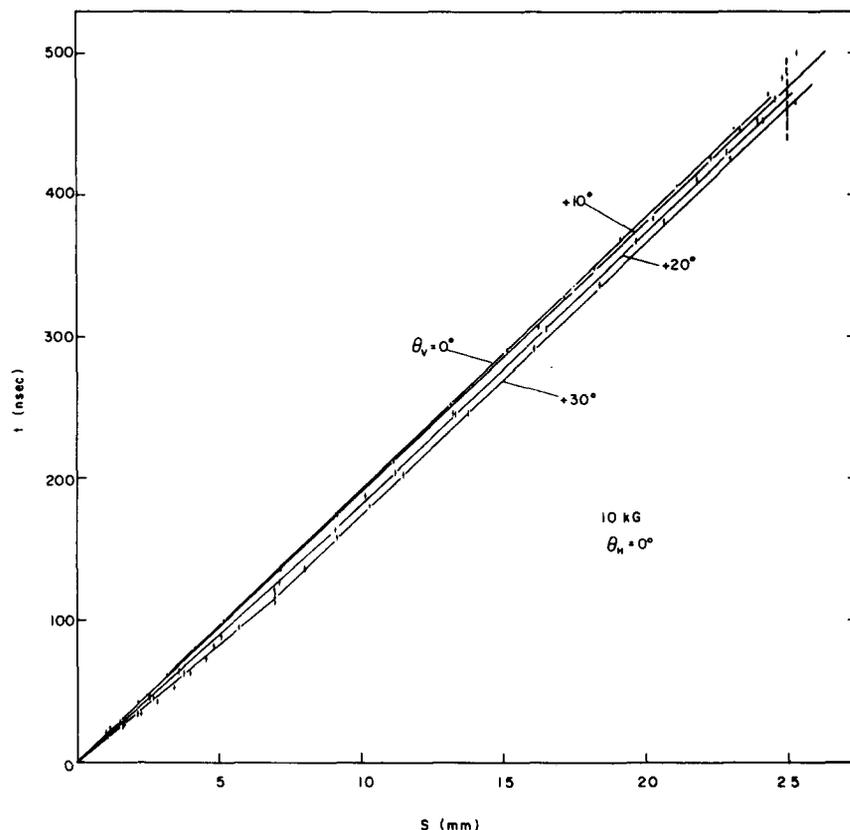incidence, in the chamber of Fig. 98 at 10 kG [9]. The
similarity with the results of Fig. 92 is apparent.

be seen in Fig. 99, where the space-time relationship has been measured for several angles
of incidence and in a magnetic field, parallel to the wires, of 10 kG [9]. The equipotentials'
tilt angle was, in this case, about 29°; the similarity of behaviour to the case of no mag-
netic field, Fig. 92, is apparent. In more complex geometries of magnetic field, or for non-
uniform fields, a simple formulation of the space-time relationship is, of course, not pos-
sible; corrections are then done by using a set of measured drift velocities and angles,
like the ones shown in Figs. 37 and 38. Denoting by $w_\parallel$ the projection of the drift velocity
in the plane of the chamber, or in other words the slope of the space-time correlation, the
following variance has been measured[9] (around 10 kG): $\Delta w_\parallel/w_\parallel = 3 \times 10^{-3}$ per kG. To maintain
a ±50 μm stability, one can therefore tolerate a variation of the axial magnetic field of
±660 G; larger variations imply the use of a modified slope. About the same tolerance has
been found for weak stray fields in a chamber operating with normal geometry.

7.5 Mechanical construction and associated electronics

As for the multiwire proportional chambers, only a brief mention will be given here
about the mechanical construction of drift chambers, and the reader is referred to the quoted
literature for more information. Basically, the same techniques as those developed for the
construction of proportional chambers have been used for drift chambers, except for high ac-
curacy chambers where the general mechanical tolerances and the anode wires' positioning, in
particular, have to satisfy more stringent criteria.

Calculation of the electrostatic forces in a chamber with a structure like the one in Fig. 86 is relatively straightforward and shows that anodic instabilities do not appear for any reasonable length of the wire[72]; on the other hand, the two cathode planes are attracted inwards and the over-all movement can be estimated following the methods outlined in Section 6.4. The same is not true for the configuration depicted in Fig. 88, since the cathode wires are not equipotentials and one cannot assume a uniform charge distribution. Programs have been written to compute the charge on each wire and the relative forces[79,80]. It appears that the more critical point is in the region of the field wire; since the adjacent cathode wires have a charge equal in sign and rather large, they receive a strong outward force. A gap-restoring strip, like the one depicted in Fig. 83, but inserted between the cathodes and the screening electrodes every 50 cm along the wires have proved to be sufficient to compensate the electrostatic forces. Being outside the active volume of the chamber, the strip has no influence on the behaviour of the drift chamber and does not need a field-restoring conductor.

The problem of amplifying and shaping the signals in a drift chamber is also similar to the one encountered in multiwire proportional chambers, except for the fact that one wants, in general, to obtain a better time resolution (implying wider bandwidth and smaller slewing for the amplifier). To measure the time of drift, then, it is possible to use standard time-to-digital converters working in the range of 500 or 1000 nsec, with a channel resolution
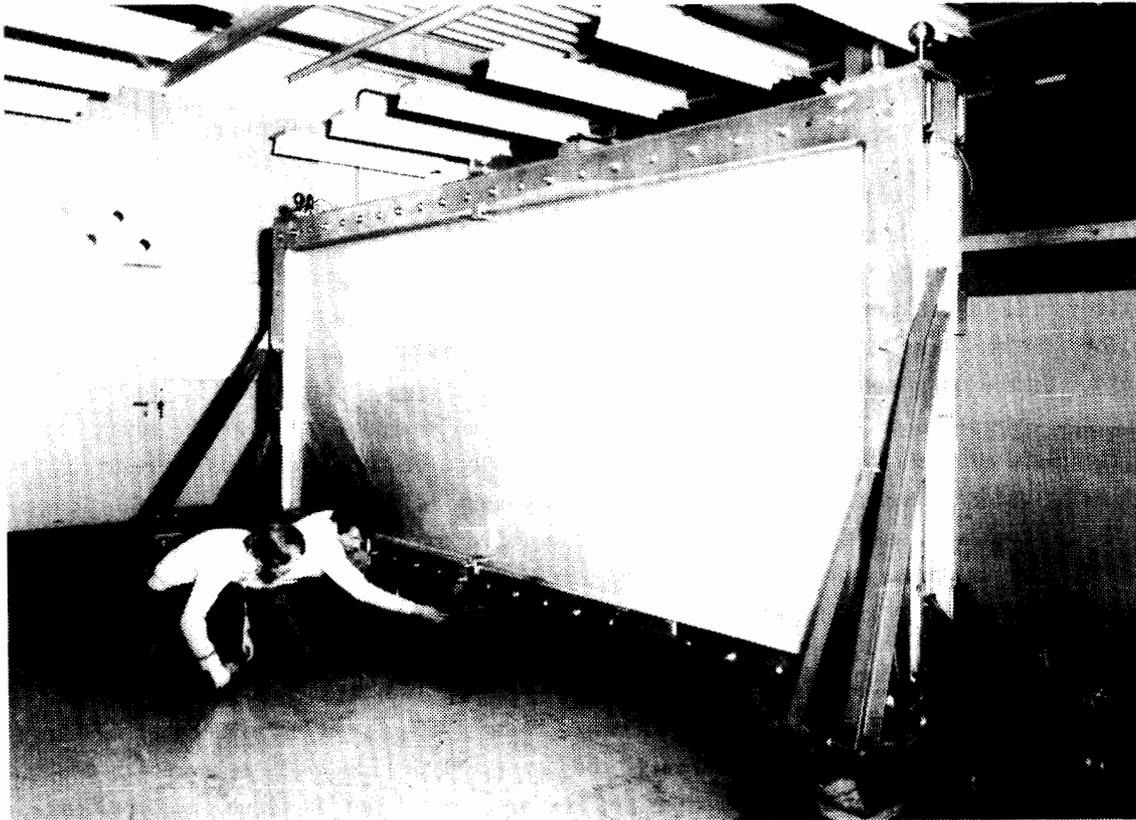

Fig. 100   Large drift chamber (about 4×2.5 m^2) constructed at CERN for the Ω spectrometer lever arm[88]. The module has four independent coordinates, similar in construction to the one depicted in Fig. 88.

around 1 nsec (for the highest accuracy) or worse. However, several dedicated electronic circuits have been developed for drift chambers either cheaper than the standard time-to-digital converters, or allowing multihit-per-wire capability and faster conversion and read-out times[81-87]. Some circuits are already commercially available. A very convenient mode of operation has been incorporated in almost all dedicated drift time digitizers, which allows the provision of the time reference, or time zero, as a late stop instead of as an early start (as required in conventional units). Several hundred nsec are therefore available to the experimenter for making up a trigger selection, using external devices like scintillation and Čerenkov counters, before permanently storing the drift chamber data.

Several large drift chamber systems are already or are close to being operational, including many thousands of drift wires, at CERN and elsewhere. Figure 100 shows a high accuracy drift chamber module developed at CERN[88]; three such chambers approximately $4 \times 2.5 \, m^2$, have been constructed for the Omega magnetic spectrometer.

BASIC BIBLIOGRAPHY

Sections 2 and 3

W. PRICE, Nuclear radiation detection (McGraw-Hill, New York, 1958).

J. SHARPE, Nuclear radiation detectors (Methuen, New York, 1964).

D.H. PERKINS, Introduction to high energy physics (Addison-Wesley, Reading, Mass., 1972).

D.M. RITSON, Techniques of high energy physics (Interscience, New York, 1961).

N.A. DYSON, X-rays in atomic and nuclear physics (Longmans, London, 1973).

Section 4

S.C. BROWN, Basic data of plasma physics (Wiley, New York, 1959).

L.B. LOEB, Basic processes of gaseous electronics (University of California Press, Berkeley, 1961).

R.N. VARNEY and L.H. FISHER, Electron swarms, *in* Methods of experimental physics, (Ed. L. Marton) (Academic Press, New York, 1968), Vol. 7B p. 29.

R.H. HEALEY and J.W. REED, The behaviour of slow electrons in gases (Amalgamated Wireless, Sidney, 1941).

L.G. CHRISTOPHOROU, Atomic and molecular radiation physics (Wiley, New York, 1971).

V. PALLADINO and B. SADOULET, Application of the classical theory of electrons in gases to multiwire proportional chambers and drift chambers, Report LBL-3013 (1974).

Section 5

S.A. KORFF, Electron and nuclear counters (Van Nostrand, New York, 1955).

W. FRANZEN and L.W. COCHRAN, Pulse ionization chambers and proportional counters, *in* Nuclear instruments and their uses (Ed. A.H. Snell) (Wiley, New York, 1956).

S.C. CURRAN and J.D. CRAGGS, Counting tubes, theory and applications (Butterworths, London, 1949).

Sections 6 and 7

G. CHARPAK, Evolution of the automatic spark chambers, Annu. Rev. Nuclear Sci. **20**, 195 (1970).

F. SAULI, Principes de fonctionnement et d'utilisation des chambres proportionnelles multifils *dans* Méthodes expérimentales en physique nucléaire, Ecole d'Eté de Physique théorique, Les Houches, semptembre 1974 (SETAR, Ivry).

P. RICE-EVANS, Spark, streamer, proportional and drift chambers (Richelieu, London, 1974).

REFERENCES

1) G. Charpak, R. Bouclier, T. Bressani, J. Favier and Č. Zupančič, Nuclear Instrum. Methods 62, 235 (1968).

2) See, for example, G. Charpak and F. Sauli, An interesting fall-out of high-energy physics techniques; the imaging of X-rays at various energies for biomedical applications, Proc. Conf. on Computer-Assisted Scanning, Padova, 21-24 April 1976 (Istituto di Fisica, Univ. di Padova, 1976) p. 592.

3) See, for example, D. Ritson, Techniques of high-energy physics (Interscience, New York, 1961).

4) U. Amaldi, Fisica delle radiazioni (Boringhieri, Torino, 1971).

5) D. Jeanne, P. Lazeyras, I. Lehraus, R. Matthewson, W. Tejessy and M. Aderholz, Nuclear Instrum. Methods 111, 287 (1973).

6) M. Aderholz, P. Lazeyras, I. Lehraus, R. Matthewson and W. Tejessy, Nuclear Instrum. Methods 118, 419 (1974).

7) H.L. Brandt and B. Peters, Phys. Rev. 74, 1828 (1948).

8) E.J. Kobetich and R. Katz, Phys. Rev. 170, 391 (1968).

9) A. Breskin, G. Charpak, F. Sauli, M. Atkinson and G. Schultz, Nuclear Instrum. Methods 124, 189 (1975).

10) N.A. Filatova, T.S. Nigmanov, V.P. Pugachevich, V.D. Riabtsov, M.D. Shafranov, E.N. Tsyganov, D.V. Uralsky, A.S. Vodopianov, F. Sauli and M. Atac, Study of drift chambers system for K^-e scattering experiment at Fermi National Accelerator Laboratory, Nuclear Instrum. Methods 143, 17 (1977).

11) See, for example, J.E. Moyal, Phil. Mag. 46, 263 (1955).

12) H.W. Fulbright, Ionization chambers in nuclear physics, in Encyclopedia of Physics (Ed. S. Flügge) (Springer-Verlag, Berlin, 1958), p. 1.

13) G. White Grodstein, National Bureau of Standard Circ. 583 (NBS, Washington, 1957). R.T. McGinnies, National Bureau of Standards, Supplement to Circ. 583 (NBS, Washington, 1959).

14) C.D. Brogles, D.A. Thomas and S.K. Haynes, Phys. Rev. 89, 715 (1953).

15) J.E. Bateman, M.W. Waters and R.E. Jones, Nuclear Instrum. Methods 135, 235 (1976).

16) R.D. Evans, Compton effect, in Handbuch der Physik (Ed. J. Flügge) (Springer-Verlag, Berlin, 1958), Vol. 34, p. 218.

17) A.P. Jeavons, G. Charpak and R.J. Stubbs, Nuclear Instrum. Methods 124, 491 (1975).

18) L.B. Loeb, Basic processes of gaseous electronics (University of California Press, Berkeley, 1961).

19) S.C. Curran and J.D. Craggs, Counting tubes, theory and applications (Butterworths, London, 1949).

20) G. Schultz, G. Charpak and F. Sauli, Mobilities of positive ions in some gas mixtures used in proportional and drift chambers, Rev. Physique Appliquée 12, 67 (1977).

21) J. Townsend, Electrons in gases (Hutchinson, London, 1947).

22) S.C. Brown, Basic data of plasma physics (MIT Press, Cambridge, Mass., 1959).

23) W.N. English and G.C. Hanna, Canad. J. Phys. 31, 768 (1953).

24) A. Breskin, Nuclear Instrum. Methods 141, 505 (1977).

25) V. Palladino and B. Sadoulet, Nuclear Instrum. Methods 128, 323 (1975).

26) G. Schultz, Etude d'un détecteur de particules à très haute précision spatiale (chambre à drift) Thèse, Université L. Pasteur de Strasbourg (1976); also CERN EP Internal Report 76-19 (1976).

27) S.A. Korff, Electrons and nuclear counters (Van Nostrand, New York, 1946).

28) O.K. Allkofer, Spark chambers (Theimig, München, 1969).

29) R. Bouclier, G. Charpak and F. Sauli, Parallel-plate proportional counters for relativistic particles, CERN NP Internal Report 71-72 (1971).

30) G. Charpak, Filet à particules, Découverte (février 1972), p. 9.

31) H. Staub, Detection methods, in Experimental Nuclear Physics (Ed. E. Segré) (Wiley, New Nork, 1953), Vol. 1, p. 1.

32) L. Malter, Phys. Rev. 50, 48 (1936).

33) G. Charpak, H.G. Fisher, C.R. Grühn, A. Minten, F. Sauli, G. Plch and G. Flügge, Nuclear Instrum. Methods 99, 279 (1972).

34) A.J.F. Den Boggende, A.C. Brinkman and W. de Graaff, J. Sci. Instrum. (J. Phys. E) 2, 701 (1962).

35) W.S. Bawdeker, IEEE Trans. Nuclear Sci. NS-22, 282 (1975).

36) R.W. Hendricks, Rev. Sci. Instrum. 40, 1216 (1969).

37) G.A. Erskine, Nuclear Instrum. Methods 105, 565 (1972).

38) G. Charpak, Annu. Rev. Nuclear Sci. 20, 195 (1970).

39) P. Morse and H. Feshbach, Methods of theoretical physics (McGraw Hill, New York, 1953).

40) E. Durand, Electrostatique (Masson, Paris, 1964) Vol. 1.

41) P.A. Souder, J. Sandweiss and D.A. Disco, Nuclear Instrum. Methods 109, 237 (1973).

42) Z. Dimčowski, Calculation of some factors governing multiwire proportional chambers, CERN NP Internal report 70-16 (1970).

43) T. Trippe, Minimum tension requirements for Charpak chambers' wires, CERN NP Internal Report 69-18 (1969).

44) P. Schilly, P. Steffen, J. Steinberger, T. Trippe, F. Vannucci, H. Wahl, K. Kleinknecht and V. Lüth, Nuclear Instrum. Methods 91, 221 (1971).

45) G. Charpak, G. Fischer, A. Minten, L. Naumann, F. Sauli, G. Flügge, Ch. Gottfried and P. Tirler, Nuclear Instrum. Methods 97, 377 (1971).

46) A. Michelini and K. Zankel, A first design study of a large area proportional counter, CERN Internal Note OM/SPS/75/5 (1975).

47) R. Bouclier, G. Charpak, E. Chesi, L. Dumps, H.G. Fischer, H.J. Hilke, P.G. Innocenti, G. Maurin, A. Minten, L. Naumann, F. Piuz, J.C. Santiard and O. Ullaland, Nuclear Instrum. Methods 115, 235 (1974).

48) S. Majewski and F. Sauli, Support lines and beam killers for large size multiwire proportional chambers, CERN NP Internal Report 75-14 (1975).

49) R. Bouclier, G. Charpak, Z. Dimčowski, G. Fischer, F. Sauli, G. Coignet and G. Flügge, Nuclear Instrum. Methods 88, 149 (1970).

50) H. Fischer, F. Piuz, W.G. Schwille, G. Sinapsius and O. Ullaland, Proc. Internat. Meeting on Proportional and Drift Chambers, Angle measurement and space resolution in proportional chambers, Dubna, 1975.

51) M. Breidenbach, F. Sauli and R. Tirler, Nuclear Instrum. Methods 108, 23 (1973).

52) S. Brehin, A. Diamant Berger, G. Marel, G. Tarte, R. Turlay, G. Charpak and F. Sauli, Nuclear Instrum. Methods 123, 225 (1975).

53) G. Charpak and F. Sauli, Nuclear Instrum. Methods 96, 363 (1971).

54) B. Sadoulet and B. Makowski, Space charge effects in multiwire proportional counters, CERN D PH II/PHYS 73-3 (1973).

55) S. Declay, J. Duchon, H. Louvel, J.P. Datry, J. Seguinot, P. Baillon, C. Bricman, M. Ferro-Luzzi, J.M. Perreau and T. Ypsilantis, K⁻p and K⁻n final states in K̄d collisions between 1.2 and 2.2 GeV/c, submitted to Nuclear Phys. B, May 1976.

56) S. Parker, R. Jones, J. Kadyk, M.L. Stevenson, T. Katsure, V.Z. Peterson and D. Yount, Nuclear Instrum. Methods 97, 181 (1971).

57) E. Bloom, R.L.A. Cottrell, G. Johnson, C. Prescott, R. Siemann and S. Stein, Nuclear Instrum. Methods 39, 259 (1972).

58) R. Lanza and N. Hopkins, Nuclear Instrum. Methods 102, 131 (1972).

59) J. Buchanan, L. Gulson, N. Galitzsch, E.V. Hungerford, G.S. Mutchler, R. Persson, M.L. Scott, J. Windish and G.C. Phillips, Nuclear Instrum. Methods 99, 159 (1972).

60) K.B. Burns, B.R. Grummon, T.A. Nunamaker, L.W. Who and S.C. Wright, Nuclear Instrum. Methods 106, 171 (1973).

61) L. Baksay, A. Böhm, H. Foeth, A. Staude, W. Lockman, T. Meyer, J. Rander, P. Schlein, R. Webb, M. Bozzo, R. Ellis, B. Naroska, C. Rubbia and P. Strolin, Nuclear Instrum. Methods 133, 219 (1976).

62) J. Lindsay, Ch. Millerin, J.C. Tarlé, H. Verweij and H. Wendler, A general-purpose amplifier and read-out system for multiwire proportional chambers, CERN 74-12 (1974).

63) LeCroy Model 2720 and LD604 (LeCroy Research Systems Co., New York).

64) FILAS, 8-channel MOS circuit for proportional chambers (Société pour l'Etude et la Fabrication de Circuits intégrés spéciaux, Grenoble, France).

65) R. Grove, K. Lee, V. Perez-Mendez and J. Sperinde, Nuclear Instrum. Methods 89, 257 (1970).

66) D.M. Lee, J.E. Sobottka and H.A. Thiessen, Los Alamos Report LA-4968-MS (1972).

67) F. Bradamante, S. Connetti, C. Daum, G. Fidecaro, M. Fidecaro, M. Giorgi, A. Penzo, L. Piemontese, A. Prokofiev, M. Renevey, P. Schiavon and A. Vascotto, Electric delay-line read-out for multiwire proportional chambers in Proc. Internat. Conf. on Instrumentation for High-Energy Physics, Frascati, 1973 (Lab. Naz. CNEN, Frascati, 1973).

68) J. Hough and R.W.P. Drever, Nuclear Instrum. Methods 103, 365 (1972).

69) H. Foeth, R. Hammarström and C. Rubbia, Nuclear Instrum. Methods 109, 521 (1973).

70) J. Saudinos, J.C. Duchazeaubeneix, C. Laspalles and R. Chaminade, Nuclear Instrum. Methods 11, 77 (1973).

71) A.H. Walenta, J. Heintze and B. Schürlein, Nuclear Instrum. Methods 92, 373 (1971).

72) D.C. Cheng, W.A. Kozanecki, R.L. Piccioni, C. Rubbia, R.L. Sulak, H.J. Weedon and J. Wittaker, Nuclear Instrum. Methods 117, 157 (1974).

73) Experiment R209 at CERN (H. Newman, private communication).

74) G. Charpak, F. Sauli and W. Duinker, Nuclear Instrum. Methods 108, 413 (1973).

75) G. Marel, P. Bloch, S. Brehin, B. Devaux, A.M. Diamant-Berger, C. Leschevin, J. Maillard, Y. Malbequi, H. Martin, A. Patoux, J. Pelle, J. Plancoulaine, G. Tarte and R. Turlay, Large planar drift chambers, Nuclear Instrum. Methods 141, 43 (1977).

76) M. Atac and W.E. Taylor, Nuclear Instrum. Methods 120, 147 (1974).

77) A. Breskin, G. Charpak, B. Gabioud, F. Sauli, N. Trautner, W. Duinker and G. Schultz, Nuclear Instrum. Methods 119, 9 (1974).

78) B. Sadoulet and A. Litke, Nuclear Instrum. Methods 129, 349 (1975).

79) F. Bourgeois and J.P. Dufey, Programmes de simulation des chambres à drift en champs magnétique, CERN NP Internal Report 73-11 (1973).

80) A. Wylie, Some calculations of drift chamber electric fields, CERN NP Internal Report 74-7, September 1974.

81) B. Schurlein, W. Farr, H.W. Siebert and A.H. Walenta, Nuclear Instrum. Methods 114, 587 (1974).

82) E. Schuller, A two-clock sensing system, a new time-to-digital converter, CERN NP Internal Report 73-15 (1973).

83) H. Verweij, Electronics for Drift Chambers, IEEE Trans. Nuclear Sci. NS-22 437 (1975). See also: DTR, Drift Time Recorder, CERN Type EP247.

84) W. Sippach, Drift chambers electronics, NEVIS Internal Report (1975).

85) C. Rubbia, New electronics for drift chambers, CERN NP Internal Report 75-10 (1975).

86) M. Atac and T. Droege, Notes on drift chambers time digitizer meeting, Fermilab Int. Note TM-553 (April 1975).

87) LeCroy Model 2770A, Drift chambers digitizer.

88) A. Dalluge and M. Jeanrenaud, private communication at CERN.